

The authors appreciate the reviewer's constructive and friendly comments. We have substantially revised the manuscript. New data and figures are present in the main text. A new supplementary document is included in the revision. We reply to the reviewer's comments point by point.

### **Anonymous Referee #1**

Received and published: 19 October 2020

The manuscript presents the development of assimilation of aerosol observations into WRF-Chem using the GSI system using approaches that are different to those used in previous studies. These developments are then tested for a case of assimilating ground-based observations of particle mass concentration, scattering and absorption coefficients, and AOD, performing sensitivity simulations on assimilating datasets independently and jointly. This is done for a single site located in Kashi, representative of dust conditions. This study is within the scope of ACP and represents good contributions to the field as it develops a tool that could be used by the community and highlights shortcomings in the techniques and how could they be improved. I think the paper needs a bit more work before it's ready for publication based on the comments below.

My main comments are the following.

- While the WRF-Chem optical properties module assumes Mie theory which is based on particles being spherical, the testing of the tool is focused on dust which are mostly non-spherical particles. This is briefly mentioned in the article, but I would like to see more on the subject, including looking into literature that has explored this topic and discussion on what discrepancies obtained in this study could be explained by this issue. See more on by line comments.

Response: Yes, the spherical dust particle in WRF-Chem introduces uncertainty. We reviewed a few literatures and added a paragraph to discuss the impact of non-spherical particles in section 3.3.

- I believe that what the authors defined as Adjoint operators are really the tangent linear models, i.e., the derivative of the observables with respect to the inputs (aerosol mass). The adjoint operates on perturbations on the observables and outputs the expected perturbations on inputs. Please verify with the literature and correct accordingly.

Response: The author appreciates the reviewer's kindly comment. We have changed the misstatement of "adjoint operator" to "tangent linear operator".

- Assess representation of some intensive properties such as size (e.g., angstrom exponent, ratio of pm<sub>2.5</sub> to pm<sub>10</sub>), single-scattering albedo, and mass scattering efficiency to try to understand mismatches when doing assimilation. A little bit is done but it would be very helpful to expand this topic and use the nomenclature used in the literature. See more on by line comments.

Response: According to this comment, the revised manuscript shows additional assessments of angstrom exponent and SSA (Table 3). A new figure 10 shows the multi-wavelength mass scattering/absorption coefficient. Hope this additional content makes this study more convincing.

- Absorption seems completely biased even after assimilation, this points to issues probably related to underestimation of imaginary refractive index of dust. Look for literature on this depending on the deserts, I believe Chinese deserts tend to have darker (i.e., more absorbing) sands.

Response: We used the generic model value of dust refractive index in the first version manuscript. In the revision, we increased the imaginary part of the dust refractive index, which is higher than the imaginary part of the Taklimakan desert that has been retrieved by Di Biagio et al. (2019). We find that tuning dust DA is not helpful for removing the DA bias in absorption coefficient. We redid a lot of DA experiments and found a negligence of anthropogenic emission in the WRF-Chem simulation. This strong bias in absorption DA is relevant to the low concentration of black carbon (BC) and the low BC's background error. We have rewritten the relevant content in section 3.5.

Di Biagio, C., et al.: Complex refractive indices and single-scattering albedo of global dust aerosols in the shortwave spectrum and relationship to size and iron content, Atmos. Chem. Phys., doi:10.5194/acp-19-15503-2019, 2019.

Comments by line:

103-108. For completion, consider citing and discussing the study by Kumar et al (2019) that also uses GSI with CMAQ but does not use the CRTM as Tang study. This study also provides an alternative way of computing the BEC matrix (other than the NMC method) which you discuss in section 2.3

Response: We added a few words about Kumar et al. (2019) study in the revised introduction and section 2.3.

545-552. Are all of these observations in the same location? If not how far apart are they? How many PM2.5/PM10 sites are used? Also, what's the inlet cutoff size used for the scattering and absorption measurements? This is important to related mass and optical properties properly.

Response: All the observations (PM2.5, PM10, AOD, scattering/absorption coefficient) were carried out at a single site. There was no inlet cutoff for the scattering and absorption measurements. In the revised manuscript:

*"The site was placed in the Kashi campus of the Aerospace Information Research Institute, Chinese Academy of Sciences (39.50°N, 75.93°E; Li et al., 2018), about 4 km in the northwest to the Kashi city. ... All the instruments were deployed at the roof of a three stories height building on the campus."*

554-561. Could you add justification for the PM2.5/PM10 observation errors stated in Table 1? There is no explanation how the errors were picked. Also, why do you only use representative error for PM2.5/PM0 but not for the other observations?

Response: In the revised section 2.4:

*"The observation errors of PM<sub>x</sub> are handled in the conventional way (Schwartz et al., 2012; Chen et al., 2019), which contains the measurement error ( $e_1$ ) and the representative error ( $e_2$ ). The measurement error is the sum of a baseline error of  $1.5 \mu\text{g m}^{-3}$  and 0.75% of the observed PM<sub>x</sub> concentration. The representative error is the measurement error multiplied by the half-squared ratio of the grid spacing to*

*the scale distance. The scale distance denotes the site representation in GSI and has four default values of 2, 3, 4, and 10 km, corresponding to the urban, unknown, suburban, and rural sites. We used 3 km for the scale distance in this study. As we had a single site in Kashi, it is difficult to estimate the site representation error. Since the DA analysis was based on the child model domain with a horizontal resolution of 5 km, close to the site distance to the Kashi urban area, we assumed the aerosol optical measurement had good representativeness of the model grid covering the site. The observation error of CE318 AOD took the AERONET AOD uncertainty of 0.01 in cloud-free conditions (Holben et al., 1998).”*

569. Can you add a bit more info on the vertical resolution? For instance, thickness of the 1st level and number of levels within 1km.

Response: In the revised section 2.5:

*“Both domains had 41 vertical levels extending from the surface to 50 hPa. The lowest model layer at the site was approximately 25-meter height from the ground.”*

594-596. Can you clarify if you did 2 simulations every cycle with and without aerosol interacting with radiation, or it was a single simulation with two calls to the radiation code within the same simulation?

Response: It was a single simulation with two calls to the radiation code. In the revised section 2.5:

*“To study the impact of DA on aerosol direct radiative forcing (ADRF), we modified the WRF-Chem code to calculate the shortwave irradiance with and without aerosols at each model integration step. The modified WRF-Chem model restarted from each DA analysis and ran to the next analysis time. Each running performed the radiation transfer calculation twice, and each calculation saw the aerosols and clean air, respectively. The irradiance difference between the two pairing calls was aerosol radiative forcing.”*

632-638. You are also missing some processes of potential importance such as secondary organic aerosol formation and heterogeneous sulfate formation influencing low-dust days.

Response: Yes, our simulation did not have SOA, and the heterogeneous sulfate formation in WRF-Chem may bias. Nevertheless, we accidentally lowered the anthropogenic emissions in the original WRF-Chem simulation. Because of the ambition of haze abatement in China since 2013, the anthropogenic emissions had dramatic reductions in 2013-2019. So far as we know, a timely update of emission inventories is not available, and we used the open MEIC emission inventories for the year 2010 when the anthropogenic emissions had peak values. A general way to handle this emission reduction is to scale the historical emissions, which were not appropriately handled in our first manuscript. The anthropogenic emissions that we set for Kashi in the 2019 simulation were too low. As lack of aerosol measurement at Kashi, the low bias was not identified at the first glance. In the revised manuscript, we just ignore the yearly emission differences. We redid all simulations with the MEIC emission inventories for 2010.

The revised model concentrations of PM<sub>2.5</sub> and PM<sub>10</sub> are almost equivalent to the old data (Figure 1) because dust is the dominant component at Kashi. Besides, the real part of the refractive index of sulfate, nitrate, ammonium, and dust are comparable in the model. Thus, the new results do not change

the conclusion. The new advantage is that the DA bias in absorption coefficient can be somewhat attributed to black carbon when the BC's background error was amplified. We rewrote the DA of the absorption coefficient in section 3.5.

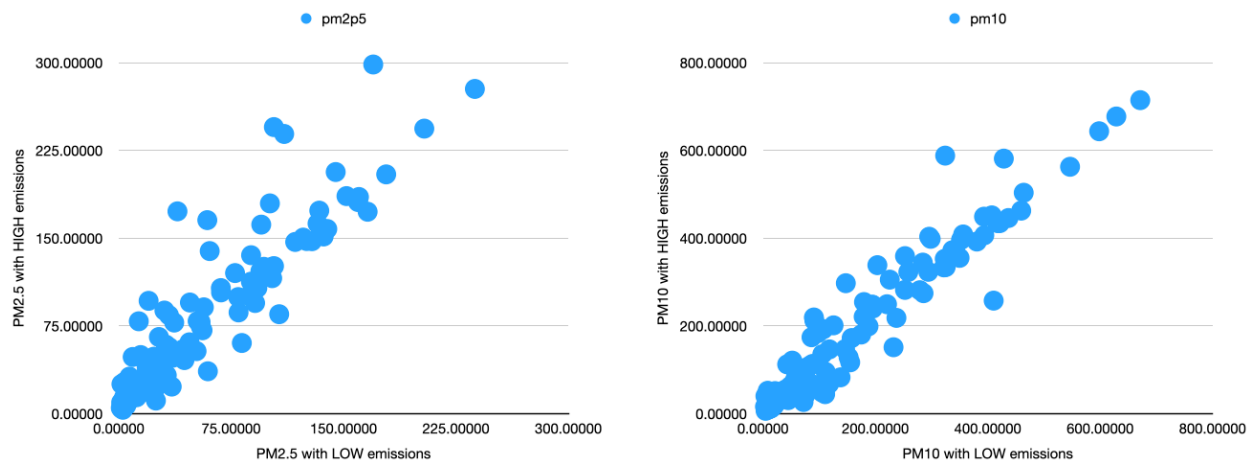


Figure 1. Comparisons of PM<sub>2.5</sub> (left) and PM<sub>10</sub> (right) in the WRF-Chem simulations with high (y-axis) and low anthropogenic emissions (x-axis) at Kashi in April 2019

645-647. I think a better fit to PM<sub>2.5</sub> could be achieved if you relaxed the interbin correlation. It looks like PM<sub>10</sub> is fitting pretty well but it's going a bit over the observation, so this is restricting increases in PM<sub>2.5</sub> due to the correlation. Since bin 4 is 2.5-10um, in theory, if no interbin correlation was present, PM<sub>10</sub> and PM<sub>2.5</sub> should be able to fit independently. For this study it would make sense to relax the interbin correlation due to the known issues in dust size distributions (see next comment)

Response: Based on lots of experiments, we find that the analyses are not sensitive to the inter-size bin correlation length in this case, though the analyses changed a lot when we turned off the inter-size bin correlation. We find that the magnitude of large background error of coarse dust is more effective in affecting the analysis of PM<sub>2.5</sub>. Reducing the background error of the fourth size bin OIN (oin\_a04) will increase PM<sub>2.5</sub> and decrease PM<sub>10</sub>. We added table S3 in the supplementary document, which shows the PM<sub>x</sub> response to the different magnitudes of oin\_a04's background error.

In the revised section 3.2:

*“Applying the inter-size bin correlation length caused the interlinked analyses of PM<sub>2.5</sub> and PM<sub>10</sub>. In the desert area, the coarse and fine dust are readily affected by the magnitude of BEC of the fourth size-bin OIN (oin\_a04). We intentionally decreased the BEC of oin\_a04 by 10% each time to 30% of its original value. The magnitude of 30% of oin\_a04 was comparable to the magnitude of the third size-bin (oin\_a03) OIN's background error. As shown in Table S3, because the oin\_a04's BEC reduction relaxes the constraint on the coarse particle, the PM<sub>10</sub> bias becomes more negative along with the decrease in oin\_a04's BEC. Meanwhile, the PM<sub>2.5</sub> bias becomes more positive. Correspondingly, the ratio of PM<sub>2.5</sub> to*

*PM<sub>10</sub> was exaggerated to 0.33 with 30% of oin\_a04's BEC, higher than the observed value of 0.28. Overall, the original BEC of oin\_a04 is a reasonable tradeoff in our DA experiments."*

647-652. Literature on dust modeling states that parameterizations tend to overpredict the fine dust and underpredict the coarse dust (see Kok et al., 2011, Adebisi and Kok 2020). So the joint assimilation of PM<sub>2.5</sub> and PM<sub>10</sub> could be somewhat correcting for that, which is an additional possible explanation to the behavior explained in these sentences.

Response: Thanks for the hint. We cite the two pieces of literature in the revised section 3.2:

*"As a result, the ratio of PM<sub>2.5</sub> to PM<sub>10</sub> decreased from 0.39 in the background to 0.27 in DA\_PMx, approaching the observed ratio of 0.28. Such improvement was consistent with the correction required to the model desert dust in literature. Kok et al. (2011) found that regional and global circulation models underestimate the fraction of emitted coast dust (>~5 μm), overestimates the fraction of fine dust (<2 μm diameter). Adebisi and Kok (2020) claimed that too rapid deposition of coarse dust out of the atmosphere accounts for the missing coarse dust in models. Similarly, WRF-Chem assimilated too much smaller dust particles than the observed. According to Kashi's AOD between 440 nm and 1020 nm, the observed Ångström exponent (AE) was 0.18 in this case, but the background value was 0.54 (Table 3). DA\_PMx reduced the AE value to 0.30, a little improvement but not sufficient."*

672-685. Another reason for the discrepancy is related to the size distribution. Are you assimilating multi-wavelength AOD here, right? If so, I would expect some modifications to the size distribution. It looks you are effectively modifying size distr. as the ratio of PM<sub>2.5</sub> to PM<sub>10</sub> ratio is reduced from 0.31 in the background to 0.11 in the DA\_AOD simulation but it might be going a bit too far as the observed ratio is 0.28. You can also check angstrom exponent. You can also explore the point you make at the end related to the dust mass extinction efficiency, you have observations to compute this at the surface. Additionally, there is also potential for your vertical distribution to be off and be generating these issues. You can diagnose this by comparing the ratio of surface extinction vs AOD. It seems the model is overpredicting this ratio, which could mean too much aerosol close to the surface.

Response: In the revised manuscript, we check the PM<sub>2.5</sub>/PM<sub>10</sub> ratio, mass extinction efficiency, angstrom exponent (AE), and SSA. We do not check the ratio of surface extinction and AOD because it requires the interpolation of surface extinction and AOD to similar wavelength. The model has a large bias in AE, resulting in an unreliable interpolation. We rewrote a lot in sections 3.2 and 3.3. Please refer to the revised manuscript.

Related to this point. You are actually already computing mass scattering efficiency (2nd column in Table 3). The background already underpredicts it, and the assimilation makes it worse as you are increasing the coarser fraction. You could explore if there is an underprediction of the dust refractive index. You could look into values provided in the literature for the region studied and compare to what WRF-Chem uses.

Response: We add a supplementary document to give the complex refractive indexes for all aerosols in this study. A part of the table is shown below. We set the dust's refractive index referring to the generic

model values in literature. The imaginary part in our study is higher than the retrieved imaginary part for the Taklimakan desert dust by Di Biagio (2019).

Table S1. Multi-wavelength real and imaginary parts of refractive indexes of aerosol chemical compositions and water in this study (a part of the snapshot of table S1)

(nm)	440	450	470	520	525	550	635	660	675	870	1020
	<i>OIN, dust (Cheng et al., 2006; Zhao et al., 2010)</i>										
Real						1.53					
Imag	0.003	0.003	0.003	0.0025	0.0025	0.002	0.0015	0.0015	0.0015	0.001	0.001

678-683. I think there is no need for this very long description of the Ma paper as these results are not that relevant to the area study as RH is likely low in the desert and dust aerosols tend to be hydrophobic  
 Response: We have removed the statements in the revision.

690-692. AOD to PM10 ratios depends on many variables. Since you are blaming discrepancies to issues in mass scattering/absorption efficiency it makes more sense to do direct comparisons to this variable as you have in-situ measurements of scattering and absorption

Response: In the revised table 4, we show the ratios of AOD, scattering/absorption coefficient to PM10 per DA experiment. In the revised section 3.3:

*“Table 4 shows the ratios of the AOD and aerosol scattering/absorption coefficients to the surface PM<sub>10</sub> concentrations. The ratio of AOD to PM<sub>10</sub> in the background model result was one-third of the observed levels. The observed mass scattering coefficient (Esca/PM<sub>10</sub>) was 1.05 Mm<sup>-1</sup> μg<sup>-1</sup> m<sup>3</sup>, while the background value was only 0.65 Mm<sup>-1</sup> μg<sup>-1</sup> m<sup>3</sup>. DA\_AOD did not eliminate the low bias but enlarged the low bias to 0.51 Mm<sup>-1</sup> μg<sup>-1</sup> m<sup>3</sup>. The same thing occurred for Eabs/PM<sub>10</sub>, which was 0.09 in the background and 0.05 in DA\_AOD, much lower than the observed value of 0.25. Figure 10 shows these mean ratios at the other wavelengths. The low bias in AOD/PM<sub>10</sub> was comparable at each wavelength. ...”*

693-696. You can assess issues with size distribution by using the angstrom exponent.

Table 2 and 3. Is there any reason behind using the lower wavelength (440-450nm) for these comparisons? Since the focus of this work is on dust, it would be preferable to compute optical properties for longer wavelengths where coarse aerosols contribute more to the scattering

Response: A new table 3 shows the angstrom exponent and SSA. The revised discussion in the main text is based on 870 nm AOD, 635 nm scattering coefficient, and 660 nm absorption coefficient.

702-706. There is extensive literature on how optical properties of dust particles deviate from Mie theory (e.g., Dubovik et al, 2006, Nousiainen et al 2015). It would be good for the authors to reference this work and attempt to explain what could be the implications of using Mie theory, and if those can explain any of the discrepancies found when assimilating multiple datasets in this study.

Response: In the revised section 3.3:

*“The irregular morphology had a significant influence on the dust simulation. Okada et al. (2001) found that the aspect ratio (the ratio of the longest dimension to its orthogonal width) of the mineral dust particles (0.1-6  $\mu\text{m}$ ) in China arid regions exhibited a median of 1.4. Dubovik et al. (2006) suggested the aspect ratio of  $\sim 1.5$  and higher in desert dust plumes. Kok et al. (2017) found that the dust’ sphericity assumption underestimated dust extinction efficiency by  $\sim 20\text{--}60\%$  for the dust particle larger than  $1\mu\text{m}$ . Tian et al. (2020) found that using a dust ellipsoid model could increase the concentration of coarse dust particle (5-10  $\mu\text{m}$ ) by  $\sim 5\%$  in eastern china and  $\sim 10\%$  in the Taklimakan area because of the decrease in gravitational settling, comparing with the simulations with dust sphericity model. Nevertheless, the aspect ratio of the spheroid dust is uncertain. Even after applying the spheroidal approximation, Soorbas et al. (2015) found that the model underestimated 550 nm aerosol scattering and backscattering values by 49% and 11%, respectively, because of the uncertainties in particle axial ratio, complex refractive index, and the particle size distribution. To date, the assumption of spherical particles has been widespread in models (including WRF-Chem) for computational efficiency. Impact of dust morphology to DA deserves a further investigation.”*

Figure 12. It would help to see an additional panel with these profiles being normalized, so we can more easily assess by how much the assimilation of the different datasets is changing the vertical distribution.

Response: The revised figure 12 has additional two panels showing the vertical distributions normalized to the surface PM<sub>x</sub> concentrations.

730 You know it overestimated PM<sub>10</sub>, not sure about aerosol number concentration (you would need a different observation for assessing that)

Response: We do not have the surface measurement of aerosol number concentration. The amounts of quality assured retrievals of aerosol columnar volume and effective radius by CE318 are limited in DAO-K (<9 days, 1 to 4 data samples per day). It is difficult to give a robust verification. The original statement describes that the GSI tends to increase the aerosol number in response to the high aerosol mass concentration. We changed the statement to:

*“The revised GSI updates aerosol number concentration according to the analyzed aerosol mass concentration and the background ratio between mass and number concentrations. Thus, an overestimation of aerosol mass concentration inclines to raise aerosol number concentration, resulting in high scattering/absorption coefficients.”*

734. Use single-scattering albedo for this

Response: We add a new table 4 to show the angstrom exponent and SSA. In the revised section 3.3:

*“Additionally, we computed the surface single scattering albedo (SSA<sub>srf</sub>) with the 525 nm scattering coefficient and 520 nm absorption coefficient. We did not use the Ångström exponent to interpolate the scattering/absorption coefficients to a similar wavelength because the AE itself had a large model bias even after DA (Table 3). The observed SSA<sub>srf</sub> value was 0.78, indicating an emphatic absorption particle,*

probably due to the mixture of anthropogenic black carbon and natural desert dust in the local air. The model background  $SSA_{srf}$  was 0.86, while the DA analyses gave even higher  $SSA_{srf}$  (0.88 to 0.9)."

738-746. This is a misconception, aerosol light extinction and AOD does not depend on sun light intensity (for instance, you can sample both at night time with different methods). What's going to change with sunlight are the radiative effects. There are likely other reasons to explain this diurnal behavior. Look into the diurnal evolution of your BEC, and also into diurnal evolution of dust reaching the city. Similar misconnection is mentioned in lines 770-771.

Response: In the revised 3.3,

*"Assimilating the AOD seems to increase the diurnal variation in the DA analyses, but this variation was not conclusive since there were different amounts of AOD data for DA at 00:00, 06:00, and 12:00. The AOD data were not always available as the data quality control (i.e., cloud screening). There was a higher increase in the concentration at noon (06:00 UTC) (Figure 9b), corresponding to a few high AOD during mild dust episodes at that hour. ..."*

The misstatement in the original lines 770-771 has been removed.

960-963. This is probably due to underprediction of dust imaginary refractive index

Response: We set the dust refractive index to refer to the generic model values in literature. The imaginary part in our study is higher than the imaginary part for the Taklimakan desert dust retrieved by Di Biagio (2019). The strong bias in absorption coefficient can be largely removed by tuning the background error of black carbon, though additional disadvantage is introduced. Please refer to the revised section 3.5.

Minor Edits

Fig 5 caption. It reads like a) and b) represent  $PM_{10}$  and winds, respectively, but I think that's not the case. Please revise

Response: The figure caption is changed to

*"Figure 5. Monthly mean  $PM_{10}$  concentration ( $\mu g m^{-3}$ ) and the streamlines of the 10-m wind ( $m s^{-1}$ ) in April (a, b) and their daily mean anomalies (c, d) ..."*

623. Did you mean "underestimates" instead of "lowered"?

Response: changed to "underestimates"

780. Do you mean "particles that absorb radiation" rather than "aborting particles"? Also, I would like black carbon in that list as well.

Response: Corrected.

781-791. I believe primary dust in WRF-Chem is also considered to be a bit absorbing (has a imaginary refractive index above 0). As mentioned in a previous comment, this number might be too low for dust in this region.

Response: In the first version manuscript, the imaginary part of dust was in the range of 0.002 to 0.001. In the revision, we increase the imaginary part to the range of 0.003 to 0.001. Our imaginary part is higher than the imaginary part for the Taklimakan desert dust retrieved by Di Biagio (2019). The strong bias when assimilating the absorption coefficient can be largely removed by tuning the background error of black carbon. Please refer to the revised section 3.5.

802-804. I disagree with this statement. If the model has biases that the assimilation is not able to correct (for instance, inaccurate real and imaginary refractive indexes) then assimilating multiple observation could also create unrealistic modifications to the model.

Response: The statements have been removed in the revision.

806-828. I wouldn't put DA\_Esca\_Eabs as an improvement over DA\_Esca, they show pretty much the same results. This means that the absorption observations are not really generating any differences in the results. Also, DA\_PMx\_AOD matches better the assimilated variables (which off course is expected) and the better agreement with scattering you happened to underpredict it with PM assimilation, and overpredict it with AOD assimilation, so assimilating both yields you something in between.

Response: Because of the problem of individual assimilation of the absorption coefficient, we remove the DA results of DA\_Esca\_Eabs and DA\_PMx\_Esca\_Eabs\_AOD and just keep the result of DA\_PMx\_AOD.

832-834. As mentioned earlier, it would be better to check this using normalized profiles. The background profiles already had aerosols up to 4km, so is likely that the assimilation is just scaling this profile upwards rather than adding a larger fraction of the mass in these layers

Response: The revised figure 12 shows the normalized profiles. In the revised section 3.7:

*"Also shown in the figure are the vertical profiles normalized to their own respective surface particulate concentrations. The assimilations not only added a larger fraction of the mass in these layers but also adjusted the shapes of the PM<sub>10</sub> profiles within 3 km above the ground (Figure 11d), following the BEC's vertical correlation length scales (Figure 3r)."*

Section 4.1. I don't think this section is very relevant, the aerosols are so dominated by dust and your BEC is constructed in a way dust aerosols will be the ones largely modified. So just briefly mentioning that the composition of these other aerosols doesn't change would do.

Response: We shorten the revised section 4.1 and present the new anthropogenic aerosols' results.

Section 4.2. Might want to discuss in this section how the large underprediction of dust absorption would impact these results.

Response: It is not easy to quantify the ADRF bias due to the weak absorption with a single WRF-Chem experiment. We admit this uncertainty and add a new paragraph in section 4:

*"It is noteworthy to say that the ADRF estimation remains uncertain even after DA. The AOD observation is only sporadically available because of cloud screening in retrieval data. The DA experiments cannot*

*eliminate the low bias in AOD in WRF-Chem. The ADRF values in the DA experiments are likely to be weaker than the plausible aerosol radiative forcing at Kashi. Neither DA experiment lowers SSAsrf to approach the observation. The observed SSAsrf (0.78) indicates likely warming forcing of aerosol at Kashi, while WRF-Chem and the DA analyses impose cooling forcing. The ADRF uncertainty is associated with the background aerosols. WRF-Chem simulates aerosol size up to 10  $\mu\text{m}$ , whereas larger particles ( $>10 \mu\text{m}$ ) exhibit substantial absorption relative to scattering in the visible wavelength (Kok et al., 2017). Anthropogenic emission inventories need an update for the year 2019, which may reduce the potential low bias in BC concentration. Additionally, the revised GSI does not concern the change in particle effective radius per size bin when calculating the aerosol number concentration in each outer loop. Low absorption cross section rises aerosol number concentration as compensation, increasing aerosol scattering coefficient too much. If our tangent operator concerns the change in particle effective radius per size bin, we can use aerosol mass and number concentration as control variables simultaneously. The DA would have a higher degree of freedom to balance the particle radius and number concentration and improve the absorption coefficient. All these need further research in the future.”*

The authors appreciate the reviewer's constructive and friendly comments. We have substantially revised the manuscript. New data and figures are present in the main text. A new supplementary document is included in the revision. We reply to the reviewer's comments point by point.

## **Anonymous Referee #2**

Received and published: 28 October 2020

The study of Chang et al. developed the GSI 3Dvar capability to assimilate AOD, scattering/absorbing coefficients for MOSAIC scheme. A few DA tests (both simultaneously and separately experiments) were conducted for northwestern China and compared with surface observations at Kashi. The authors should have spent great efforts on the system development and presented very comprehensive results.

Based on my current understanding, some more work need to be done to facilitate the readers to understand, including some essential considerations of the DA core details and the clarifications of the texts. In this way, the system would be better under-stand/promoted and readers would be more convinced.

My general comments are as below:

1. Actually GOCART is understood for the better performance of dust simulation and the relevant optical properties had been well verified; while the MOSAIC scheme is thought to be more suitable for anthropogenic emission related simulation, but the optical simulation is rather complex.

Response: Agree. The GOCART dust emission scheme is popular for dust simulation. Here, we applied the GOCART dust scheme to simulate the dust and used the MOSAIC scheme to simulate anthropogenic aerosols.

In this study, the system is developed for MOSAIC but the verification is conducted for a site in desert. This required intensive investigation of the DUST related properties representation in the MOSAIC scheme, for example,

(a) the refractive index of OIN since it is mostly treated as DUST (while there should be distinctive differences between the two);

Response: Yes, the OIN is not equivalent to dust. WRF-Chem has a dust option (dust\_opt=13) for simultaneous simulation of dust and anthropogenic aerosols with the GOCART dust scheme and the MOSAIC scheme, respectively. With this option, dust is added to OIN. Surely, this simplification is not perfect, but it did not hinder our verification of the DA system. In fact, even using the GOCART aerosol scheme, WRF-Chem computes aerosol optics with the Mie theory. Improving the dust representation in WRF-Chem needs further code development.

(b) the species partitioning (NO<sub>3</sub> is not changed in option 2 which might not be reasonable and lead to unbalanced chemistry partitioning),

Response: NO<sub>3</sub> is one of the control variables in the revision. We redid the DA experiments.

(c) the size distribution, (d) the number concentration, since the three factors determining the absorbing and scattering efficiency;

Response: We used multi-wavelength aerosol optical measurements to verify the DA system. The revised manuscript additionally shows the angstrom exponent result in Table 3.

(e) aerosol water content which are not considered but actually may change the optical properties. With very limited observational data to verify the above-mentioned information, the results in this study is really hard to interpret.

Response: Aerosol water content (AWC) is not a control variable in DA but is diagnosed in the GSI system according to the hygroscopic growth scheme, based on the analyzed aerosol dry mass concentrations. This treatment ensures the change in AWC is a physical constraint. Besides, AWC is low in the desert site and does not affect AOD a lot. In the revision, we dig the analyses by studying angstrom exponent, SSA, mass extinction coefficient. Hope the revised manuscript is convincing.

2. Some descriptions about DA core and observational data should be provided. For example, it seemed not only AOD, but also wavelength depended absorbing and scattering efficient were all assimilated, the corresponding observational operators and the errors should be given in more detail.

Response: Sorry for the confusion. The observational operators of scattering/absorption coefficient are implicitly involved in the operator of AOD in equation (3). In the revised section 2.2.3, we explicitly present the two observational operators in equation (4). We rewrote the statements about observation errors in the revised section 2.4:

*“The observation errors of PM<sub>x</sub> are handled in the conventional way (Schwartz et al., 2012; Chen et al., 2019), which contains the measurement error ( $e_1$ ) and the representative error ( $e_2$ ). The measurement error is the sum of a baseline error of  $1.5 \mu\text{g m}^{-3}$  and 0.75% of the observed PM<sub>x</sub> concentration. The representative error is the measurement error multiplied by the half-squared ratio of the grid spacing to the scale distance. The scale distance denotes the site representation in GSI and has four default values of 2, 3, 4, and 10 km, corresponding to the urban, unknown, suburban, and rural sites. We used 3 km for the scale distance in this study. As we had a single site in Kashi, it is difficult to estimate the site representation error. Since the DA analysis was based on the child model domain with a horizontal resolution of 5 km, close to the site distance to the Kashi urban area, we assumed the aerosol optical measurement had good representativeness of the model grid covering the site. The observation error of CE318 AOD took the AERONET AOD uncertainty of 0.01 in cloud-free conditions (Holben et al., 1998). The AOD observational error was further divided by the total model layer thickness in GSI.”*

Comments by lines:

1. Line 65 and other places. Adjoint operator, is it referred as TL-AD? Please clarify

Response: We corrected the statements to “tangent linear”.

2. Line 86 GIS ?

Response: Corrected to “GSI”

3. Line 100 Zang et al 2016, acutally a different DA system was used other than GSI in this study. Please check.

Response: We corrected the statements in the revised introduction:

*“Li et al. (2013) developed a 3D-Var scheme for assimilating the surface  $PM_{2.5}$  and speciated aerosol chemical concentrations for the WRF-Chem MOSAIC aerosols. Zang et al. (2016) applied this scheme to incorporate aircraft speciated aerosols in California. They proved that the assimilation of aircraft profile extended the DA benefit to aerosol forecast.”*

4. Line 181 regarding of the low anthropogenic and biogenic emissions in the desert, why not use GOCART instead?

Response: The research purpose is to introduce the new GSI system to work with the MOSAIC aerosol scheme. We used the GOCART scheme to simulate dust. In the revised section 2.1:

*“The dust emission was simulated using the GOCART dust scheme (Ginoux et al., 2001), and the dust mass was included in the OIN concentration. We performed the MOSAIC aerosol simulations with four-size bins (0.039–0.156  $\mu\text{m}$ , 0.156–0.625  $\mu\text{m}$ , 0.625–2.500  $\mu\text{m}$ , and 2.5–10.0  $\mu\text{m}$  dry diameters) for the anthropogenic aerosols.”*

5. Line 184-190. Actually the optical properties of  $\text{NH}_4\text{SO}_4$ , OC, dust, NaCl,  $\text{H}_2\text{O}$  are treated as wavelength depended in the model, this information should be investigated and provided. As it seemed that multi-wavelength aerosol scattering and absorption coefficients are assimilated. The uncertainties of the assumption in the model and observational data should be provided.

Response: In the revision, we give the complex refractive index in table S1 in the supplementary document; Section 2.2.6 describes the refractive index; The revised section 2.4 describes the observational errors; the revised section 3.3 and section 4.2 states the uncertainties associated with dust morphology and aerosol radiative forcing. Hope the revisions make the manuscript more complete.

6. Line 228. Why  $\text{NO}_3$  is not considered? In this case, it may lead to unbalanced chemistry partitioning.

Response: Nitrate is a control variable in the revision.

7. Section 2.2.3 It seemed that scattering and absorbing coefficients are also observational assimilated. Please provide details.

Response: The revised section 2.2.3 provides the observation operators of scattering/absorption coefficients.

8. Line 101: are the  $M_{i,z,k}$  in the two terms the same, maybe possibly dry and wet mass concentration respectively? If not, please clarify.

Response:  $M_{i,z,k}$  denotes the aerosol composition. It could be aerosol water content when calculating the internal mixing refractive index. In the revised section 2.2.4,

*“Note that the dry ( $r_{dry,z,k}$ ) and wet ( $r_{wet,z,k}$ ) particle radiuses are both present in Eq (21). Because aerosol water content is not a control variable,  $r_{dry,z,k}$  is used in Eq (19) and appears in Eq (21). Aerosol water*

content participates the computation of internal mixing refractive indexes, and thus  $r_{\text{wet},z,k}$  is also present in Eq (21).”

9. Line 315: is  $r_{\text{wet}}$  related with aerosol water content, considering the hygroscopicity? Any uncertainty by not considering aerosol water content. Please clarify.

Response:  $r_{\text{wet}}$  is the wet particle radius when aerosol water content (AWC) is counted in the aerosol composition. At the end of the revised section 2.2.1:

*“The AWC was diagnosed according to the analyzed aerosol mass concentration and the background relative humidity in each DA outer loop. The hygroscopic growth was calculated using the WRF-Chem code coupled with the revised GSI.”*

10. Line 352, please clarify  $m_{i,z,k}$  as dry or wet mass?

Response:  $M_{i,z,k}$  denotes the aerosol compositions. It could be aerosol water content when calculating the internal mixing refractive index.

11. Line 367. Any uncertainty by considering constant radius?

Response: It is hard to estimate the uncertainty of this constant radius in this study. Applying this constant radius is to simplify the mathematical derivation of the tangent linear operator for AOD. This simplification was applied by Saide et al. (2013). We hope to remove this assumption in the future and could discuss the relevant uncertainty.

Saide, P. E., Carmichael, G. R., Liu, Z., Schwartz, C. S., Lin, H. C., da Silva, A. M., and Hyer, E.: Aerosol optical depth assimilation for a size-resolved sectional model: impacts of observationally constrained, multi-wavelength and fine mode retrievals on regional scale analyses and forecasts, *Atmos. Chem. Phys.*, 13, 10425-10444, doi:10.5194/acp-13-10425-2013, 2013.

12. Line 703-706. Please dig more on this issue.

Response: We add a paragraph in the revised section 3.3:

*“The irregular morphology had a significant influence on the dust simulation. Okada et al. (2001) found that the aspect ratio (the ratio of the longest dimension to its orthogonal width) of the mineral dust particles (0.1–6  $\mu\text{m}$ ) in China arid regions exhibited a median of 1.4. Dubovik et al. (2006) suggested the aspect ratio of  $\sim 1.5$  and higher in desert dust plumes. Kok et al. (2017) found that the dust’ sphericity assumption underestimated dust extinction efficiency by  $\sim 20\text{--}60\%$  for the dust particle larger than  $1\mu\text{m}$ . Tian et al. (2020) found that using a dust ellipsoid model could increase the concentration of coarse dust particle (5–10  $\mu\text{m}$ ) by  $\sim 5\%$  in eastern china and  $\sim 10\%$  in the Taklimakan area because of the decrease in gravitational settling, comparing with the simulations with dust sphericity model. Nevertheless, the aspect ratio of the spheroid dust is uncertain. Even after applying the spheroidal approximation, Soorbas et al. (2015) found that the model underestimated 550 nm aerosol scattering and backscattering values by 49% and 11%, respectively, because of the uncertainties in particle axial ratio, complex refractive index, and the particle size distribution. To date, the assumption of spherical particles has been widespread in*

*models (including WRF-Chem) for computational efficiency. Impact of dust morphology to DA deserves a further investigation.”*

13. Line 765. Please investigate the uncertainties of the modeled and observed absorption coefficients.

Response: We check the differences in DA analysis as using the different imaginary part of dust refractive index and background error of BC. Please refer to the revised section 3.5.

14. Figure2. Why the domain averaged standard deviation (c) is significantly larger than that of column averages (d, e)?

Response: The vertical profiles in figure 2(c, d, e) are based on different grids. As shown in Figure 5c, Kashi and the desert point we picked up for figure 2(e) are not on the track of dust storm. Thus, the dust variations at the two points (figure 2d, e) are smaller than the average of binning standard deviation (figure 2c).

15. Figure 3. Why background error standard deviation of the OIN is two magnitudes larger than the other species? Indicating dominating contribution of dust? In this case, is it meaningful to investigate other species changes?

Response: We accidentally lowered anthropogenic aerosols in Kashi. The revised simulations correct the emissions and show that the OIN is still the predominant composition, accounting for 62% of PM<sub>2.5</sub> and 82% of PM<sub>10</sub> in April. The qualitative conclusion is the same.

16. Table 1. Please explain how the errors are determined?

Response: In the revised section 2.4:

*“The measurement error is the sum of a baseline error of  $1.5 \mu\text{g m}^{-3}$  and 0.75% of the observed PM<sub>x</sub> concentration. The representative error is the measurement error multiplied by the half-squared ratio of the grid spacing to the scale distance. The scale distance denotes the site representation in GSI and has four default values of 2, 3, 4, and 10 km, corresponding to the urban, unknown, suburban, and rural sites. We used 3 km for the scale distance in this study. As we had a single site in Kashi, it is difficult to estimate the site representation error. Since the DA analysis was based on the child model domain with a horizontal resolution of 5 km, close to the site distance to the Kashi urban area, we assumed the aerosol optical measurement had good representativeness of the model grid covering the site. The observation error of CE318 AOD took the AERONET AOD uncertainty of 0.01 in cloud-free conditions (Holben et al., 1998). The AOD observational error was further divided by the total model layer thickness in GSI.”*

1 **Improving the Sectional MOSAIC Aerosols of WRF-Chem with the revised**  
2 **Gridpoint Statistical Interpolation System and multi-wavelength aerosol optical**  
3 **measurements: DAO-K experiment 2019 at Kashi, near the Taklamakan Desert,**  
4 **northwestern China**

5  
6 Wenyuan Chang<sup>1</sup>, Ying Zhang<sup>2</sup>, Zhengqiang Li<sup>2</sup>, Jie Chen<sup>3</sup>, Kaitao Li<sup>2</sup>  
7

8  
9 <sup>1</sup> State Key Laboratory of Atmospheric Boundary Layer Physics and Atmospheric Chemistry  
10 (LAPC), Institute of Atmospheric Physics, Chinese Academy of Sciences, Beijing 100029,  
11 China.

12  
13 <sup>2</sup> [State Environment Protection Key Laboratory of Satellite Remote Sensing, Aerospace](#)  
14 [Information Research Institute](#), Chinese Academy of Sciences, Beijing 100101, China

15  
16 <sup>3</sup> National Meteorological Information Center, China Meteorological Administration, Beijing  
17 100081, China

18  
19  
20  
21  
22  
23 Corresponding authors:

24 Wenyuan Chang (changwy@mail.iap.ac.cn)

25 Zhengqiang Li (lizq@radi.ac.cn)  
26  
27

Deleted: model

29 **Abstract**

30 The Gridpoint Statistical Interpolation data assimilation (DA) system was developed for the  
31 four-size bin sectional Model for Simulating Aerosol Interactions and Chemistry (MOSAIC)  
32 aerosol mechanism in the Weather Research and Forecasting-Chemistry (WRF-Chem) model.

33 The forward and ~~tangent linear~~ operators for the aerosol optical depth (AOD) analysis were  
34 derived from WRF-Chem aerosol optical code. We applied three-dimensional variational DA  
35 to assimilate the multi-wavelength AOD, ambient aerosol scattering coefficient, and aerosol  
36 absorption coefficient, measured by the sun-sky photometer, nephelometer, and aethalometer,  
37 respectively. These were undertaken during a dust observation field campaign at Kashi in  
38 northwestern China in April 2019. The results showed that the DA analyses decreased the low  
39 biases in the model aerosols; however, it had some deficiencies. Assimilating the surface  
40 particle concentration increased the coarse particles in the dust episodes, but AOD, and the  
41 coefficients for aerosol scattering and absorption, were still lower than observed values.

42 Assimilating aerosol scattering coefficient separately from AOD improved the two optical  
43 quantities. However, it caused an overestimation of the particle concentrations at the surface.

44 Assimilating the aerosol absorption coefficient yielded the highest positive bias in the surface  
45 particle concentration, aerosol scattering coefficient, and AOD. The positive biases in the DA

46 analysis were caused by the forward operator underestimating ~~aerosol mass~~ scattering and  
47 absorption efficiency. As a compensation, the DA system increased particle concentrations

48 excessively so as to fit the observed optical values. The best overall improvements were  
49 obtained from the simultaneous assimilation of the surface particle concentration and AOD.

50 The assimilation did not substantially change the aerosol chemical fractions. After DA, the  
51 clear-sky aerosol radiative forcing at Kashi was  $-10.4 \text{ Wm}^{-2}$  at the top of the atmosphere,

52 which was 55% higher than the background radiative forcing value.

Deleted: adjoint

Deleted: particle

55 **1. Introduction**

56 Data assimilation (DA) blends the information from observations with *a priori* background  
57 fields from deterministic models to obtain an optimal analysis (Wang et al., 2001; Bannister,  
58 2017). With lagged emission inventories and unsatisfactory model chemistry mechanisms,  
59 there are notable discrepancies between model aerosols and observed levels (He et al., 2017;  
60 Chen L. et al., 2019). The DA technology incorporates aerosol measurements into the models  
61 to optimize emissions (Peng et al., 2017; Ma et al., 2019), and cyclically updates the  
62 background fields in forecasts. This effectively improves the air quality forecasts in China  
63 (Bao et al., 2019; Cheng et al., 2019; Feng et al., 2018; Hong et al., 2020; Liu et al., 2011;  
64 Pang et al., 2018; Peng et al., 2018; Xia et al., 2019a, 2019b).

65  
66 Variational DA minimizes the distant scalar function measuring the misfit between model  
67 states and a set of observations in each assimilation window. An effective variational DA  
68 requires an appropriate **tangent linear and adjoint operators**, which describes the gradient or  
69 sensitivity of the observed parameter to the control variable (Wang et al., 2001; Bannister  
70 2017). The **operator** is highly dependent on the types of assimilated observations and the  
71 selection of control variables; it is also sometimes dependent on the aerosol mechanism. For  
72 PM<sub>2.5</sub> (particulate matter with dynamic radius less than 2.5 μm) DA, the **tangent linear**  
73 operator is the ratio of the PM<sub>2.5</sub> concentration to composition of each aerosol (Pagowski et  
74 al., 2010). For the aerosol optical depth (AOD) DA, the **operator** is generated through Mie  
75 theory (Liu et al., 2011; Saide et al., 2013). With the development of aerosol mechanisms and  
76 the growing body of novel aerosol observations from ground-based networks and satellites,  
77 appropriate **tangent linear and adjoint operators** are in demand.

78  
79 The community gridpoint statistical interpolation (GSI) system (Wu et al., 2002; Purser et al.,  
80 2003a, 2003b) is often used to modify regional aerosol simulations with three-dimensional  
81 variational (3D-Var) DA. The official GSI (version 3.7 in this study) can incorporate  
82 observations of surface particulate matter concentration and AOD to constrain the aerosols  
83 simulated within the aerosol mechanism of Goddard Chemistry Aerosol Radiation and  
84 Transport (GOCART, Liu et al., 2011; Pagowski et al., 2014). The tangent linear operator and  
85 adjoint operator for AOD were determined using the Community Radiative Transfer Model  
86 (CRTM). This GSI version incorporating the Moderate Resolution Imaging  
87 Spectroradiometer (MODIS) AOD in East Asia (Liu et al., 2011) revealed the simultaneous  
88 DA effects of PM<sub>2.5</sub> and AOD in the continental United States (Schwartz et al., 2012). This  
89 **GSI** was used to identify DA effects that weakened during running of the succeeding model  
90 as the model error grew (Jiang et al., 2013), and assessed the radiative forcing of the aerosols  
91 released by wildfires (Chen et al., 2014). This version of GSI was also utilized to improve air  
92 quality forecasts in China by assimilating a variety of satellite AOD data retrieved from: the  
93 Geostationary Ocean Color Imager (Pang et al., 2018); Visible Infrared Imaging Radiometer  
94 Suite (Pang et al., 2018); Advanced Himawari-8 Imager (Xia et al., 2019a); and the Fengyun-  
95 3A/medium-resolution spectral imager (Bao et al., 2019; Xia et al., 2019b).

96  
97 Despite its capabilities, the GOCART mechanism is unable to simulate nitrate and secondary  
98 organic aerosols (SOA), and the GOCART aerosol size distribution uses a bulk assumption

Deleted: (or Jacobian matrix)

Deleted: adjoint

Deleted: adjoint

Deleted: adjoint

Deleted: GIS

104 for radiative transfer calculation. Strictly speaking, the lack of aerosol components violates  
105 the unbiased requirements for the model states in the DA system. Lack of size-segregated  
106 aerosols may introduce a bias in the calculation of optical aerosols. The official GSI can  
107 assimilate the surface particle concentration from the aerosol mechanism apart from  
108 GOCART, but its AOD DA is tightly bound with the GOCART aerosols. If one wished to use  
109 GSI to assimilate AOD for the other aerosol mechanisms, a compromise solution was to  
110 either integrate the map of the speciated aerosols of other mechanisms into that of the  
111 GOCART aerosols or use a simplified formula to convert aerosol chemical mass  
112 concentrations to AOD. For example, Tang et al. (2017) used the official GSI to assimilate  
113 MODIS AOD with the aerosols from the Community Multi-scale Air Quality Model  
114 (CMAQ). They incorporated the map of the 54 aerosol components of CMAQ into the five  
115 CRTM aerosols and repartitioned the mass increments of each CMAQ aerosol according to  
116 the ratio of aerosol chemical components in the background field. This repartitioning is called  
117 the “ratio approach.” Cheng et al. (2019) assimilated the lidar extinction coefficient profiles  
118 measured in Beijing to modify the Weather Research and Forecasting-Chemistry (WRF-  
119 Chem) Model for Simulating Aerosol Interactions and Chemistry (MOSAIC) aerosols. They  
120 used the ratio approach to map eight MOSAIC aerosols based on five GOCART aerosols.  
121 This mapping strategy is readily implemented but introduces inconsistent size-segregated  
122 aerosol information (e.g., hygroscopicity and extinction efficiency) between the aerosol  
123 model and the DA system. Kumar et al. (2019) analyzed the CMAQ aerosols by assimilating  
124 MODIS AOD with GSI. Their forward operator converted aerosol chemical composition into  
125 AOD based on the well-known IMPROVE aerosol extinction model (Malm and Hand, 2007).  
126 The IMPROVE model predicts AOD with a linear combination of aerosol chemical masses,  
127 with the hydrophilic particles multiplied by a tuning factor associated with relative humidity.  
128 Because building a GSI system for a new aerosol mechanism is quite technical, the official  
129 GSI for the GOCART aerosols is still a primary choice for recent aerosol DA studies (Bao et  
130 al., 2019; Xia et al., 2019; Hong et al., 2020).

131  
132 Because of the shortcomings, the official GSI has been extended to cooperate with other  
133 aerosol mechanisms in WRF-Chem. The MOSAIC mechanism in WRF-Chem simulates  
134 aerosol mass and number concentrations in either four- or eight-size bins. This sectional  
135 aerosol mechanism involves nitrate chemistry and can simulate SOA with the volatility basis  
136 set scheme. Li et al. (2013) developed a 3D-Var scheme for assimilating the surface  $PM_{2.5}$  and  
137 speciated aerosol chemical concentrations for the WRF-Chem MOSAIC aerosols. Zang et al.  
138 (2016) applied this scheme to incorporate aircraft speciated aerosols in California. They  
139 proved that the assimilation of aircraft profile extended the DA benefit to aerosol forecast.  
140 Saide et al. (2013) proposed a revised GSI version that performed variational DA for the  
141 MOSAIC aerosols. The authors generated the adjoint operator code with the automatic  
142 differentiation tool (ADT), TAPENADE v3.6. The ADT used the chain rule of derivative  
143 calculus on the AOD source code in WRF-Chem. They assimilated multi-source AOD data  
144 with the MOSAIC aerosols over continental United States and found that incorporating multi-  
145 wavelength fine-mode AOD redistributed the aerosols’ particulate mass concentration sizes.  
146 The revised GSI system assimilated Korean ground-based and geostationary satellite AOD  
147 datasets to improve local aerosol simulations (Saide et al., 2014, 2020). Pang et al. (2020)

Deleted: (Zang et al., 2016)

149 developed the official GSI to work with the Modal Aerosol Dynamics Model for Europe with  
150 the Secondary Organic Aerosol Model (MADE/SORGAM) aerosols in WRF-Chem. The  
151 authors used the WRF-Chem AOD code as the forward operator to calculate the essential  
152 aerosol optical properties, which were then inputted to the CRTM adjoint operator. Because  
153 aerosols were externally mixed in CRTM, the setting of the internal mixture per size bin in  
154 WRF-Chem was not taken into account, and the AOD of each aerosol component was  
155 calculated separately.

156  
157 This study provides a solution to improve the capability of the GSI 3D-Var DA system for the  
158 sectional MOSAIC aerosols in WRF-Chem. We designed the ~~tangent linear~~ operator code for  
159 AOD DA based on the WRF-Chem intrinsic aerosol optical subroutine (Fast et al., 2006), that  
160 is, without using the ADT. The ~~operator~~ code is programmed based on the analytical  
161 equations of the linear tangent model for AOD. As our revised GSI does not use the CRTM  
162 module, it avoids the problem of needing to eliminate WRF-Chem aerosols characteristics  
163 (e.g., aerosol mixture state and size distribution) to meet the CRTM input requirements. The  
164 forward and ~~tangent linear~~ operators are coordinated, since they are derived from the same  
165 WRF-Chem code, and are written in a single subroutine, which is coupled to the GSI at the  
166 place of invoking CRTM for the AOD calculation. In addition to AOD DA, our ~~tangent linear~~  
167 operator has two variants to assimilate the aerosol scattering and absorption coefficients,  
168 measured using a nephelometer and aethalometer, respectively.

169  
170 This study verifies the effectiveness of our revised GSI system by incorporating multi-  
171 wavelength aerosol optical observations that were measured during an international field  
172 campaign, the Dust Aerosol Observation-Kashi, in April 2019 at Kashi city, neighboring the  
173 Taklamakan Desert, northwestern China. This desert is the second largest globally, and is the  
174 primary source of dust aerosols in East Asia. The dust from the desert affects the nearby  
175 Tibetan Plateau (Ge et al., 2014; Jia et al., 2015; Zhao et al., 2020), air quality and climate in  
176 East Asia (Huang et al., 2014), and the biogeochemical cycles in the western Pacific Ocean  
177 (Calil et al., 2011). A successful DA analysis will help improve the local air quality forecast  
178 and enhance our understanding of the environmental impacts of local dust storms. The  
179 remainder of this paper is organized as follows. Section 2 describes the revised GSI system,  
180 the experimental design, and the observed data. Section 3 presents the DA results when  
181 assimilating different observations. Section 4 discusses the impact of DA on aerosol chemical  
182 composition and aerosol direct radiative forcing. Finally, Section 5 provides the conclusions  
183 and limitations that need further research.

## 184 **2. Methodology and Data**

### 185 **2.1 Forecast Model**

186  
187 The background aerosol fields were simulated using the WRF-Chem model version 4.0 (Grell  
188 et al., 2005; Fast et al., 2006). The model configurations included the Purdue Lin  
189 microphysics scheme (Chen and Sun, 2002), the unified Noah land surface model (Tewari et  
190 al., 2004), the Yonsei University scheme for planetary boundary layer meteorological  
191 conditions (Hong et al., 2006), and the rapid radiative transfer model for general circulation  
192 models (RRTMG) scheme for shortwave and longwave radiation (Iacono et al., 2008). The

Deleted: adjoint

Deleted: adjoint

Deleted: adjoint

Deleted: adjoint

197 gas-phase chemistry was simulated using the carbon bond mechanism (Zaveri and Peters,  
 198 1999), including aqueous-phase chemistry. The aerosol chemistry was simulated using the  
 199 MOSAIC mechanism (Zaveri et al., 2008), which simulated sulfate, nitrate, ammonium, black  
 200 carbon (BC), organic carbon (OC), sodium, calcium, chloride, carbonate, and other inorganic  
 201 matter (OIN, e.g., trace metals and silica). SOA was excluded from our experiments to  
 202 accelerate model integration. Although ignoring that SOA biased the model, the influence was  
 203 assumed to be small, based on low anthropogenic and biogenic emissions in the vicinity of the  
 204 desert. The dust emission was simulated using the GOCART dust scheme (Ginoux et al.,  
 205 2001), and the dust mass was included in the OIN concentration. We performed the MOSAIC  
 206 aerosol simulations with four-size bins (0.039–0.156  $\mu\text{m}$ , 0.156–0.625  $\mu\text{m}$ , 0.625–2.500  $\mu\text{m}$ ,  
 207 and 2.5–10.0  $\mu\text{m}$  dry diameters) for the anthropogenic aerosols. The sectional aerosol data in  
 208 the hourly model output were the aerosol dry mass mixing ratios of chemical compositions,  
 209 aerosol number concentration, and aerosol water content. The aerosol compositions included  
 210 hydrophilic particulates (i.e.,  $\text{SO}_4^{2-}$ ,  $\text{NO}_3^-$ ,  $\text{NH}_4^+$ ,  $\text{Cl}^-$ ,  $\text{Na}^+$ ) and hydrophobic particulates (i.e.,  
 211 BC, OC, and OIN). We used the spherical particulate assumption and computed the aerosol  
 212 optics according to the Mie theory. The aerosol compositions were internally mixed in each  
 213 size bin and were externally mixed between the size bins. The internal mixing refractive index  
 214 was the volume-weighted mean refractive index of each composition. The WRF-Chem model  
 215 computed the aerosol optics at 300, 400, 600, and 999 nm and interpolated the aerosol optical  
 216 parameters (AOD, SSA, asymmetry factor) to eleven shortwave lengths with Ångström  
 217 exponents for the radiative transfer calculation.

## 219 2.2 Assimilation System

220 The revised GSI DA system is based on the official GSI ([https://dtcenter.org/community-](https://dtcenter.org/community-code/gridpoint-statistical-interpolation-gsi)  
 221 [code/gridpoint-statistical-interpolation-gsi](https://dtcenter.org/community-code/gridpoint-statistical-interpolation-gsi), Wu et al., 2002; Liu et al., 2011; Schwartz et al.,  
 222 2012; Pagowski et al., 2014) version 3.7. The 3D-Var DA minimizes the cost function:

$$224 \quad J(\mathbf{x}) = \frac{1}{2}(\mathbf{x} - \mathbf{x}_b)^T \mathbf{B}^{-1}(\mathbf{x} - \mathbf{x}_b) + \frac{1}{2}(H(\mathbf{x}) - \mathbf{y})^T \mathbf{R}^{-1}(H(\mathbf{x}) - \mathbf{y}) \quad (1)$$

227 where  $\mathbf{x}$  is the state vector composed of the model control variables; the subscript  $b$  denotes  
 228 that  $\mathbf{x}$  is the background state vector;  $\mathbf{y}$  is the vector of the observations;  $H$  is the forward  
 229 operator or observation operator that transfers the gridded control variables into the observed  
 230 quantities at the observation locations; and  $\mathbf{B}$  and  $\mathbf{R}$  are the background and observation error  
 231 covariance matrices, respectively.

233 The official GSI version only works with the GOCART aerosols for assimilating the surface-  
 234 layer  $\text{PM}_{2.5}$  and  $\text{PM}_{10}$  (denoted as  $\text{PM}_x$  in the context) concentrations, and the 550 nm MODIS  
 235 AOD. Our revised GSI system assimilates  $\text{PM}_x$  concentrations, multi-wavelength aerosol  
 236 scattering/absorption coefficients, and AOD. Figure 1 shows the workflow of our DA system.  
 237 According to the AOD calculation in WRF-Chem, we can either choose the aerosol number  
 238 concentration (option 1), or aerosol mass concentration (option 2) as control variables. Option

Moved (insertion) [2]

Moved (insertion) [1]

Deleted: determination and aerosol optical calculation

Moved up [2]: The dust emission was simulated using the GOCART dust scheme (Ginoux et al., 2001).

Moved up [1]: The dust mass was included in the OIN concentration determination and aerosol optical calculation.

244 1 is described in Li et al. (2020). In this study, we selected option 2, which is described in the  
245 following subsections.  
246

Figure 1

### 247 248 **2.2.1 Control Variables**

249 The control variables in this study were the mass mixing ratio of composition of each aerosol  
250 per size bin, which corresponded to the WRF-Chem output data only. This set therefore  
251 differed from previous studies that lumped aerosols per size bin as control variables. The  
252 lumped aerosols avoided the burdensome task of specifying the background error statistics for  
253 numerous aerosols (Li et al., 2013; Pagowski et al. 2014). Although our control variables  
254 could have been further optimized, here we designed the control variable using only those that  
255 substantially contributed to the total mass concentrations. We set the control variables of six  
256 aerosol mass mixing ratios of  $\text{SO}_4^{2-}$ ,  $\text{NH}_4^+$ ,  $\text{NO}_3^-$ , OC, BC, and OIN per size bin. Chlorine,  
257 and sodium had miniscule background concentrations and remained the background values in  
258 the DA analysis. There were twenty-four control variables in total for the four-size bin  
259 simulations. In Kashi's case near the desert, the OIN was predominant, accounting for 62% of  
260  $\text{PM}_{2.5}$  and 82% of  $\text{PM}_{10}$ .

261 Our design of the control variables was different from the AOD assimilation in Saide et al.  
262 (2013), with theirs being the natural logarithm of the total mass mixing ratio per size bin,  
263 multiplied by the thickness of the model layer. As the high model layer had a significant layer  
264 thickness with low aerosol concentrations, the multiplication offset the opposite effects of  
265 increasing layer thickness versus decreasing concentrations with increase in altitude. This  
266 multiplication prevented the addition of many modifications for the high model layers, where  
267 aerosols were low in concentration. The logarithmic transformation was used to decrease the  
268 extensive value range in the control variables caused by multiplication. Since the AOD value  
269 is often smaller than one, this leads to a significant negative logarithm value and a relatively  
270 unconstrained DA system. Saide et al. (2013) introduced two weak constraints in their cost  
271 function to cut off the user-defined "extraordinarily high" and "extraordinarily low"  
272 concentrations. They repartitioned the increments of the total mass per size bin for  
273 composition of each aerosol, with the background aerosol chemical mass fractions. Here,  
274 neither the logarithmic transformation, nor the multiplication using layer thickness was set in  
275 our DA system. Our control variable was restricted to the WRF-Chem output variable, and the  
276 DA system changed the composition of each aerosol per size bin, depending on the aerosol  
277 background errors.  
278

279 Consistent with the set by Pang et al. (2020), aerosol water content (AWC) was not one of the  
280 control variables in our GSI. Otherwise, the AWC might have increased contrary to the  
281 physical constraints for the loading of hydrophilic particles, and simply as a mathematical  
282 artefact. The AWC was diagnosed according to the analyzed aerosol mass concentration and  
283 the background relative humidity in each DA outer loop. The hygroscopic growth was  
284 calculated using the WRF-Chem code coupled with the revised GSI.  
285  
286

**Deleted:** In the case of Kashi situated near the desert, the OIN was predominant, accounting for ~99% of the total particle mass concentrations. The control variable could thus have exclusively comprised the OIN. However, because we were curious about the response of aerosol chemical fractions in the DA constraint, w

**Deleted:** five

**Deleted:** Nitrate, c

**Deleted:** , and the time cost for the DA calculation for these variables was acceptable

**Moved (insertion) [3]**

**Moved up [3]:** Saide et al. (2013) repartitioned the increments of the total mass per size bin for composition of each aerosol, with the background aerosol chemical mass fractions. Our control variable

### 2.2.2 Tangent Linear Operator for PM<sub>x</sub>

The PM<sub>10</sub> is the sum of all aerosol dry mass concentrations over the size bins, and the sum of the first three is the PM<sub>2.5</sub> (Chen et al., 2019; Wang et al., 2020). Accordingly, the tangent linear operator for PM<sub>x</sub> is the gradient of the PM<sub>x</sub> concentration to the aerosol chemical mass concentration per size bin:

$$\frac{\delta[PM_x]}{\delta[C_{aer,k}]}, k = 1, \dots, n_{size} \quad (2)$$

where  $n_{size}$  is the number of size bins and is equal to four in this study;  $[\cdot]$  denotes the mass concentration ( $\mu\text{g m}^{-3}$  for PM<sub>x</sub>);  $C_{aer,k}$  is the aerosol mass mixing ratio ( $\mu\text{g kg}^{-1}$ ) of  $\text{SO}_4^{2-}$ ,  $\text{NO}_3^-$ ,  $\text{NH}_4^+$ , OC, BC, and OIN at the  $k$ -th size bin. Because we did not multiply the chemical mass with a scaling factor to represent some unknown compositions in the summation of PM<sub>x</sub>, Eq (2) always equals one. It means that we equally distribute the PM<sub>x</sub> increment to each aerosol composition per size bin. The PM<sub>2.5</sub> and PM<sub>10</sub> are assimilated in the same way. When the fine and coarse particles are assimilated simultaneously, we assimilate the concentration of PM<sub>2.5</sub> and the coarse particulate (PM<sub>10</sub>-PM<sub>2.5</sub>).

### 2.2.3 Forward Operator for Aerosol Optics in WRF-Chem

We used the original forward operator in WRF-Chem for the aerosol optical parameters (Fast et al., 2006). AOD is calculated as a function of wavelength according to Mie theory. The columnar AOD  $\tau$  is the sum of layer AOD across the  $n_z$  model layers:

$$\tau = \sum_{z=1}^{n_z} \tau_z = \sum_{z=1}^{n_z} \sum_{k=1}^{n_{size}} e_{ext,z,k} \cdot n_{z,k} \cdot H_z \quad (3)$$

where  $e_{ext,z,k}$  is the extinction cross section of a single mixing particle in the  $k$ -th size bin at the  $z$ -th model layer,  $n_{z,k}$  is the aerosol number concentration, and  $H_z$  is the layer thickness. At the surface, the ambient aerosol scattering ( $E_{sca}$ ) and absorbing ( $E_{abs}$ ) coefficients that are measured by the nephelometer and aethalometer, respectively, are represented in the model as

$$E_{sca} = \sum_{k=1}^{n_{size}} e_{sca,1,k} \cdot n_{1,k}$$

$$E_{abs} = \sum_{k=1}^{n_{size}} e_{abs,1,k} \cdot n_{1,k} \quad (4)$$

where  $e_{sca,1,k}$  and  $e_{abs,1,k}$  are the scattering and absorption cross section of a particle at the surface. There is a relationship:

Deleted: Adjoint

Deleted: adjoint

Deleted: The threshold of aerosol mass mixing ratio that yields the non-zero adjoint operator is  $0.01 \mu\text{g kg}^{-1}$ .

Deleted: AOD

343  
344  
345  
346  
347  
348  
349  
350  
351  
352  
353  
354  
355  
356  
357  
358  
359  
360  
361  
362  
363  
364  
365  
366  
367  
368  
369  
370  
371  
372  
373  
374  
375  
376  
377  
378  
379  
380  
381

$$e_{ext,z,k} = e_{sca,z,k} + e_{abs,z,k} \quad (5)$$

The extinction cross section  $e_{ext,z,k}$  of a wet particle with radius  $r_{wet,z,k}$  is:

$$e_{ext,z,k} = p_{ext,z,k} \cdot \pi \cdot r_{wet,z,k}^2 \quad (6)$$

where  $p_{ext,z,k}$  is the extinction efficiency, given the desired mixing refractive indexes and the wet particle radius. The  $p_{ext,z,k}$  is attained through the Chebyshev polynomial interpolation:

$$p_{ext,z,k} = \exp \left\{ \sum_{j=1}^{n_{coef}} c_{ch}(j) \cdot c_{ext,z,k}(j) \right\} \quad (7)$$

where  $c_{ch}$  is the coefficient of  $n_{coef}$  order Chebyshev polynomials,  $c_{ext,z,k}$  is the polynomial value for the extinction efficiency of the particle, which is an internal mixture of all aerosol compositions (i.e., the control variables plus chlorine, sodium, and AWC). The radius in the AOD subroutine code is in a logarithmic transform to handle the broad particle size range from 0.039  $\mu\text{m}$  to 10  $\mu\text{m}$ . The exponential function in Eq. (7) transforms the logarithm radius back to the normal radius. The aerosol number concentration  $n_{z,k}$ , and the aerosol dry (wet) mass concentration  $m_{i,z,k}$  have a linkage through the dry (wet) particle radius  $r_{dry,z,k}$  ( $r_{wet,z,k}$ ) and the density  $\rho_i$  of each aerosol chemical composition:

$$n_{z,k} = \sum_{i=1}^{n_{wet,aer}} \frac{m_{i,z,k}}{\rho_i} \cdot \frac{3}{4\pi \cdot r_{wet,z,k}^3} = \sum_{i=1}^{n_{dry,aer}} \frac{m_{i,z,k}}{\rho_i} \cdot \frac{3}{4\pi \cdot r_{dry,z,k}^3} \quad (8)$$

Both the dry and wet particle radius will appear in the tangent linear operator. The difference between the second and the third terms in Eq (8) is whether aerosol water content is counted.  $n_{wet,aer}$  is the number of aerosol chemical composition plus aerosol water content ( $n_{wet,aer} = n_{dry,aer} + 1$ ).

#### 2.2.4 Tangent Linear Operator Developed for AOD

As per the forward operator in Eq. (3) in WRF-Chem, we developed the tangent linear operator for AOD, which requires the derivative of  $\tau$  in Eq. (3) to the aerosol dry mass concentration (aerosol water content is not a control variable),  $m_{i,z,k}$ :

$$\frac{\delta\tau}{\delta m_{i,z,k}} = \frac{\delta\tau_z}{\delta m_{i,z,k}} = \frac{\delta e_{ext,z,k} \cdot n_{z,k} \cdot H_z}{\delta m_{i,z,k}} + \frac{e_{ext,z,k} \cdot \delta n_{z,k} \cdot H_z}{\delta m_{i,z,k}} + \frac{e_{ext,z,k} \cdot n_{z,k} \cdot \delta H_z}{\delta m_{i,z,k}} \quad (9)$$

Deleted: coefficient

Deleted: nitrate,

Deleted: Adjoint

Deleted: adjoint

386 The first term on the righthand side of Eq. (9) indicates the change in AOD as the perturbation  
 387 of extinction cross section. According to Eq. (6), considering that the particle radius is  
 388 constant,  $\delta e_{ext,z,k}$  is represented as:

$$389 \quad \delta e_{ext,z,k} = \delta p_{ext,z,k} \cdot \pi \cdot r_{wet,z,k}^2 \quad (10)$$

392 where  $\delta ch(j) = 0$  assuming that the particle radius is constant. [This assumption simplifies](#)  
 394 [the tangent linear operator and is also employed in Saide et al. \(2013\).](#)

396 Equation (10) is expanded with the derivative of Eq. (7):

$$398 \quad \delta p_{ext,z,k} = p_{ext,z,k} \cdot \left\{ \sum_{j=1}^{n_{coef}} c_{ch}(j) \cdot \delta c_{ext,z,k}(j) \right\} \quad (11)$$

400 By expanding  $\delta c_{ext,z,k}$  in Eq. (11), we have:

$$402 \quad \delta c_{ext,z,k}(j) = \delta w_{00} \cdot E_{ext,00}(j) + \delta w_{01} \cdot E_{ext,01}(j) + \delta w_{10} \cdot E_{ext,10}(j) + \delta w_{11} \cdot E_{ext,11}(j) \quad (12)$$

404 where the four parameters of  $E_{ext}$  indicate the extinction efficiencies in the Mie [lookup](#) table  
 406 surrounding the point with the desired mixing refractive indexes, and the wet particle radius.  
 407 The interpolation weights  $\delta w$  are determined as:

$$409 \quad \delta w_{00} = (v-1)\delta u + (u-1)\delta v \quad \delta w_{01} = (1-v)\delta u - u\delta v$$

$$410 \quad \delta w_{10} = (1-u)\delta v - v\delta u \quad \delta w_{11} = u\delta v + v\delta u \quad (13)$$

413 where

$$415 \quad u = \frac{R_{mix} - R_{low}}{R_{up} - R_{low}} \quad \delta u = \frac{\delta R_{mix}}{R_{up} - R_{low}}$$

$$416 \quad v = \frac{I_{mix} - I_{low}}{I_{up} - I_{low}} \quad \delta v = \frac{\delta I_{mix}}{I_{up} - I_{low}} \quad (14)$$

419 In Eq. (14),  $R_{mix}$  and  $I_{mix}$  are the aerosol volume-weighted mean real and imaginary [parts of](#)  
 420 [complex](#) refractive indices, respectively.  $R_{up}$  ( $I_{up}$ ) and  $R_{low}$  ( $I_{low}$ ) are the nearest upper and  
 421 lower limits for  $R_{mix}$  ( $I_{mix}$ ) in the Mie table. Considering  $V_{wet,z,k}$  is the volume of all aerosol [dry](#)  
 422 masses [plus aerosol water content](#), the real and imaginary parts and their derivatives are:

$$424 \quad R_{mix,z,k} = \sum_{i=1}^{n_{wet,aer}} R_i \cdot \frac{m_{i,z,k}}{\rho_i \cdot V_{wet,z,k}} \quad \delta R_{mix,z,k} = \frac{R_i}{\rho_i \cdot V_{wet,z,k}} \cdot \delta m_{i,z,k}$$

$$I_{mix,z,k} = \sum_{i=1}^{n_{wet,aer}} I_i \cdot \frac{m_{i,z,k}}{\rho_i \cdot V_{wet,z,k}} \quad \delta I_{mix,z,k} = \frac{I_i}{\rho_i \cdot V_{wet,z,k}} \cdot \delta m_{i,z,k} \quad (15)$$

where

$$V_{wet,z,k} = \sum_{i=1}^{n_{wet,aer}} \frac{m_{i,z,k}}{\rho_i} \quad (16)$$

Put Eq. (12), Eq. (13) into Eq. (11) leads to:

$$\delta p_{ext,z,k} = [(v-1)\alpha_{sca,00} + (1-v)\alpha_{sca,01} - v\alpha_{sca,10} + v\alpha_{sca,11}] \delta u + [(u-1)\alpha_{abs,00} - u\alpha_{abs,01} + (1-u)\alpha_{abs,10} + u\alpha_{abs,11}] \delta v \quad (17)$$

where

$$\begin{aligned} \alpha_{sca,00} &= p_{sca,1,k} \cdot \sum_{j=1}^{n_{coef}} c_{ch}(j) \cdot E_{sca,00}(j) & \alpha_{sca,01} &= p_{sca,1,k} \cdot \sum_{j=1}^{n_{coef}} c_{ch}(j) \cdot E_{sca,01}(j) \\ \alpha_{sca,10} &= p_{sca,1,k} \cdot \sum_{j=1}^{n_{coef}} c_{ch}(j) \cdot E_{sca,10}(j) & \alpha_{sca,11} &= p_{sca,1,k} \cdot \sum_{j=1}^{n_{coef}} c_{ch}(j) \cdot E_{sca,11}(j) \\ \alpha_{abs,00} &= p_{abs,1,k} \cdot \sum_{j=1}^{n_{coef}} c_{ch}(j) \cdot E_{abs,00}(j) & \alpha_{abs,01} &= p_{abs,1,k} \cdot \sum_{j=1}^{n_{coef}} c_{ch}(j) \cdot E_{abs,01}(j) \\ \alpha_{abs,10} &= p_{abs,1,k} \cdot \sum_{j=1}^{n_{coef}} c_{ch}(j) \cdot E_{abs,10}(j) & \alpha_{abs,11} &= p_{abs,1,k} \cdot \sum_{j=1}^{n_{coef}} c_{ch}(j) \cdot E_{abs,11}(j) \end{aligned} \quad (18)$$

The subscripts of *sca* and *abs* in Eq. (17) and (18) denote “scattering” and “absorption”, respectively. The first term on the righthand side of Eq. (9) is determined using Eq. (10) and Eq. (17). The second term on the righthand side of Eq. (9) indicates the linkage of the aerosol number and mass concentrations. It is the derivative of [dry particle in](#) Eq. (8) by assuming a constant radius:

$$\delta n_{z,k} = \frac{3 \cdot \delta m_{i,z,k}}{4\pi \cdot r_{dry,z,k}^3 \cdot \rho_i} \quad (19)$$

The third term on the righthand side of Eq. (9) contains the derivative of the layer thickness to the concentrations in this layer. This indicates that the light attenuation length based on per

456 unit concentration, which can be intuitively represented by the ratio of layer thickness to the  
 457 aerosol mass concentration in this layer. Putting Eq. (10) and Eq. (19) into Eq. (9), we have  
 458 the original formula of the tangent linear operator for AOD for the aerosol dry mass  
 459 concentration:

$$\begin{aligned}
 461 & \\
 462 & \frac{\delta\tau}{\delta m_{i,z,k}} = \frac{\delta\tau_z}{\delta m_{i,z,k}} = \frac{\delta e_{ext,z,k} \cdot n_{z,k} \cdot H_z}{\delta m_{i,z,k}} + \frac{e_{ext,z,k} \cdot \delta n_{z,k} \cdot H_z}{\delta m_{i,z,k}} + \frac{e_{ext,z,k} \cdot n_{z,k} \cdot \delta H_z}{\delta m_{i,z,k}} = \\
 463 & \{[(v-1)\alpha_{sca,00} + (1-v)\alpha_{sca,01} - v\alpha_{sca,10} + v\alpha_{sca,11}] \cdot \frac{\pi \cdot r_{wet,z,k}^2 \cdot R_i \cdot n_{z,k} \cdot H_z}{\rho_i \cdot V_{wet,z,k} \cdot (R_{up,z,k} - R_{low,z,k})} \\
 464 & + \\
 465 & [(u-1)\alpha_{abs,00} - u\alpha_{abs,01} + (1-u)\alpha_{abs,10} + u\alpha_{abs,11}] \cdot \frac{\pi \cdot r_{wet,z,k}^2 \cdot I_i \cdot n_{z,k} \cdot H_z}{\rho_i \cdot V_{wet,z,k} \cdot (I_{up,z,k} - I_{low,z,k})} + \\
 466 & \frac{3e_{ext,z,k} \cdot H_z}{4\pi \cdot r_{dry,z,k}^3 \cdot \rho_i} + \frac{e_{ext,z,k} \cdot n_{z,k} \cdot H_z}{m_{i,z,k}} \} \cdot \beta \\
 467 & \\
 468 & \tag{20}
 \end{aligned}$$

470 where  $\beta$  is the factor that changes the unit of mass from  $\mu\text{g kg}^{-1}$  to  $\mu\text{g m}^{-3}$ . The last righthand  
 471 term in Eq. (20) may not have a quick convergence in the DA outer loops because the aerosol  
 472 mass concentration  $m_{i,z,k}$  in the denominator often has a low bias, which introduces an error  
 473 into the operator. The error is amplified by the layer thickness  $H_z$  in the numerator. Thus, the  
 474 operator of Eq. (20) cannot lead to a stable analysis. For this reason, we changed the operator  
 475 to account for the columnar mean aerosol extinction coefficient which is described as follows:

$$\begin{aligned}
 477 & \frac{\delta(\overline{e_{ext} \cdot n})}{\delta m_{i,z,k}} = \frac{H_z}{\sum H_z} \cdot \frac{\delta(e_{ext,z,k} \cdot n_{z,k})}{\delta m_{i,z,k}} = \frac{H_z}{\sum H_z} \cdot \left[ \frac{\delta e_{ext,z,k} \cdot n_{z,k}}{\delta m_{i,z,k}} + \frac{e_{ext,z,k} \cdot \delta n_{z,k}}{\delta m_{i,z,k}} \right] = \\
 478 & \{[(v-1)\alpha_{sca,00} + (1-v)\alpha_{sca,01} - v\alpha_{sca,10} + v\alpha_{sca,11}] \cdot \frac{\pi \cdot r_{wet,z,k}^2 \cdot R_i \cdot n_{z,k}}{\rho_i \cdot V_{wet,z,k} \cdot (R_{up,z,k} - R_{low,z,k})} \\
 479 & + \\
 480 & [(u-1)\alpha_{abs,00} - u\alpha_{abs,01} + (1-u)\alpha_{abs,10} + u\alpha_{abs,11}] \cdot \frac{\pi \cdot r_{wet,z,k}^2 \cdot I_i \cdot n_{z,k}}{\rho_i \cdot V_{wet,z,k} \cdot (I_{up,z,k} - I_{low,z,k})} + \\
 481 & \frac{3e_{ext,z,k}}{4\pi \cdot r_{dry,z,k}^3 \cdot \rho_i} \} \cdot \beta \cdot \frac{H_z}{\sum H_z} \\
 482 & \\
 483 & \tag{21}
 \end{aligned}$$

485 In Eq. (21), the operator is based on the extinction coefficient at each layer, weighted by the  
 486 layer thickness normalized to the total model layer thickness. Correspondingly, the AOD  
 487 observations and AOD observation error are divided by the total layer thickness at the

Deleted: adjoint

Deleted: adjoint

Deleted: adjoint

Deleted: adjoint

492 observation location. Note that the dry ( $r_{dry,z,k}$ ) and wet ( $r_{wet,z,k}$ ) particle radii are both  
 493 present in Eq (21). Because aerosol water content is not a control variable,  $r_{dry,z,k}$  is used in Eq  
 494 (19) and appears in Eq (21). Aerosol water content participates the computation of internal  
 495 mixing refractive indexes, and thus  $r_{wet,z,k}$  is also present in Eq (21). Equation (21) is the final  
 496 tangent linear operator for AOD DA in this study.

Deleted: adjoint

## 498 2.2.5 Tangent Linear Operator Developed for Surface Aerosol Attenuation Coefficients

Deleted: Adjoint

499 The aerosol scattering and absorption coefficients measured by the nephelometer and  
 500 aethalometer, respectively, are similar to the aerosol extinction coefficient at the surface in  
 501 Eq. (21). Neither of the two coefficients address the layer thickness. The operator for the  
 502 aerosol scattering coefficient measured by nephelometer is described as follows:

Deleted: adjoint

$$505 \frac{\delta(e_{sca,1,k} \cdot n_{1,k})}{\delta m_{i,1,k}} = \{[(v-1)\alpha_{sca,00} + (1-v)\alpha_{sca,01} - v\alpha_{sca,10} + v\alpha_{sca,11}]$$

$$506 \cdot \frac{\pi \cdot r_{wet,1,k}^2 \cdot R_i \cdot n_{1,k}}{\rho_i \cdot V_{wet,1,k} \cdot (R_{up,1,k} - R_{low,1,k})} + \frac{3e_{sca,1,k}}{4\pi \cdot r_{dry,1,k}^3 \cdot \rho_i}\} \cdot \beta$$

504 (22)

507 where the symbols have the same meaning as before, and the subscript one in Eq. (22)  
 508 denotes the surface layer. The operator for the aerosol absorption coefficient measured by  
 509 aethalometer is

Deleted: adjoint

$$513 \frac{\delta(e_{abs,1,k} \cdot n_{1,k})}{\delta m_{i,1,k}} = \{[(u-1)\alpha_{abs,00} - u\alpha_{abs,01} + (1-u)\alpha_{abs,10} + u\alpha_{abs,11}]$$

$$514 \cdot \frac{\pi \cdot r_{wet,1,k}^2 \cdot I_i \cdot n_{1,k}}{\rho_i \cdot V_{wet,1,k} \cdot (I_{up,1,k} - I_{low,1,k})} + \frac{3e_{abs,1,k}}{4\pi \cdot r_{dry,1,k}^3 \cdot \rho_i}\} \cdot \beta$$

512 (23)

515 As shown in the operators, the gradients of the aerosol mass concentrations rely on the aerosol  
 516 number concentration; meanwhile, the number concentration is estimated according to the  
 517 mass concentration and the particle radius. The two concentrations are intertwined in the DA  
 518 system, indicating the nonlinearity of the operator. This nonlinearity is handled with a  
 519 succeeding minimization of the cost function within the GSI. That is, the cost function is first  
 520 minimized with the number concentration in the background field, and the number  
 521 concentration is updated with the first analyzed aerosol mass concentrations. In the second  
 522 minimization, the number concentration assessed in the first analysis constructs a new  
 523 operator value, resulting in a new analysis of mass concentrations. This iterative process is  
 524 denoted as the “outer loop,” which is repeated several times to attain the final analysis  
 525 (Massart et al., 2010). We set ten maximum iterations to handle the nonlinearity in the  
 526 operator. The cost function in most analyses reaches the minimum in two or three outer loops.

Deleted: adjoint

Deleted: adjoint

Deleted: adjoint

Deleted: adjoint

528 The WRF-Chem AOD code is coupled into the GSI subroutine at the place of invoking  
 529 CRTM. The tangent linear operators of Eq. (21), Eq. (22), and Eq. (23) are simultaneously  
 530 determined in the subroutines, which are cyclically invoked in the outer loops within the GSI.

Deleted: AOD and the adjoint

### 541 **2.2.6 Aerosol Complex Refractive Indexes in GSI**

542 Table S1 in the supplementary document shows the complex refractive indexes for each  
543 aerosol chemical composition in the revised GSI. The refractive indexes are for eleven  
544 wavelengths, including four for CE318, three for nephelometer, three for aethalometer, and  
545 one for 550 nm MODIS AOD (not assimilated in this study). The real parts of refractive  
546 indexes of sulfate, nitrate, and ammonium are similar and refer to Toon et al.'s (1976) data.  
547 The real part is 1.53 at 440 nm and decreases to 1.52 at 1020 nm. The refractive indexes of  
548 OC and BC are constant across the wavelengths, being  $1.55-0.001i$  for OC (Chen and Bond,  
549 2010) and  $1.95-0.79i$  for BC (Bond and Berstrom, 2006). The dust refractive index's real part  
550 is a constant value of 1.54 (Zhao et al., 2010). The dust refractive index's imaginary part  
551 depends on the dust mineralogy, size distribution, and shape, which are associated with the  
552 dust sources. The imaginary part varies a lot at the same dust source. Cheng et al. (2006)  
553 reported the desert dust refractive index in winter and spring at Dunhuang, a city adjacent to  
554 the northeast side of the Taklamakan desert. Their imaginary part value was approximately in  
555 the ranges of 0.0008 to 0.0028 at 440 nm, 0.0006 to 0.0030 at 670 nm, 0.0005 to 0.0036 at  
556 870 nm, and 0.0005 to 0.0040 at 1020 nm (See Figure 9 in their paper). Recently, Di Biagio et  
557 al. (2019) retrieved the dust's imaginary part in the Taklimakan desert's north edge (41.83°N,  
558 85.88°E). Their dust imaginary part decreased from  $0.0018\pm 0.0008$  at 370 nm to  
559  $0.0005\pm 0.0002$  at 950 nm, much lower than the generic values in climate models. The  
560 imaginary part's retrieval uncertainty is related to the iron oxide in dust samples, the cutoff  
561 coarse particle size ( $<10\ \mu\text{m}$  in Di Biagio et al., 2019), and the assumption of spherical  
562 particles applied in the retrieval algorithm. Here, we admit the high uncertainty and use the  
563 imaginary part following the generic model values (Table S1), which are higher than the  
564 upper limits of the data of Di Biagio et al. (2019) and are close to the values of Cheng et al.  
565 (2006). The desert dust has a stronger absorption at shortwave wavelengths. The refractive  
566 index of a wavelength without exact literature data uses the nearby wavelength's data in  
567 literature. The supplement also shows the aerosol density (Table S2) that follows the density  
568 data in Barnard et al. (2010). The aerosol density is necessitated to compute aerosol optical  
569 parameters in the AOD forward operator and construct our tangent linear operator.

### 570 **2.3 Background Error Covariance (BEC)**

571 Many aerosol DA studies used the National Meteorological Center (NMC) method (Parrish  
572 and Derber, 1992) to model the BEC matrix. The NMC method uses long-term archived  
573 weather data that are created in the forecast cycles. It computes the statistical differences  
574 between two forecasts with different leading lengths (e.g., 24 h and 48 h), but which are valid  
575 at the same time. The NMC method is workable because solving global weather forecasts is  
576 an initial value problem of mathematical physics. That is, a slight difference in the initial  
577 atmospheric state would lead to a substantially different prediction, because of the chaos in  
578 the atmosphere. However, a regional model is a boundary value problem. Meteorological  
579 reanalysis data drive the regional chemistry simulation, and the driving data quality affects the  
580 simulation (Giorgi and Mearns, 1999). The WRF-Chem simulations in the NMC method only  
581 reflected the influences of using different initial conditions. As the model runs, the influence  
582 of the initial conditions becomes weak, while the influence of lateral boundary conditions  
583 always takes effect. Because the same reanalysis data drive the paring regional model

585 simulations, the following lateral boundary conditions for the simulations of the two leading-  
586 lengths are similar. This leads to a limited regional model difference when using the NMC  
587 method. That is, the NMC method's BEC on the meteorology would underestimate the  
588 aerosol error in WRF-Chem. Kumar et al. (2019) assimilated AOD in the contiguous United  
589 States based on the NMC method's BEC. They perturbed the background emissions by adding  
590 the gridded mean differences of four emission inventories. Their analysis with the BEC  
591 accounting for meteorology and emissions uncertainties reduced the AOD bias by 38%,  
592 superior to 10% bias reduction counting the meteorology uncertainty alone.

**Deleted:** We speculate that the NMC method cannot fully represent the model biases in emission inventories

**Deleted:** and model chemistry, underestimate the aerosol error in WRF-Chem.

593  
594 Some aerosol DA studies have created background error variance using the ensemble  
595 simulations by randomly disturbing model lateral boundary conditions and surface emissions  
596 (Peng et al., 2017; Ma et al., 2020). The ensemble experiments better represent the model  
597 error, but significantly increase the computational burden. Here, we used the standard  
598 deviation of hourly aerosol concentrations in April in the background field (first guess field)  
599 to represent the background error variance. The rationale of this approach is that the Tarim  
600 Basin acts as a “dust reservoir” and traps dust particles for a period, before being carried long-  
601 distance by wind (Fan et al., 2020). The model bias in dust dominates the model aerosol error,  
602 and is correlated with the aerosol variation as the weather fluctuates. The model bias is small  
603 on clear days when the aerosol concentration is low. Conversely, the bias is large when the  
604 mean concentration is high: that is, on heavily-polluted days. Because the mean aerosol  
605 concentration correlated positively with the aerosol variation, we used the standard deviation  
606 of aerosol concentration to represent the background aerosol error. This approach was similar  
607 to Sič et al. (2016), who set a percentage of the first guess field for the background error  
608 variance. Our approach prioritizes DA modification of aerosols which have high background  
609 mean concentrations.

610  
611 We calculated the statistics of the background error, including the aerosol standard deviation  
612 and the horizontal and vertical correlation length scales, using the GENerate the Background  
613 Errors (GEN-BE) software (Descombes et al., 2015), based on the one-month hourly aerosol  
614 concentrations in WRF-Chem. We obtained the statistics of four static BECs for the four DA  
615 analysis hours (i.e., 00:00, 06:00, 12:00, and 18:00 UTC), respectively. The DA procedures  
616 for the April 2019 data repeatedly use the statistics of the background error at the  
617 corresponding analysis time. A usual strategy to enrich the samples of model results for  
618 calculating the statistics is to gather model grid points with similar characteristics of the  
619 atmosphere, referred to as “binning.” The statistics are spatially averaged over the binned grid  
620 points. The default strategy in the GEN\_BE for GSI is latitude-binning, which creates a  
621 latitude-dependent error correlation function (Figure 2a). The latitude binning is generally  
622 used for latitude flow dependency and works for large and global domains (Wu et al., 2002).  
623 However, we found that using the latitude-binning strategy overestimated the surface PM<sub>x</sub>  
624 concentration when assimilating aerosol optical observations. One reason for this was related  
625 to the model bias in particle extinction efficiency, as discussed in Section 3.3. Another  
626 plausible reason is related to the vertical profile of the background model error. The  
627 maximum dust error occurred at the surface of the desert (Figure 2e) because of the local dust  
628 emission sources, but the maximum error at Kashi was at the dust transporting layer above the

633 surface (Figure 2d). Owing to the vast extent of the Taklamakan Desert, the latitude-binning  
634 suppressed the local error characteristics at Kashi, and led to a vertical error profile (Figure  
635 2c) similar to that over the desert (Figure 2e).

636  
637 For this reason, we used the standard deviation of the control variable at each model grid to  
638 replace the latitude-binning standard deviation. The horizontal and vertical correlation length  
639 scales were calculated based on the latitude-binning data. Figure 3 shows the background  
640 error statistics generated by the GEN\_BE software, which provided the input to the GSI. The  
641 OIN component showed high background errors in the third and fourth particle sizes at the  
642 transporting layer above the surface (Figure 3f). The aerosol compositions related to  
643 anthropogenic emissions (i.e., sulfate, nitrate, ammonium, OC, and BC, referred to here as  
644 'anthropogenic aerosols') had maximum errors in the second particle size and showed the  
645 greatest vertical error at the surface. The background error for OIN composition was higher  
646 than that for anthropogenic aerosols by a factor of two or three, because of the high  
647 background dust concentration in the city.

648  
649 The horizontal and vertical correlation length scales determine the range of observation  
650 innovations spreading from the observation locations. The horizontal influences had small  
651 changes in altitude within the lowest 15 model layers (below a height of ~5 km), indicating  
652 that the dust transport layer was well-mixed in the lower atmosphere. This deep dust layer  
653 was consistent with the dust simulation by Meng et al. (2019). They showed that the dust in  
654 spring was vertically mixed in a thick boundary layer to a height of 3–5 km in the Tarim  
655 Basin. The vertical correlation length scales first increased from low values at the surface, to  
656 high values at ~2.5 km in height (for the 8–9 layers), indicating that strong winds yielded  
657 intense aerosol upward flux. The vertical correlation length scale quickly decreased from the  
658 maximum value, with further increase in altitude corresponding to the large particle gradient  
659 at the upper edge of the transporting layer. The latter was associated with laminar air motion  
660 during the dust storm.

661  
662 The background model errors were independent of particle size, which would have tended to  
663 accumulate the DA modification in a single size bin that had the maximum background error  
664 (e.g., the OIN in the fourth particle size). To avoid excessive accumulation of increments in a  
665 single size bin, we added a one-dimensional recursive filter for the background covariances of  
666 control variables across the size bins within the GSI. The inter-size bin correlation length  
667 scale was four bin units.

668  
669 Figure 2, Figure 3

#### 670 2.4 Observational Data and Errors

671 The Dust Aerosol Observation–Kashi field campaign was performed at Kashi from  
672 00:00UTC 25 March to 00:00 UTC 1 May 2019. The site was placed in the Kashi campus of  
673 the Aerospace Information Research Institute, Chinese Academy of Sciences (39.50°N,  
674 75.93°E; Li et al., 2018), about 4 km in the northwest to the Kashi city. The site aerosol  
675 observations used for our DA analysis included: (1) the multi-wavelength AOD measured by

Deleted: for the OIN component

Deleted: standard deviation for the other compositions and the

Deleted: . aerosol compositions showed vertical error profiles, greatest at the surface (Figures 3a-d).

Deleted: , as per the setting of Saide et al. (2013)

682 the sun-sky photometer (Cimel CE318); (2) the multi-wavelength aerosol scattering and  
683 absorption coefficients at the surface, measured with a nephelometer (Aurora 3000) and  
684 aethalometer (Magee AE-33), respectively, during the campaign; and (3) the hourly PM<sub>2.5</sub> and  
685 PM<sub>10</sub> observations, measured with a METONE BAM-1020 continuous particulate monitor.  
686 All the instruments were deployed at the roof of a three stories height building on the campus.  
687 Please refer to Li et al. (2020) for more details about the field campaign.

688  
689 Table 1 summarizes the observation periods, the wavelengths of the aerosol optical data, and  
690 the observation errors. The multi-wavelength data of each type of observation were  
691 assimilated simultaneously. The observation errors of PM<sub>x</sub> are handled in the conventional  
692 way (Schwartz et al., 2012; Chen et al., 2019), which contains the measurement error ( $e_1$ ) and  
693 the representative error ( $e_2$ ). The measurement error is the sum of a baseline error of  $1.5 \mu\text{g}$   
694  $\text{m}^{-3}$  and 0.75% of the observed PM<sub>x</sub> concentration. The representative error is the  
695 measurement error multiplied by the half-squared ratio of the grid spacing to the scale  
696 distance. The scale distance denotes the site representation in GSI and has four default values  
697 of 2, 3, 4, and 10 km, corresponding to the urban, unknown, suburban, and rural sites. We  
698 used 3 km for the scale distance in this study. As we had a single site in Kashi, it is difficult to  
699 estimate the site representation error. Since the DA analysis was based on the child model  
700 domain with a horizontal resolution of 5 km, close to the site distance to the Kashi urban area,  
701 we assumed the aerosol optical measurement had good representativeness of the model grid  
702 covering the site. The observation error of CE318 AOD took the AERONET AOD  
703 uncertainty of 0.01 in cloud-free conditions (Holben et al., 1998). The AOD observational  
704 error was further divided by the total model layer thickness in GSI. It is difficult to determine  
705 instrumental errors in nephelometers and aethalometers, and we empirically set their  
706 instrumental errors to  $10 \text{ Mm}^{-1}$ , equivalent to the magnitude of the Rayleigh extinction  
707 coefficient. The observational errors were uncorrelated, with  $\mathbf{R}$  being a diagonal matrix.

Table 1
---------

709

## 710 2.5 Experimental Design

711 The WRF-Chem simulations were configured in a two-nested domain centered at 82.9 °E,  
712 41.5 °N. The coarse domain was a 120×100 (west-east × north-south) grid with a horizontal  
713 resolution of 20 km that covered the Taklamakan Desert, and the fine domain was an 81×61  
714 grid with a resolution of 5 km, focusing on Kashi and environs (Figure 4a). Both domains had  
715 41 vertical levels extending from the surface to 50 hPa. The lowest model layer at the site was  
716 approximately 25-meter height from the ground. The two domains were two-way coupled.  
717 The parent domain covered the entire dust emission source, providing dust transport fluxes at  
718 the lateral boundaries of the fine domain. The aerosol radiative effect was set to provide  
719 feedback on the meteorology. The indirect effect of aerosols was not set in the experiments.  
720 Initial and lateral boundary meteorological conditions for WRF-Chem were the one-degree  
721 resolution of the National Centers for Environmental Prediction Final Analysis data created  
722 by the Global Forecast System model. The meteorological lateral boundary conditions for the  
723 coarse domain were updated every six hours, and were linearly interpolated between the  
724 updates in WRF-Chem. We did not set the chemical boundary conditions for the coarse

725 domain. The Multiresolution Emission Inventory of China (MEIC) for the year 2010  
726 (www.meicmodel.org) provided anthropogenic emission levels. The yearly emission  
727 differences in 2010-2019 may bias the aerosol chemical simulation, but this bias is hard to be  
728 quantified as lack of aerosol chemical observations in this city. As the significant pollutant at  
729 Kashi is dust, we just ignore the model uncertainties due to the yearly differences in  
730 anthropogenic emission inventories. The biogenic emission levels were estimated online  
731 using the Model of Emissions of Gases and Aerosols from Nature (Guenther et al., 2006).  
732 Wildfire emissions were not set in the experiments.

733  
734 We conducted a one-month WRF-Chem simulation for April 2019, starting at 00:00 UTC 27  
735 March and discarding the first five days for spin-up. The revised GSI system modified the  
736 aerosols in the fine domain at 00:00, 06:00, 12:00, and 18:00 UTC each day starting from  
737 00:00 UTC 1 April until the end of the month. We assimilated the observations four times a  
738 day because the reanalyzed meteorological data were available for the four time slices, which  
739 facilitated the model restarting from the DA analyses. The hourly PM<sub>x</sub> observations were  
740 assimilated at the exact time of analysis. The observed AOD and aerosol scattering/absorption  
741 coefficients were assimilated when they fell within 3 hours before the time of analysis. Table  
742 2 shows the DA experiments. The literal meanings of the experimental names denote the  
743 observations that were individually or simultaneously assimilated. To study the impact of DA  
744 on aerosol direct radiative forcing (ADRF), we modified the WRF-Chem code to calculate the  
745 shortwave irradiance with and without aerosols at each model integration step. The modified  
746 WRF-Chem model restarted from each DA analysis and ran to the next analysis time. Each  
747 running performed the radiation transfer calculation twice, and each calculation saw the  
748 aerosols and clean air, respectively. The irradiance difference between the two pairing calls  
749 was aerosol radiative forcing. Section 4.2 shows the DA effects on the clear-sky ADRF  
750 values.

**Deleted:** we restarted the WRF-Chem model from each DA analysis, which then ran to the next analysis time.

751 

Table 2, Figure 4
-------------------

752

### 753 3. Results

#### 754 3.1 Evaluation of Control Experiment

755 Table 2 shows the monthly mean values and correlations between the observed data and the  
756 model results. The statistical values were based on the pairing data between the model results  
757 and the observations. Figures 6 show the surface PM<sub>x</sub> concentrations, aerosol scattering  
758 coefficients, and AOD when assimilating the observations at 00:00, 06:00, 12:00, and 18:00  
759 UTC each day in April.

**Deleted:** absorption

760

761 Kashi is in the junction between the Tian Shan Mountains to the west and the Taklamakan  
762 Desert to the east (Figure 5a). In the Tarim Basin, the prevailing surface wind is easterly or  
763 northeasterly, which raises dust levels and carries the particles westward (Figure 5b). An  
764 intense dust storm hit the city at noon on 24 April 2019, with a peak PM<sub>10</sub> concentration  
765 exceeding 3,000 μg m<sup>-3</sup>. The dust storm travelled across the northern part of the desert and  
766 carried the dust particles to Kashi and the mountainous area (Figure 5c, d). A few mild dust  
767 storms occurred at Kashi on April 3–5, April 8–11, and April 14–17 (Figure 6b), and the

771 maximum PM<sub>10</sub> concentrations were in the range of 400–600 μgm<sup>-3</sup>. The time series of PM<sub>2.5</sub>,  
772 aerosol scattering/absorption coefficient, and AOD showed patterns, similar to those for PM<sub>10</sub>  
773 (Figure 6).

774  
775 WRF-Chem captured the main dust episodes, but significantly underestimated the aerosols at  
776 Kashi (Table 2). The background monthly mean concentrations of PM<sub>2.5</sub> and PM<sub>10</sub> were 17%  
777 and 41% lower than the observed values, respectively, with a low correlation ( $R < 0.3$ ). The  
778 simulated dust storm on 24 April was a mild dust event and had a maximum PM<sub>10</sub> of ~300 μg  
779 m<sup>-3</sup>, one-tenth of the observed value. The model underestimates the aerosol  
780 scattering/absorption coefficients and AOD by 40–70%.

781  
782 The OIN component accounted for the model bias in PM<sub>10</sub> on dusty days. Zhao et al. (2020)  
783 proposed that the GOCART scheme reproduced dust emission fluxes under conditions of  
784 weak wind erosion but underestimated the emissions in conditions of strong wind erosion. We  
785 did not assimilate meteorology. The model bias in the surface wind introduces errors in dust  
786 emission, and places bias on the number of dust particles entering the city. In the non-dust  
787 days with the PM<sub>10</sub> lower than the 25<sup>th</sup> percentile PM<sub>10</sub> in April, the model hourly PM<sub>2.5</sub> on  
788 average only accounted for 60% of the observed data levels. The PM<sub>2.5</sub> low bias could be due  
789 to the lack of SOA chemistry in our experiments and the emission low bias in the residential  
790 sector which is a major source of anthropogenic emissions for PM<sub>2.5</sub>, BC, and OC in the  
791 developing western area. The residential sector accounts for 36–82% of these emissions,  
792 according to the MEIC emission inventory (Li et al., 2017) and is the primary source of  
793 uncertainty in anthropogenic emissions inventories in China.

Deleted: simulated anthropogenic aerosols were probably too low to be reasonable for this city.

Figure 5

795

### 796 3.2 Assimilating PM<sub>2.5</sub> and PM<sub>10</sub> Concentrations

797 Simultaneous assimilation of the observed PM<sub>x</sub> (DA\_PM<sub>x</sub>) improved both the fine and  
798 coarse particle concentrations, with a substantial improvement in the third and fourth particle  
799 sizes of the OIN composition (Figure 8f). The analyzed monthly mean PM<sub>10</sub> increased to  
800 329.3 μg m<sup>-3</sup>, with a high correlation of 0.99. The analyzed monthly mean PM<sub>2.5</sub> was  
801 improved to 89.3 μg m<sup>-3</sup>, although it was still lower than the observed levels, with a high  
802 correlation of 0.89. The low bias in PM<sub>2.5</sub> and the high bias in PM<sub>10</sub> in the analyses were both  
803 mainly in the dust storm on 24–25 April (Figure 6a,d). Applying the inter-size bin correlation  
804 length caused the interlinked analyses of PM<sub>2.5</sub> and PM<sub>10</sub>. In the desert area, the coarse and  
805 fine dust are readily affected by the magnitude of BEC of the fourth size-bin OIN (oin\_a04).  
806 We intentionally decreased the BEC of oin\_a04 by 10% each time to 30% of its original  
807 value. The magnitude of 30% of oin\_a04 was comparable to the magnitude of the third size-  
808 bin (oin\_a03) OIN's background error. As shown in Table S3, because the oin\_a04's BEC  
809 reduction relaxes the constraint on the coarse particle, the PM<sub>10</sub> bias becomes more negative  
810 along with the decrease in oin\_a04's BEC. Meanwhile, the PM<sub>2.5</sub> bias becomes more positive.  
811 Correspondingly, the ratio of PM<sub>2.5</sub> to PM<sub>10</sub> was exaggerated to 0.33 with 30% of oin\_a04's  
812 BEC, higher than the observed value of 0.28. Overall, the original BEC of oin\_a04 is a  
813 reasonable tradeoff in our DA experiments. The inter-size bin correlation length tunes the

816 cross size-bin modifications, and it indeed does matter to the DA performance compared with  
817 those without inter-size bin correlation. Although the correlation length of four in our DA  
818 experiment is a little bit arbitrary, we found that the impact on the analysis due to using  
819 different correlation length is almost ignorable.

820  
821 The DA system preferentially modified the coarse particle concentrations because of the  
822 coarse particles's high background model error according to our BEC modeling strategy.  
823 Intuitively, our modification that mainly focused on the highest concentration of coarse  
824 particles was reasonable. It decreased the model biases by raising the heaviest loading  
825 aerosols. As a result, the ratio of PM<sub>2.5</sub> to PM<sub>10</sub> decreased from 0.39 in the background to 0.27  
826 in DA\_PMx, approaching the observed ratio of 0.28. Such improvement was consistent with  
827 the correction required to the model desert dust in literature. Kok et al. (2011) found that  
828 regional and global circulation models underestimate the fraction of emitted coast dust (>~5  
829 µm), overestimates the fraction of fine dust (<2µm diameter). Adebisi and Kok (2020)  
830 claimed that too rapid deposition of coarse dust out of the atmosphere accounts for the  
831 missing coarse dust in models. Similarly, WRF-Chem assimilated too much smaller dust  
832 particles than the observed. According to Kashi's AOD between 440 nm and 1020 nm, the  
833 observed Ångström exponent (AE) was 0.18 in this case, but the background value was 0.54  
834 (Table 3). DA\_PMx reduced the AE value to 0.30, a little improvement but not sufficient.

835  
836 As the particle concentration increased, the 635 nm aerosol scattering coefficient in DA\_PMx  
837 moderately increased to 170.4 Mm<sup>-1</sup>, with a high correlation of 0.89, still lower than the  
838 observed level of 231.5 Mm<sup>-1</sup>. The analyzed 660 nm absorption coefficient was 15.8 Mm<sup>-1</sup>,  
839 67% lower than observed levels, with a correlation of 0.42. The analyzed AOD showed a  
840 monthly mean value of 0.38 in DA\_PMx, 42% lower than observed levels, with a low  
841 correlation of 0.35.

Deleted: The improvements in the analyzed absorption coefficients and AOD were insufficient (Figures 6d-e).

842  
843 Figure 9a shows the diurnal concentrations of PM<sub>10</sub> in the analyses in April. The observed  
844 PM<sub>10</sub> showed a substantial variation at 18:00 UTC, the (local midnight). This substantial  
845 nocturnal variation was partly owing to the dust storm that started on 24 April and ended the  
846 next day. This midnight variation was also related to a nocturnal low-level jet. Ge et al.  
847 (2016) pointed out that there was a nocturnal low-level jet at a height of 100–400 m, with a  
848 wind speed of 4–10 m s<sup>-1</sup> throughout the year in the Tarim Basin. They stressed that the low-  
849 level jet broke down in the morning, transporting its momentum toward the surface, and  
850 increased dust emissions. The nocturnal low-level jet increased the possibility of dust  
851 particles moving towards the city at night, causing a high PM<sub>10</sub> variation at 18:00 UTC. The  
852 diurnal changes in the DA analyses followed the observed levels, but had higher mean values.

### 853 3.3 Assimilating AOD

854  
855 Assimilating AOD (DA\_AOD) improved the monthly mean 870 nm AOD to 0.59,  
856 approaching to the observed value of 0.66, with a high correlation of 0.98 (Figure 6u). The  
857 monthly mean PM<sub>2.5</sub> was improved to 92.6 µg m<sup>-3</sup>, quite close to the observed level of 91 µg  
858 m<sup>-3</sup>, but the analyzed PM<sub>10</sub> was 541.7 µg m<sup>-3</sup>, 68% higher than the observed value. The DA  
859 system improved the AOD at the price of deteriorating the data quality of surface coarse

862 particle concentrations. Surface particle overestimations have been reported in previous  
863 studies (Liu et al., 2011; Ma et al., 2020; Saide et al., 2020). In the arid area of Kashi, the ratio  
864 of PM<sub>2.5</sub> to PM<sub>10</sub> therefore reduced to 0.17 in DA AOD, which was too far comparing with  
865 the observed ratio of 0.28.

Deleted: , opposite to the result when assimilating PMx

866 The revised GSI updates aerosol number concentration according to the analyzed aerosol  
867 mass concentration and the background ratio between mass and number concentrations. Thus,  
868 an overestimation of aerosol mass concentration inclines to raise aerosol number  
869 concentration, resulting in high scattering/absorption coefficients. In Kashi, the analyzed 635  
870 nm scattering coefficient in DA AOD was 222.6 Mm<sup>-1</sup>, slightly lower than the observed  
871 value. The analyzed 660 nm absorption coefficient was 17.0 Mm<sup>-1</sup>, 64% lower than the  
872 observed value. It indicates that WRF-Chem strongly underestimated the  
873 scattering/absorption cross section. This underestimation resulted in too many coarse particles  
874 as compensation to fit the observed AOD, and hence decreased the PM<sub>2.5</sub>/PM<sub>10</sub> ratio further.

875  
876  
877 Table 4 shows the ratios of the AOD and aerosol scattering/absorption coefficients to the  
878 surface PM<sub>10</sub> concentrations. The ratio of AOD to PM<sub>10</sub> in the background model result was  
879 one-third of the observed levels. The observed mass scattering coefficient (Esca/PM<sub>10</sub>) was  
880 1.05 Mm<sup>-1</sup> μg<sup>-1</sup> m<sup>3</sup>, while the background value was only 0.65 Mm<sup>-1</sup> μg<sup>-1</sup> m<sup>3</sup>. DA AOD  
881 did not eliminate the low bias but enlarged the low bias to 0.51 Mm<sup>-1</sup> μg<sup>-1</sup> m<sup>3</sup>. The same  
882 thing occurred for Eabs/PM<sub>10</sub>, which was 0.09 in the background and 0.05 in DA AOD,  
883 much lower than the observed value of 0.25. Figure 10 shows these mean ratios at the other  
884 wavelengths. The low bias in AOD/PM<sub>10</sub> was comparable at each wavelength. All DA  
885 experiments yielded close bias in extinction/scattering/absorption efficiency. Such low bias in  
886 AOD/PM<sub>10</sub> imposed the DA system to overestimate the PM<sub>10</sub> to fit the observed AOD data.

Deleted: a model low bias in particle scattering/absorption efficiency

887  
888 Additionally, we computed the surface single scattering albedo (SSAsrf) with the 525 nm  
889 scattering coefficient and 520 nm absorption coefficient. We did not use the Ångström  
890 exponent to interpolate the scattering/absorption coefficients to a similar wavelength because  
891 the AE itself had a large model bias even after DA (Table 3). The observed SSAsrf value was  
892 0.78, indicating an emphatic absorption particle, probably due to the mixture of anthropogenic  
893 black carbon and natural desert dust in the local air. The model background SSAsrf was 0.86,  
894 while the DA analyses gave even higher SSAsrf (0.88 to 0.9).

895  
896 The low bias in mass scattering/absorption efficiency is related to the aerosol optical module,  
897 which is based on Mie theory in WRF-Chem. First, the simulations used four-size bin particle  
898 segregation. This coarse size representation aggregated many aerosols in the accumulation  
899 mode (Figure 8f). Because small particles have a strong of light attenuation capability,  
900 according to the Mie theory, too many coarse particles would not effectively increase the  
901 AOD. Saide et al. (2020) linked the aerosol optics to the size bin representation (from 4 to 16  
902 bins) for hazes in South Korea. They showed that WRF-Chem underestimated the dry aerosol  
903 extinction, and the underestimation could be relieved when using a finer size bin than four.  
904 Okada and Kai (2004) found that the dust particle radius in the Taklamakan Desert was in the

908 range of 0.1–4  $\mu\text{m}$ , indicating the dominant fine-mode particles in the desert. Using the four-  
909 size bin would simultaneously obtain better analyses of both AOD and PM<sub>x</sub>.

911 Second, the dust particles are irregular in shape (Okada and Kai, 2004), while the spherical  
912 particle is a common assumption for the aerosol optics in the Mie theory in current models,  
913 which is an essential source of uncertainty in the forward operator of WRF-Chem when the  
914 assumption of spherical particles for dust fails. The irregular morphology had a significant  
915 influence on the dust simulation. Okada et al. (2001) found that the aspect ratio (the ratio of  
916 the longest dimension to its orthogonal width) of the mineral dust particles (0.1–6  $\mu\text{m}$ ) in  
917 China arid regions exhibited a median of 1.4. Dubovik et al. (2006) suggested the aspect ratio  
918 of ~1.5 and higher in desert dust plumes. Kok et al. (2017) found that the dust sphericity  
919 assumption underestimated dust extinction efficiency by ~20–60% for the dust particle larger  
920 than 1  $\mu\text{m}$ . Tian et al. (2020) found that using a dust ellipsoid model could increase the  
921 concentration of coarse dust particle (5–10  $\mu\text{m}$ ) by ~5% in eastern china and ~10% in the  
922 Taklimakan area because of the decrease in gravitational settling, comparing with the  
923 simulations with dust sphericity model. Nevertheless, the aspect ratio of the spheroid dust is  
924 uncertain. Even after applying the spheroidal approximation, Soorbas et al. (2015) found that  
925 the model underestimated 550 nm aerosol scattering and backscattering values by 49% and  
926 11%, respectively, because of the uncertainties in particle axial ratio, complex refractive  
927 index, and the particle size distribution. To date, the assumption of spherical particles has  
928 been widespread in models (including WRF-Chem) for computational efficiency. Impact of  
929 dust morphology to DA deserves a further investigation.

931 To reduce the overestimate in PM<sub>x</sub> concentrations, we set the gridded standard deviation in  
932 place of the latitude-binning standard deviation, as discussed in Section 2.3. Figure 11 shows  
933 the analyzed vertical profiles of PM<sub>x</sub> concentrations. Higher PM<sub>10</sub> concentrations were  
934 observed in the low atmosphere than at the surface. These vertical error profiles decreased the  
935 surface PM<sub>10</sub> particles and tended to increase the PM<sub>2.5</sub>/PM<sub>10</sub> ratio, contrary to the effects of  
936 low model bias in particle extinction efficiency. For the net effect of the compensation, the  
937 mass extinction efficiency in the analysis was still almost equivalent to the background value  
938 (Table 4). That is, our tuned BEC vertical profile at Kashi, to some extent canceled out the  
939 effects of other model error sources (e.g., the positive bias in the coarse particle of BEC, and  
940 the low bias in extinction efficiency) but was not sufficient to increase the mass extinction  
941 efficiency to the observed value. Finer aerosol size representation and a better advanced  
942 aerosol optical calculation for dust are essential solutions.

943 ↓  
944 Assimilating the AOD seems to increase the diurnal variation in the DA analyses, but this  
945 variation was not conclusive since there were different amounts of AOD data for DA at 00:00,  
946 06:00, and 12:00. The AOD data were not always available as the data quality control (i.e.,  
947 cloud screening). There was a higher increase in the concentration at noon (06:00 UTC)  
948 (Figure 9b), corresponding to a few high AOD during mild dust episodes at that hour. The DA  
949 system had to raise the PM<sub>10</sub> to fit the observed high AOD values. Because the CE318 AOD  
950 was only available in the daytime, none DA analysis was performed at 18:00. Also, due to the  
951 limited AOD data, assimilating AOD did not substantially increase the correlation of PM<sub>x</sub>.

**Deleted:** ¶

Another reason for the low ratio of AOD to PM<sub>10</sub> is related to our approach for modeling BEC. It is important to remember that our BEC represents the possible error effects owing to model bias in aerosols. The coarse particle accounts for a large mass portion of PM<sub>x</sub>, and its bias dominates the model error. we cannot say that this background error assessment is unbiased. As our BEC gave a high background error to the coarse particle for its sufficient concentration, the DA system tended to increase PM<sub>10</sub>, which was not as effective in increasing AOD as PM<sub>2.5</sub>. If the background error of the coarse particle were too high, the BEC would falsely lower the ratio of AOD to PM<sub>10</sub> in the analysis. ¶

**Deleted:** and the possible high bias in the BEC values of coarse particles

**Deleted:** ratio

**Deleted:** ratio

**Deleted:** ¶

Because the DA system overestimated the aerosol number concentration, resulting in a positive bias in PM<sub>10</sub>, This indicates that WRF-Chem strongly underestimated the single-particle absorption efficiency, and the low bias was too strong to be compensated by the overestimated aerosol number concentration. the analyzed aerosol scattering coefficient was overestimated up to 280.1 Mm<sup>-1</sup>, 37% higher than the observed value. In contrast, the analyzed absorption coefficient was 23.1 Mm<sup>-1</sup>, 72% lower than the observed value. also indicates that WRF-Chem strongly underestimated the single-particle absorption efficiency, and the low bias was too strong to be compensated by the overestimated aerosol number concentration. ¶

**Deleted:** . At the hot time of the day, intense sunlight increased the light extinction by the particles

**Deleted:** At dawn (00:00 UTC) or dusk (12:00 UTC), when the sunlight was weak, the DA modifications were small, and the DA increases in the PM<sub>10</sub> fell to low levels. However, because the AOD constraint was only available in the daytime and the AOD DA data were not always available as the data quality control (i.e., cloud screening),

991 The analyzed PM<sub>2.5</sub> and PM<sub>10</sub> still had low correlations with the observed levels  
992 ( $R=0.31\sim 0.35$ ).

993

### 994 3.4 Assimilating Aerosol Scattering Coefficient

995 Assimilating the aerosol scattering coefficient (DA\_Esca) yielded overall analyses similar to  
996 the phenomenon in DA\_AOD. The analyzed 635 nm scattering coefficient ( $192.1 \text{ Mm}^{-1}$ ) was  
997 lower than the observation ( $231.5 \text{ Mm}^{-1}$ ), with a high correlation of 0.97. The analyzed  
998 monthly mean AOD was 0.53, better than the AOD of 0.38 when assimilating PMx.

999 However, the surface particle concentrations were overestimated (i.e., positive biases by 14%  
1000 for PM<sub>2.5</sub>, and 37% for PM<sub>10</sub>), with a substantial increase in the coarse particle of OIN.

1001 Overestimations appeared during a few mild dust episodes (Figure 7d). This again indicated  
1002 that WRF-Chem underestimated the dust scattering efficiency, in accordance with the low  
1003 bias in the ratio of the scattering coefficient to PM<sub>10</sub> ( $0.52 \text{ Mm}^{-1} \mu\text{g}^{-1} \text{ m}^3$ ; Table 4). The DA  
1004 system thus overfitted the PMx concentration to approach the observed scattering coefficient.

1005 The diurnal PM<sub>10</sub> in the analysis was similar to the assimilation of PMx, showing a maximum  
1006 improvement and a robust nocturnal variation at 18:00 UTC (Figure 9c). Assimilating the  
1007 scattering coefficient failed to improve the absorption coefficient. The monthly mean  
1008 absorption coefficient was 16.5 Mm<sup>-1</sup>, 65% lower than the observed value.

1009

### 1010 3.5 Assimilating Aerosol Absorption Coefficient

1011 In contrast to the above results, assimilating the absorption coefficient (DA\_Eabs) degraded  
1012 all the analyses other than the absorption coefficient itself. The analyses showed substantial  
1013 daily variations, and strong positive biases appeared in the dust episodes (Figure 7). The  
1014 PM<sub>2.5</sub> was overestimated by a factor of three, and the PM<sub>10</sub> was overestimated by a factor of  
1015 four. The increases occurred each hour (Figure 9d). Because of the constant ratio between  
1016 mass and number concentration, the particle number concentration increased. As a result, the  
1017 aerosol scattering coefficient was overfitted to 612.2 Mm<sup>-1</sup>, higher than the observed levels by  
1018 a factor of three. The monthly mean AOD improbably rose up to 1.73. Nevertheless, the  
1019 absorption coefficient (40 Mm<sup>-1</sup>) was improved to the observed level (47.4 Mm<sup>-1</sup>).

1020

1021 Improving the absorption coefficient at the cost of PM<sub>10</sub> overestimation, indicates the model  
1022 biases in the representation of the particle mixture and the other absorbing particles (e.g.,  
1023 black carbon, brown carbon and aged dust). With respect to the current model, this failure is  
1024 related to the aerosol absorption represented in WRF-Chem. The leading absorption aerosol in  
1025 WRF-Chem is BC. The BC particle in the second size (0.156–0.625  $\mu\text{m}$ ) had the maximum  
1026 absorption, according to Mie theory, and had the maximum DA modifications in the second-  
1027 size bin (Figure 8e). However, because the BC had a small background concentration, the BC  
1028 showed a small DA improvement ( $<1.5 \mu\text{g m}^{-3}$ ) and had small effects on increasing the  
1029 particle absorption. Meanwhile, the coarse dust particle concentration was primarily  
1030 increased, but the dust particles did not have a strong absorption as BC. As a result, the model  
1031 lowered the ratio of the absorption coefficient of PM<sub>10</sub> by an order of magnitude (Table 4).

1032 The lower mass absorption efficiency was comparable at each wavelength and was close to  
1033 the other DA experiment (Figure 10c). Because of the constraint of the observed absorption  
1034 coefficient, the DA system dramatically overestimated the particle concentrations and induced

Deleted: and enlarged the diurnal variation of PM<sub>10</sub>

Deleted: The maximum increase in the mean value was at 06:00 UTC, also because of the strong noontime heating in the model. As t

Deleted: cannot increase the absorption data

Deleted: . This DA failure in assimilating the absorption coefficient

Deleted: aborting

Deleted: , but the analyzed absorption coefficient was still underestimated.

1043 too much higher aerosol scattering coefficient and AOD. Because the overestimation of the  
1044 scattering coefficient was higher than that of the absorption coefficient, DA\_abs even gave  
1045 the strongest SSArf (0.9; Table 3) in all DA experiments, opposite to our expectation that the  
1046 assimilation of absorption coefficient should improve SSA.

1047  
1048 To understand the DA\_Eabs's failure, we performed a few trials by changing the imaginary  
1049 part of the dust refractive index on 1200UTC on April 9. The results are present in the  
1050 supplementary Table S4a and S4b. The trials show that a high imaginary part of the dust  
1051 refractive index decreases the aerosol absorption coefficient. This paradox is due to the BC's  
1052 reduction. Specifically, a high imaginary part increases the absorption efficiency of coarse  
1053 dust and decreases the coarse dust number concentration (num\_a04; Table S4a). This  
1054 reduction also led to less fine aerosol number concentrations (e.g., num\_a02) because of the  
1055 inter-size bin correlation. BC is abundant in the second and third size bins, and its imaginary  
1056 part of refractive index is two orders of magnitude higher than dust. Less BC caused a weak  
1057 absorption coefficient (Table S4b). On the contrary, the low dust imaginary part would not  
1058 largely increase dust numbers in the coarse size bin because the DA system attempts to  
1059 increase BC to enhance the absorption coefficient. In an extreme case with zero value of  
1060 imaginary part of dust, the improvement of absorption coefficient exclusively relies on BC;  
1061 the num\_a02 is increased by order of magnitude (Table S4a), and 660 nm Eabs rose up to  
1062 92.5 Mm<sup>-1</sup> (Table S4b), much higher than the observed level.

1063  
1064 At Kashi, BC has a low background concentration and low background error. The innovation  
1065 of BC was limited. Thus, tuning the imaginary part of dust would not change the SSArf  
1066 value a lot (0.89 to 0.92). Excluding the contribution from OIN in PM<sub>10</sub>, the scattering  
1067 coefficient was associated with sulfate. The sulfate's background error was higher than the  
1068 BC's by order of magnitude. The DA system prioritized sulfate modification even when  
1069 assimilating absorption coefficient, resulting in a smaller BC mass fraction in PM<sub>10</sub> (Figure  
1070 12f) and a high SSArf of 0.90.

1071  
1072 We did another set of trials by increasing the original BC's BEC per size bin. As shown in the  
1073 supplementary Table S5, increasing the BC's BECs would not much degrade the absorption  
1074 coefficient but significantly decrease the positive biases in PM<sub>x</sub>, AOD, and scattering  
1075 coefficient; the SSArf approached the observation. Increasing BC's BECs by a factor of  
1076 seven (DA\_Eabs\_BC\*7) shows the best analyses. This trial suppressed the positive biases  
1077 without decreasing the accuracy of absorption coefficient (Figure 7), and the BC mass  
1078 fraction was increased (Figure 12g). Nevertheless, the disadvantage of the enlargement of  
1079 BC'BEC is that the simultaneous assimilation of scattering and absorption coefficient is not  
1080 convergent as well as before. After four outer loops and each with 50 inner iterations, the  
1081 analyzed absorption coefficient in DA\_Eabs\_BC\*7 was still higher than the observed value  
1082 by 47% (Figure S1j). It indicates there is a low bias in BC's background concentration that  
1083 violates the unbiased condition of DA.

### 1084 1085 **3.6 Assimilating Multi-source Observations**

1088 Assimilating an individual observation improves the corresponding model parameter (i.e.,  
1089 PM<sub>2.5</sub>, PM<sub>10</sub>, Esca, Eabs, and AOD) but may worsen other parameters. The reasons for the  
1090 inconsistent improvements are relevant to the aerosol model itself. These are: (1) the model  
1091 parameters have opposite signs in biases (e.g., one model parameter has a positive bias while  
1092 another has a negative bias); (2) the model biases have vast differences in magnitude (e.g., a  
1093 good fit of a parameter may lead to another's overfit) and the different biases in magnitude  
1094 cannot be reconciled because the forward operator is inaccurate to represent the linkage  
1095 between aerosol mass and aerosol optics (e.g., lower particle mass extinction efficiency).  
1096

1097 In our case, simultaneous assimilation of the scattering and absorption coefficients  
1098 (DA\_Esca\_Eabs) resulted in the analyses when assimilating the scattering coefficient alone  
1099 (DA\_Esca), and the inferior analysis in DA\_Eabs vanished. This was because incorporating  
1100 the scattering coefficient constrained the aerosol number concentrations, which also benefited  
1101 from incorporating the observed absorption coefficient. Simultaneous assimilation of PM<sub>x</sub>  
1102 and AOD (DA\_PM<sub>x</sub>\_AOD) gave the best overall DA results, in which all the analyses except  
1103 the absorption coefficient were not significantly different in the month mean values from the  
1104 observations. Furthermore, DA\_PM<sub>x</sub>\_AOD substantially improved the Ångström exponent,  
1105 with an analyzed value of 0.17, consistent with the observed value of 0.18 (Table 3).  
1106 Simultaneous assimilation of all observations (DA\_PM<sub>x</sub>\_Esca\_Eabs\_AOD) did not  
1107 substantially improve the analyses when compared with DA\_PM<sub>x</sub>\_AOD because the surface  
1108 coefficients, and AOD had overlapped information of the light attenuation. A redundant  
1109 information source did not introduce extra constraints on the DA system.   
1110

Table 3, 4; Figure 6, 7, 8, 9, 10

### 1111 1112 3.7 Vertical Profiles of Aerosol Concentrations

1113 Figure 11 shows the vertical concentration profiles of PM<sub>2.5</sub> and PM<sub>10</sub>. The DA system  
1114 increased the aerosol concentrations up to a height of 4 km, which is consistent with previous  
1115 studies on the Taklamakan Desert. Meng et al. (2019) simulated a deep dust layer thickness in  
1116 spring, with a depth of 3–5 km. Ge et al. (2014) analyzed the Cloud-Aerosol Lidar Orthogonal  
1117 Polarization data from 2006–2012 in the desert. They showed that dust could be lifted up to  
1118 5 km above the Tarim Basin, and even higher along the northern slope of the Tibetan Plateau.  
1119 Among our DA experiments, the analyzed PM<sub>x</sub> in the lower atmosphere followed PM<sub>x</sub> at the  
1120 surface. The vertical PM<sub>10</sub> concentration increased quickly in the lowest three model layers  
1121 and maintained high values at heights of less than 3 km. This vertical profile corresponded to  
1122 the background vertical error profile, reflecting the deep dust transporting layer. The PM<sub>2.5</sub>  
1123 vertical profiles showed a rapid reduction with an increase in altitude. The figure clearly  
1124 shows that DA\_PM<sub>x</sub> improved the PM<sub>2.5</sub> and PM<sub>10</sub> better, whereas DA\_AOD preferentially  
1125 adjusted the coarse particles and overestimated the PM<sub>10</sub>. Also shown in the figure are the  
1126 vertical profiles normalized to their own respective surface particulate concentrations. The  
1127 assimilations not only added a larger fraction of the mass in these layers but also adjusted the  
1128 shapes of the PM<sub>10</sub> profiles within 3 km above the ground (Figure 11d), following the BEC's  
1129 vertical correlation length scales (Figure 3r).  
1130

**Deleted:** through the adjoint operator

**Deleted:** Therefore, it may not always lead to a better analysis when assimilating one type of observation. Simultaneous assimilation of the multi-source observations imposes more definite constraints on the DA system and helps to eliminate significant model biases.

**Deleted:** Compared with the analysis assimilating the PM<sub>x</sub> alone (DA\_PM<sub>x</sub>), assimilating the two aerosol attenuation coefficients (DA\_Esca\_Eabs) better reproduced the AOD, but overestimated the surface particle concentrations. In Figures 8–9, there were extremely high values on 28 April 2019, because the scattering coefficient was missing at that time, during which the DA system assimilated the absorption coefficient alone and worsened the analysis again. Simultaneous assimilation of the surface particle concentration and the two aerosol attenuation coefficients (DA\_PM<sub>x</sub>\_Esca\_Eabs) improved these three assimilated parameters, but still gave a notable low bias in AOD, % lower than the observed levels.

**Deleted:** The analyses between DA\_PM<sub>x</sub>\_AOD and DA\_PM<sub>x</sub>\_Esca\_Eabs were comparable, except that the former additionally increased AOD better.

**Deleted:** the DA experiments failed to improve the aerosol absorption coefficient, always showed strong low biases and (), implying room for improvement of our DA system.

**Deleted:** DA\_PM<sub>x</sub>\_AOD provided the best balance between the adjustments of PM<sub>2.5</sub> and PM<sub>10</sub>.

**Deleted:** ¶

Figure 11

1159  
1160  
1161  
1162  
1163  
1164  
1165  
1166  
1167  
1168  
1169  
1170  
1171  
1172  
1173  
1174  
1175  
1176  
1177  
1178

#### 4. Discussions

##### 4.1 DA Impact on Aerosol Chemical Composition

For control variable design, our DA system modifies the chemical composition of each aerosol according to the BEC values. The  $PM_{10}$  chemical fractions remain close to their background values (Figure 12). As discussed in section 3.5, the assimilation of the aerosol absorption coefficient alone (DA\_Eabs) increased the sulfate fraction. The DA modification increased aerosol number concentration, and the rising number concentration increased the tangent linear operator value for the scattering component. Sulfate was the predominant anthropogenic aerosol at Kashi and had a high background error value. The DA system prioritized the modification of sulfate and prevented a rise in the BC fraction in DA\_Eabs. As the enlarged BC BEC in DA\_Eabs, BC\*7, the BC mass fraction showed the largest increase. The model bias in aerosol background concentration and the background error determine the analyzed aerosol chemical fraction. Overall, it seems that differences in aerosol chemical composition from assimilating the aerosol optical data are smaller than the difference in model setting (e.g., using other aerosol chemistry mechanisms, or using finer aerosol size bins). The assimilation of the total aerosol quantities cannot eliminate the intrinsic bias in aerosol composition. Thus, accurate aerosol chemistry and optical modules are crucial to attain a better background aerosol chemical data for DA analysis (Saide et al., 2020).

Figure 12

1179  
1180  
1181  
1182  
1183  
1184  
1185  
1186  
1187  
1188  
1189  
1190  
1191  
1192  
1193  
1194  
1195  
1196  
1197  
1198  
1199

##### 4.2 DA Impact on Aerosol Direct Radiative Forcing

Table 5 shows the instantaneous clear-sky ADRF in the background data and the analyses of DA\_PMx and DA\_PMx\_AOD. After the analyses, the DA effect (various DA frequencies for assimilating AOD and the surface particle concentrations) gradually faded away after restarting the model run. We therefore focused on the instantaneous radiative forcing values one hour after assimilating AOD data. This ensured that the comparison was based on similar analysis times and showed effective DA effects.

Aerosol redistributes the energy between the land and the atmosphere. The atmosphere gains more shortwave energy as the dust and black carbon particle absorption; the warming atmosphere also emits more longwave energy as it absorbs shortwave energy. The change in energy budget at the surface is correspondingly the opposite of that in the atmosphere. As shown in Table 5, the enhancements in surface cooling forces were slightly stronger than the atmospheric warming forcings. The differences between the surface forcing and atmospheric forcing indicate the ADRF at the top of the atmosphere (TOA). The TOA ADRF when assimilating the surface particle concentrations was enhanced by 21% in the shortwave, 100% in the longwave, and 18% in the net forcing values, and enhanced by 34%, 67%, and 32%, respectively, when assimilating the AOD. Apparently, assimilating PMx alone is not sufficient to accurately estimate the ADRF value. At Kashi, the total net (shortwave plus longwave) clear-sky ADRF with assimilating surface particles and AOD were  $-10.4 \text{ Wm}^{-2}$  at

**Deleted:** The maximum concentrations of sulfate, ammonium, BC, and OC in April were 4.1, 1.5, 0.5, and  $1.3 \mu\text{g m}^{-3}$ , respectively, in the background model data. Although a careful evaluation is difficult because of the lack of aerosol chemical measurements, we speculated that the aerosols (other than OIN) were considerably low. Anthropogenic emissions might be biased for this city. The sources of emissions in residential/developing areas are principally anthropogenic; yet the residential emission factor for the emission inventory compilation is highly uncertain compared with the emission factors of power plants, industrial plants, and vehicles (Li et al., 2017). Chlorine and sodium are selected to represent sea-salt aerosols in WRF-Chem, yet the two concentrations were at very low concentrations in the model at Kashi. This was despite the fact that the Taklamakan Desert had many atmospheric halite particles, which were Cl- and Na-rich and accounted for 10% of the total particles in the desert (Okada and Kai, 2004).

**Deleted:** If the DA experiments showed that the

**Deleted:** The low biases cannot be improved via DA because the aerosol chemical measurements were not available. In addition, the differences between DA\_Esca and DA\_Esca\_Eabs were quite small (Figure 13c, e), indicating that assimilating the aerosol absorption coefficient did not enhance particle absorption ( $19.1^{-1}$  vs.  $20.0 \text{ Mm}^{-1}$  in Table 3) in our system. T

**Deleted:** of BC to 7.1%, which was slightly higher than the 6.5% background BC

**Deleted:** The first reason for the small changes in the aerosol chemical proportions is that the scattering aerosols (i.e., sulfate, nitrate, and ammonium), use the same refractive index and hygroscopicity parameter in WRF-Chem. Therefore, the AOD had virtually the same sensitivity to composition of each aerosol, and assigned comparable modification to each composition. When assimilating the total quantities of aerosols (e.g.,  $PM_{2.5}$ ,  $PM_{10}$ , and AOD), it is difficult to distinguish different aerosol chemical ... [1]

**Deleted:** As the dust was the predominant component, the ADRF in this section was closely equivalent to the dust radiative forcing.

**Deleted:** Dust

1259 the TOA,  $+20.8 \text{ Wm}^{-2}$  within the atmosphere, and  $-31.2 \text{ Wm}^{-2}$  at the surface, respectively,  
1260 enhanced by 55%, 48%, and 50% respectively, compared to the background ADRF values.

1261  
1262 It is noteworthy to say that the ADRF estimation remains uncertain even after DA. The AOD  
1263 observation is only sporadically available because of cloud screening in retrieval data. The  
1264 DA experiments cannot eliminate the low bias in AOD in WRF-Chem. The ADRF values in  
1265 the DA experiments are likely to be weaker than the plausible aerosol radiative forcing at  
1266 Kashi. Neither DA experiment lowers SSAsrf to approach the observation. The observed  
1267 SSAsrf (0.78) indicates likely warming forcing of aerosol at Kashi, while WRF-Chem and the  
1268 DA analyses impose cooling forcing. The ADRF uncertainty is associated with the  
1269 background aerosols. WRF-Chem simulates aerosol size up to 10  $\mu\text{m}$ , whereas larger particles  
1270 (>10  $\mu\text{m}$ ) exhibit substantial absorption relative to scattering in the visible wavelength (Kok  
1271 et al., 2017). Anthropogenic emission inventories need an update for the year 2019, which  
1272 may reduce the potential low bias in BC concentration. Additionally, the revised GSI does not  
1273 concern the change in particle effective radius per size bin when calculating the aerosol  
1274 number concentration in each outer loop. Low absorption cross section rises aerosol number  
1275 concentration as compensation, increasing aerosol scattering coefficient too much. If our  
1276 tangent operator concerns the change in particle effective radius per size bin, we can use  
1277 aerosol mass and number concentration as control variables simultaneously. The DA would  
1278 have a higher degree of freedom to balance the particle radius and number concentration and  
1279 improve the absorption coefficient. All these need further research in the future.

1280

## 1281 5. Conclusions

1282 This study described our revised GSI DA system for assimilating aerosol observed data for  
1283 the four-size bin sectional MOSAIC aerosol mechanism in WRF-Chem. The DA system has  
1284 new design tangent linear operators for the multi-wavelength AOD, aerosol scattering, and  
1285 absorption coefficients measured by the sun-sky radiometer, nephelometer, and aethalometer,  
1286 respectively. We examined the DA system for Kashi city in northwestern China by  
1287 assimilating the multi-wavelength aerosol optical measurements gathered by the Dust Aerosol  
1288 Observation–Kashi field campaign of April 2019 and the concurrent hourly measurements of  
1289 surface  $\text{PM}_{2.5}$  and  $\text{PM}_{10}$  concentrations.

1290

1291 Our DA system includes two main aspects. Firstly, the control variable is the aerosol chemical  
1292 composition per size bin corresponding to the WRF-Chem output data. This design allows the  
1293 modification of the composition of each aerosol, based on their background error covariances.  
1294 The number of control variables could be reduced by intentionally excluding a few aerosol  
1295 compositions in a specific case, if these compositions had low concentrations (e.g. chlorine  
1296 and sodium in this study). Second, the DA system incorporates the observed AOD by  
1297 assimilating the column mean aerosol extinction coefficient. This transfer avoids handling  
1298 sensitivity from light attenuation length to the aerosol mass concentration in the tangent linear  
1299 operator, which is difficult to accurately estimate and introduces significant errors in the  
1300 operator. The tangent linear operator for AOD has two variants that can incorporate  
1301 nephelometer and aethalometer measurements at the surface.

1302

Deleted: adjoint

Deleted: adjoint

Deleted: adjoint

1306 The most abundant aerosol at Kashi in April 2019 was dust. The WRF-Chem model captured  
1307 the main dust episodes, but lowered the monthly mean concentrations of PM<sub>2.5</sub> and PM<sub>10</sub> by  
1308 17% and 41%, respectively. The model failed to capture the peak concentrations from a dust  
1309 storm on 24 April. The aerosol scattering/absorption coefficients and AOD in the background  
1310 data showed strong low biases and weak correlations with the observed levels. The DA  
1311 systems effectively assimilate the surface particle concentrations, aerosol scattering  
1312 coefficients, and AOD. Some deficiencies in the DA analysis were related to the forward  
1313 model bias in transferring the aerosol mass concentrations to the aerosol optical parameter.  
1314 Simultaneous assimilation of the PM<sub>2.5</sub> and PM<sub>10</sub> concentrations improved the model aerosol  
1315 concentrations, with significant increases in the coarse particles; meanwhile, the analyzed  
1316 AOD was 42% lower than observed levels. The assimilation of AOD significantly improved  
1317 the AOD but overestimated the surface PM<sub>10</sub> concentration by 68%. Assimilating the aerosol  
1318 scattering coefficient improved the scattering coefficient in the analysis but overestimated the  
1319 surface PM<sub>10</sub> concentration by 37%. It therefore seems that WRF-Chem underestimated the  
1320 particle extinction efficiency. As a compensation, the DA system overestimated the aerosol  
1321 concentration to fit the observed optical values, yielding overly high particle concentrations.  
1322

1323 A notable problem was the assimilation of the absorption coefficient, which greatly  
1324 overestimated the monthly mean values by a factor of four in PM<sub>10</sub>. The aerosol absorption  
1325 coefficient was improved but was still 16% lower than observed values. The failure of DA  
1326 analysis when assimilating the absorption coefficient is associated with many factors,  
1327 including the biases of the model in aerosol particle mixture and aged dust, the uncertainties  
1328 in the imaginary part of dust refractive index, the uncertain background error of BC and the  
1329 likely low bias in anthropogenic emissions. The most effective DA is the simultaneous  
1330 assimilation of surface particle concentration and AOD, which provides the best overall DA  
1331 analysis.  
1332

1333 Our design of control variables allowed the DA system to adjust the aerosol chemical  
1334 compositions individually. However, the analyzed anthropogenic aerosol chemical fractions  
1335 were almost equivalent to the background chemical fractions. The reason is that the  
1336 hydrophilic aerosols have equivalent or comparable refractive indices and hygroscopic  
1337 parameters in the forward operator; they therefore have comparable adjoint operator values  
1338 when assimilating the aerosol optical data. It may be possible to separate the chemical  
1339 compositions based on their background errors. The model anthropogenic aerosols were low  
1340 at Kashi, probably owing to the low biases in the anthropogenic emissions. The low  
1341 background concentrations led to low background errors and hence few increments for all  
1342 chemical compositions. As a result, the chemical fractions of the anthropogenic aerosols  
1343 remained close to their background values.  
1344

1345 When assimilating surface particles and AOD, the instantaneous clear-sky ADRF (shortwave  
1346 plus longwave) at Kashi were -10.4 Wm<sup>-2</sup> at the TOA, +20.8 Wm<sup>-2</sup> within the atmosphere,  
1347 and -31.2 Wm<sup>-2</sup> at the surface, respectively. Since the DA analyses still lowered the AOD  
1348 value and overestimated SSA, the aerosol radiative forcing values assimilating the  
1349 observations were underestimated in the atmosphere and at the surface.

**Deleted:** The biases of the model in aerosol particle mixture and aged dusts as well as the “missing” absorption of brown carbon, accounted for the bias in absorption efficiency, which would have worsened the DA analysis when assimilating the absorption coefficient.¶

¶ Simultaneous assimilation of the multi-source observations imposes a more definite constraint and helps improve model parameters. Simultaneously assimilating the scattering and absorption coefficients eliminated the defect of assimilating the absorption coefficient. It also provided comparable improvements for assimilating the surface particles and AOD; the latter additionally improved the AOD analysis.

1363

1364 The limitations that necessitate further research include:

1365 (1) The desired [binning](#) strategy should link the circulation flow and particle emission  
1366 sources. A better hybrid DA coupled with the ensemble Kalman filter will be more effective  
1367 for estimating the aerosol background error.

1368 (2) The observational error could be elaborated further. The PM<sub>10</sub> included the  
1369 anthropogenic coarse particles, which should be separated from the dust originating from the  
1370 desert (Jin et al., 2019). We set the observation errors for PM<sub>x</sub> and AOD to the conventional  
1371 values. The observational errors of the nephelometer and aethalometer were slightly arbitrary  
1372 in this study, necessitating further consideration.

1373 (3) The [anthropogenic aerosols' background errors are needed to harmonize for better](#)  
1374 [assimilation of](#) the aerosol absorption coefficient or absorption AOD.

1375 (4) The DA system was based on four-size bin MOSAIC aerosols, but it can be extended  
1376 to work with eight-size bin MOSAIC aerosols in WRF-Chem. When assimilating aerosol  
1377 optical data, the DA quality is strongly dependent on the forward model. The responses of our  
1378 DA analysis to the bias and uncertainty in the forward aerosol optical model in WRF-Chem  
1379 need further investigation.

1380

#### 1381 **Author contributions**

1382 WC developed the DA system, performed the analyses and wrote the paper. ZL led the field  
1383 campaign and revised the paper. YZ and KL implemented the observations and the data  
1384 quality control. YZ helped to design the new adjoint operator. JC verified the DA system.

1385

#### 1386 **Competing interests**

1387 The authors declare that they have no conflict of interest.

1388

#### 1389 **Code/Data availability**

1390 The official GSI code is available at [https://dtcenter.org/community-code/gridpoint-statistical-](https://dtcenter.org/community-code/gridpoint-statistical-interpolation-gsi/download)  
1391 [interpolation-gsi/download](https://dtcenter.org/community-code/gridpoint-statistical-interpolation-gsi/download). [The revised GSI code is available at https://github.com/wenyuan-](https://github.com/wenyuan-chang/GSI_WRF-Chem_MOSAIC)  
1392 [chang/GSI\\_WRF-Chem\\_MOSAIC](https://github.com/wenyuan-chang/GSI_WRF-Chem_MOSAIC). The aerosol measurements at Kashi belong to the Sun-sky  
1393 radiometer Observation NETwork (SONET) which is accessible at  
1394 <http://www.sonet.ac.cn/en/index.php>.

1395

#### 1396 **Acknowledgments**

1397 This work is supported by the National Key Research and Development Program of China  
1398 (Grant number 2016YFE0201400).

1399

#### 1400 **References**

1401 [Adebisi, A. A., Kok, J. F.: Climate models miss most of the coarse dust in the atmosphere,](#)  
1402 [Sci. Adv., 6, 1-10, doi:10.1126/sciadv.aaz9507, 2020.](#)

1403

1404 Bannister, R. N.: A review of operational methods of variational and ensemble-variational  
1405 data assimilation, Q.J.R. Meteorol. Soc., 143, 607-633, doi:10.1002/qj.2982, 2017.

1406

1407 Bao, Y., Zhu, L., Guan, Q., Guan, Y., Lu, Q., Petropoulos, G. P., Che H., Ali, g., Dong, Y.,  
1408 Tang, Z., Gu, Y., Tang, W., and Hou, Y.: Assessing the impact of Chinese FY-3/MERSI  
1409 AOD data assimilation on air quality forecasts: sand dust events in northeast China, *Atmos.*  
1410 *Environ.*, 205, 78-89, doi:10.1016/j.atmosenv.2019.02.026, 2019.

1411 [Barnard, J. C., Fast, J. D., Paredes-Miranda, G., Arnott, W. P., and Laskin, A.: Technical](#)  
1412 [Note: Evaluation of the WRF-Chem “Aerosol Chemical to Aerosol Optical Properties”](#)  
1413 [Module using data from the MILAGRO campaign, \*Atmos. Chem. Phys.\*, 19, 7325-7340,](#)  
1414 [doi:10.5194/acp-10-7325-2010, 2010.](#)

1415 [Bond, T. C., and Bergstrom, R. W.: Light absorption by carbonaceous particles: an](#)  
1416 [investigative review, \*Aerosol Sci. Tech.\*, 40, 27-67, doi:10.1080/02786820500421521, 2006.](#)

1417 Calil, P. H. R., Doney, S. C., Yumimoto, K., Eguchi, K., and Takemura, T.: Episodic  
1418 upwelling and dust deposition as bloom triggers in low-nutrient, low-chlorophyll regions, *J.*  
1419 *Geophys. Res.*, 116, C06030, doi:10.1029/2010jc006704, 2011.

1420 [Chen, Y., and Bond, T. C.: Light absorption by organic carbon from wood combustion,](#)  
1421 [Atmos. Chem. Phys., 10, 1773-1787, doi:10.5194/acp-10-1773-2010, 2010.](#)

1422 Chen, D., Liu, Z., Schwartz, C. S., Lin, H.-C., Cetola, J. D., Gu, Y., and Xue, L.: The impact  
1423 of aerosol optical depth assimilation on aerosol forecasts and radiative effects during a wild  
1424 fire event over the United States, *Geosci. Model Dev.*, 7, 2709-2715, doi:10.5194/gmd-7-  
1425 2709-2014, 2014.

1426 Chen, L., Gao, Y., Zhang, M., Fu, J. S., Zhu, J., Liao, H., Li, J., Huang, K., Ge, B., Wang, X.,  
1427 Lam, Y. F., Lin, C.-Y., Itahashi, S., Nagashima, T., Kajino, M., Yamaji, K., Wang, Z., and  
1428 Kurokawa, J.-i.: MICS-Asia III: multi-model comparison and evaluation of aerosol over East  
1429 Asia, *Atmos. Chem. Phys.*, 19, 11911-11937, doi:10.5194/acp-19-11911-2019, 2019.

1430 Chen, S.-H., and Sun, W.-Y.: A one-dimensional time dependent cloud model, *J. Meteor. Soc.*  
1431 *Japan*, 80, 1, 99-118, doi:10.2151/jmsj.80.99, 2002.

1432 [Chen, D., Liu, Z., Ban, J., Zhao, P., and Chen, M.: Retrospective analysis of 2015-2017](#)  
1433 [wintertime PM<sub>2.5</sub> in China: response to emission regulations and the role of meteorology,](#)  
1434 [Atmos. Chem. Phys., 19, 7409-7427, doi:10.5194/acp-19-7409-2019, 2019.](#)

1435 [Cheng, T., Wang, H., Xu, Y., Li, H., and Tian, L.: Climatology of aerosol optical properties in](#)  
1436 [northern China, \*Atmos. Environ.\*, 40, 1495-1509, doi:10.1016/j.atmosenv.2005.10.047, 2006.](#)

1437 Cheng, X., Liu, Y., Xu, X., You, W., Zang, Z., Gao, L., Chen, Y., Su, D., and Yan, P.: Lidar  
1438 data assimilation method based on CRTM and WRF-Chem models and its application in  
1439 PM<sub>2.5</sub> forecasts in Beijing, *Sci. Total Environ.*, 682, 541-552,  
1440 doi:10.1016/j.scitotenv.2019.05.186, 2019.

1451  
1452 Descombes, G., Auligné, T., Vandenberghe, F., Barker, D. M., and Barré, J.: Generalized  
1453 background error covariance matrix model (GEN\_BE v2.0), *Geosci. Model Dev.*, 8, 669-696,  
1454 doi:10.5194/gdm-8-669-2015, 2015.  
1455  
1456 [Di Biagio, C., Formenti, P., Balkanski, Y., Caponi, L., Cazaunau, M., Pangui, E., Journet, E.,](#)  
1457 [Nowak, S., Andreae, M. O., Kandler, K., Saeed, T., Piketh, S., Seibert, D., Williams, E., and](#)  
1458 [Doussin, J.-F.: Complex refractive indices and single-scattering albedo of global dust aerosols](#)  
1459 [in the shortwave spectrum and relationship to size and iron content, \*Atmos. Chem. Phys.\*, 19,](#)  
1460 [15503-15531, doi:10.5194/acp-19-15503-2019, 2019.](#)  
1461  
1462 [Dubovik, O., Sinyuk, A., Lapyonok, T., Holben, B. N., Mishchenko, M., Yang, P., Eck, T. F.,](#)  
1463 [Volten, H., Muñoz, O., Veihelmann, B., van der Zande, W. J., Leon, J.-F., Sorokin, M., and](#)  
1464 [Slutsker, I.: Application of spheroid models to account for aerosol particle nonsphericity in](#)  
1465 [remote sensing of desert dust, \*J. Geophys. Res.\*, 111, doi:10.1029/2005JD006619, 2006.](#)  
1466  
1467 Fan, J., Shang, Y., Chen, Q., Wang, S., Zhang, X., Zhang, L., Zhang, Y., Xu, X., and Jiang,  
1468 P.: Investigation of the “dust reservoir effect” of the Tarim Basin using WRF-GOCART  
1469 model, *Arab. J. Geosci.*, 13, 214, doi:10.1007/s12517-020-5154-x, 2020.  
1470  
1471 Fast, J. D., Gustafson, W. I., Easter, R. C., Zaveri, R. A., Barnard, J. C., Chapman, E. G.,  
1472 Grell, G. A. Peckham, S. E.: Evolution of ozone, particulates, and aerosol direct radiative  
1473 forcing in the vicinity of Houston using a fully coupled meteorology-chemistry-aerosol  
1474 model, *J. Geophys. Res.-Atmos.*, 111, D21305, doi:10.1029/2005jd006721, 2006.  
1475  
1476 Feng, S., Jiang, F., Jiang, Z., Wang, H., Cai, Z., and Zhang, L.: Impact of 3DVAR  
1477 assimilation of surface PM<sub>2.5</sub> observations on PM<sub>2.5</sub> forecasts over China during wintertime,  
1478 *Atmos. Environ.*, 187, 34-49, doi:10.1016/j.atmosenv.2018.05.049, 2018.  
1479  
1480 Ge, J. M., Huang, J. P., Xu, C. P., Qi, Y. L., and Liu, H. Y.: Characteristics of Taklimakan  
1481 dust emission and distribution: A satellite and reanalysis field perspective, *J. Geophys. Res.*  
1482 *Atmos.*, 119, 11772-11783, doi:10.1002/2014jd022280, 2014.  
1483  
1484 Ge, J. M., Liu, H., Huang, J., and Fu, Q.: Taklimakan desert nocturnal low-level jet:  
1485 climatology and dust activity, *Atmos. Chem. Phys.*, 16, 7773-7783, doi:10.5194/acp-16-7773-  
1486 2016, 2016.  
1487  
1488 Ginoux, P., Chin, M., Tegen, I., Prospero, J. M., Holben, B., Dubovik, O., and Lin, S.-J.:  
1489 Sources and distributions of dust aerosols simulated with the GOCART model, *J. Geophys.*  
1490 *Res.*, 106, D17, 20255-20273, doi: 10.1029/2000JD000053, 2001.  
1491  
1492 Giorgi, F., and Mearns, L. O.: Introduction to special section: Regional climate modeling  
1493 revisited, *J. Geophys. Res.*, 104, D6, 6335-6352, doi:10.1029/98JD02072, 1999.  
1494

1495 Grell, G. A., Peckham, S. E., Schmitz, R., McKeen, S. A., Frost, G., Skamarock, W. C., and  
1496 Eder, B.: Fully coupled “online” chemistry within the WRF model. *Atmos. Environ.*, 39,  
1497 6957-7975, doi:10.1016/j.atmosenv.2005.04.027, 2005.  
1498  
1499 Guenther, A., Karl, T., Harley, P., Wiedinmyer, C., Palmer, P. I., and Geron, C.: Estimates of  
1500 global terrestrial isoprene emissions using MEGAN (Model of Emissions of Gases and  
1501 Aerosols from Nature), *Atmos. Chem. Phys.*, 6, 3181-3210, doi:10.5194/acp-6-3181-2006,  
1502 2006.  
1503  
1504 He, J., Zhang, Y., Wang, K., Chen, Y., Leung, L. R., Fan, J., Li, M., Zheng, B., Zhang, Q.,  
1505 Duan, F., and He, K.: Multi-year application of WRF-CAM5 over East Asia-Part I:  
1506 Comprehensive evaluation and formation regimes of O<sub>3</sub> and PM<sub>2.5</sub>, *Atmos. Environ.*, 165,  
1507 122-142, doi:10.1016/j.atmosenv.2017.06.015, 2017.  
1508  
1509 [Holben, B. N., Eck, T. F., Slutsker, I., Tanré D., Buis, J. P., Setzer, A., Vermote, E., Reagan,  
1510 J. A., Kaufman, Y. J., Nakajima, T., Lavenu, F., Jankowiak, I., and Smirnov, A.: AERONET—  
1511 A federated instrument network and data archive for aerosol characterization, \*Remote Sens.\*  
1512 \*Environ.\*, 66, 1-16, doi:10.1016/s0034-4257\(98\)00031-5, 1998.](#)  
1513  
1514 Hong, S.-Y., Noh, Y., Dudhia, J.: A new vertical diffusion package with an explicit treatment  
1515 of entrainment processes, *Mon. Wea. Res.*, 134, 2318-2341, doi:10.1175/MWR3199.1, 2006.  
1516  
1517 Huang, J., Wang, T., Wang, W., Li, Z., and Yan, H.: Climate effects of dust aerosols over  
1518 East Asian arid and semiarid regions, *J. Geophys. Res.*, 119, 11398-11416,  
1519 doi:10.1002/2014jd021796, 2014.  
1520  
1521 Hong, J., Mao, F., Min, Q., Pan, Z., Wang, W., Zhang, T., and Gong, W.: Improved PM<sub>2.5</sub>  
1522 predictions of WRF-Chem via the integration of Himawari-8 satellite data and ground  
1523 observations, *Environ. Pollut.*, 263, 114451, doi:10.1016/j.envpol.2020.114451, 2020.  
1524  
1525 Iacono, M. J., Delamere, J. S., Mlawer, E. J., Shephard, M. W., Clough, S. A., and Collins,  
1526 W. D.: Radiative forcing by long-lived greenhouse gases: Calculations with the AER radiative  
1527 transfer models, *J. Geophys. Res.*, 113, D13103, doi:10.1029/2008JD009944, 2008.  
1528  
1529 Jia, R., Liu, Y., Chen, B., Zhang, Z., and Huang, J.: Source and transportation of summer dust  
1530 over the Tibetan Plateau, *Atmos. Environ.*, 123, 210-219,  
1531 doi:10.1016/j.atmosenv.2015.10.038, 2015.  
1532  
1533 Jiang, Z., Liu, Z., Wang, T., Schwartz, C. S., Lin, H.-C., and Jiang, F.: Probing into the  
1534 impact of 3DVAR assimilation of surface PM<sub>10</sub> observations over China using process  
1535 analysis, *J. Geophys. Res.*, 118, 6738-6749, doi:10.1002/jgrd.50495, 2013.  
1536

1537 Jin, J., Lin, H. X., Segers, A., Xie, Y., and Heemink, A.: Machine learning for observation  
1538 bias correction with application to dust storm data assimilation, *Atmos. Chem. Phys.*, 19,  
1539 10009-10026, doi:10.5194/acp-19-10009-2019.

1540  
1541 [Kok, J. F.: A scaling theory for the size distribution of emitted dust aerosols suggests climate](#)  
1542 [models underestimate the size of the global dust cycle, \*Proc. Natl. Acad. Sci. U.S.A.\*, 108,](#)  
1543 [1016-1021, doi:10.1073/pnas.1014798108, 2011.](#)

1544  
1545 [Kok, J. F., Ridley, D. A., Zhou, Q., Miller, R. L., Zhao, C., Heald, C. L., Ward, D. S., Albani,](#)  
1546 [S., and Haustein, K.: Smaller desert dust cooling effect estimated from analysis of dust size](#)  
1547 [and abundance, \*Nat. Geosci.\*, doi:10.1038/ngeo2912, 2017.](#)

1548  
1549 [Kumar, R., Monache, L. D., Bresch, J., Saide, P. E., Tang, Y., Liu, Z., de Silva, A. M.,](#)  
1550 [Alessandrini, S., Pfister, G., Edwards, D., Lee, P., and Djalaova, I.: Toward improving short-](#)  
1551 [term predictions of fine particulate matter over the United States via assimilation of satellite](#)  
1552 [aerosol optical depth retrievals, \*J. Geophys. Res.\*, 124, 2753-2773,](#)  
1553 [doi:10.1029/2018jd029009, 2019.](#)

1554  
1555 Li, L., Li, Z., Chang, W., Ou, Y., Goloub, P., Li, C., Li, K., Hu, Q., Wang, J., and Wendisch,  
1556 M.: Solar radiative forcing of aerosol particles near the Taklimakan desert during the Dust  
1557 Aerosol Observation-Kashi campaign in Spring 2019, *Atmos. Chem. Phys.*, 20, 10845-10864,  
1558 doi:10.5194/acp-2020-60, 2020.

1559  
1560 Li, M., Liu, H., Geng, G., Hong, C., Liu, F., Song, Y., Tong, D., Zheng, B., Cui, H., Man, H.,  
1561 Zhang, Q., and He, K.: Anthropogenic emission inventories in China: a review, *Natl. Sci.*  
1562 *Rev.*, 4, 834-866, doi:10.1093/nsr/nwx150, 2017.

1563  
1564 Li, Z., Zang, Z., Li, Q. B., Chao, Y., Chen, D., Ye, Z., Liu, Y., and Liou, K. N.: A three-  
1565 dimensional variational data assimilation system for multiple aerosol species with  
1566 WRF/Chem and an application to PM<sub>2.5</sub> prediction, *Atmos. Chem. Phys.*, 13, 4265-4278,  
1567 doi:10.5194/acp-13-4265-2013, 2013.

1568  
1569 [Li, Z. Q., Xu, H., Li, K. T., Li, D. H., Xie, Y. S., Li, L., Zhang, Y., Gu, X. F., Zhao, W., Tian,](#)  
1570 [Q. J., Deng, R. R., Su, X. L., Huang, B., Qiao, Y. L., Cui, W. Y., Hu, Y., Gong, C. L., Wang,](#)  
1571 [Y. Q., Wang, X. F., Wang, J. P., Du, W. B., Pan, Z. Q., Li, Z. Z., and Bu, D.: Comprehensive](#)  
1572 [study of optical, physical, chemical, and radiative properties of total columnar atmospheric](#)  
1573 [aerosols over China An overview of sun-sky radiometer observation network \(SONET\)](#)  
1574 [measurements, \*Bull. Amer. Meteorol. Soc.\*, 739-755, doi:10.1175/BMAS-D-17-0133.1, 2018.](#)

1575  
1576 Liu, Z., Liu, Q., Lin, H.-C., Schwartz, C. S., Lee, Y.-H., and Wang, T.: Three-dimensional  
1577 variational assimilation of MODIS aerosol optical depth: Implementation and application to a  
1578 dust storm over East Asia, *J. Geophys. Res.*, 116, D23206, doi:10.1029/2011JD016159, 2011.

1579

1580 Ma, C., Wang, T., Mizzi, A. P., Anderson, J. L., Zhuang, B., Xie, M., and Wu, R.:  
1581 Multiconstituent data assimilation with WRF-Chem/DART: Potential for adjusting  
1582 anthropogenic emissions and improving air quality forecasts over eastern China, *J. Geophys.*  
1583 *Res. Atmos.*, 124, 7393-7412, doi:10.1029/2019JD030421, 2019.  
1584  
1585 Ma, C., Wang, T., Jiang, Z., Wu, H., Zhao, M., Zhuang, B., Li, S., Xie, M., Li, M., Liu, J.,  
1586 and Wu, R.: Importance of bias correction in data assimilation of multiple observations over  
1587 eastern China using WRF-Chem/DART, *J. Geophys. Res. Atmos.*, 125, e2019JD031465,  
1588 doi:10.1029/2019JD031465, 2020.  
1589  
1590 [Malm, W., C., and Hand, J. L.: An examination of the physical and optical properties of](#)  
1591 [aerosols collected in the IMPROVE program, \*Atmos. Environ.\*, 41, 16, 3407-3427,](#)  
1592 [doi:10.1016/j.atmosenv.2006.12.012, 2007.](#)  
1593  
1594 Massart, S., Pajot, B., Piacentini, A., and Pannekoucke, O.: On the merits of using a 3D-  
1595 FGAT assimilation scheme with an outer loop for atmospheric situations governed by  
1596 transport, *Mon. Weather Rev.*, 138, 12, 4509-4522, doi:10.1175/2010MWR3237.1, 2010.  
1597  
1598 Meng, L., Yang, X., Zhao, T., He, Q., Lu, H., Mamtimin, A., Huo, W., Yang, F., and Liu, C.:  
1599 Modeling study on three-dimensional distribution of dust aerosols during a dust storm over  
1600 the Tarim Basin, Northwest China, *Atmos. Res.*, 218, 285-295,  
1601 doi:10.1016/j.atmosres.2018.12.006, 2019.  
1602  
1603 [Okada, K., Heintzenberg, J., Kai, K., and Qin, Y.: Shape of atmospheric mineral particles](#)  
1604 [collected in three Chinese arid-regions, \*Geophys. Res. Lett.\*, 28, 16, 3123-3126,](#)  
1605 [doi:10.1029/2000GL012798, 2001.](#)  
1606  
1607 Okada, K., and Kai, K.: Atmospheric mineral particles collected at Qira in the Taklamakan  
1608 Desert, China, *Atmos. Environ.*, 38, 6927-6935, doi:10.1016/j.atmosenv.2004.03.078, 2004.  
1609  
1610 Pagowski, M., Grell, G. A., McKeen, S. A., Peckham, S. E., and Devenyi, D.: Three-  
1611 dimensional variational data assimilation of ozone and fine particulate matter observations:  
1612 some results using the Weather Research and Forecasting – Chemistry model and Grid-point  
1613 Statistical Interpolation, *Q. J. R., Meteorol. Soc.*, 136, 2014-2024, doi:10.1002/qj.700, 2010.  
1614  
1615 Pagowski, M., Liu, Z., Grell, G. A., Hu, M., Lin, H.-C., and Schwartz, C. S.: Implementation  
1616 of aerosol assimilation in Gridpoint Statistical Interpolation (v.3.2) and WRF-Chem (v.3.4.1),  
1617 *Geosci. Model Dev.*, 7, 1621-1627, doi:10.5194/gmd-7-1621-2014, 2014.  
1618  
1619 Pang, J., Liu, Z., Wang, X., Bresch, J., Ban, J., Chen, D., and Kim, J.: Assimilating AOD  
1620 retrievals from GOCI and VIIRS to forecast surface PM<sub>2.5</sub> episodes over eastern China,  
1621 *Atmos. Environ.*, 179, 288-304, doi:10.1016/j.atmosenv.2018.02.011, 2018.  
1622

1623 Pang, J., Wang, X., Shao, M., Chen, W., and Chang, M.: Aerosol optical depth assimilation for  
1624 a modal aerosol model: Implementation and application in AOD forecasts over East Asia, *Sci.*  
1625 *Total Environ.*, 719, 137430, doi:10.1016/j.scitotenv.2020.137430, 2020.  
1626  
1627 Parrish, D. F., and Derber, J. C.: The National Meteorological Center's spectral statistical-  
1628 interpolation analysis system, *Mon. Weather Rev.*, 120, 1747-1763, doi: 10.1175/1520-  
1629 0493(1992)120<1747:TnMCSS>2.0.CO;2, 1992.  
1630  
1631 Peng, Z., Liu, Z., Chen, D., and Ban, J.: Improving PM<sub>2.5</sub> forecast over China by the joint  
1632 adjustment of initial conditions and source emissions with an ensemble Kalman filter, *Atmos.*  
1633 *Chem. Phys.*, 17, 4837-4855, doi:10.5194/acp-17-4837-2017, 2017.  
1634  
1635 Peng, Z., Lei, L., Liu, Z., Sun, J., Ding, A., Ban, J., Chen, D., Kou, X., and Chu, K.: The  
1636 impact of multi-species surface chemical observation assimilation on air quality forecasts in  
1637 China, *Atmos. Chem. Phys.*, 18, 17387-17404, doi:10.5194/acp-18-17387-2018, 2018.  
1638  
1639 Purser, R. J., Wu, W.-S., Parrish, D. F., and Roberts, N. M.: Numerical aspects of the  
1640 application of recursive filters to variational statistical analysis. Part I: spatially homogeneous  
1641 and isotropic gaussian covariances, *Mon. Weather Rev.*, 131, 1524-1535, doi: 10.1175//1520-  
1642 0493(2003)131<1524:NAOTAO>2.0.CO;2, 2003a.  
1643  
1644 Purser, R. J., Wu, W.-S., Parrish, D. F., and Roberts, N. M.: Numerical aspects of the  
1645 application of recursive filters to variational statistical analysis. Part II: spatially  
1646 inhomogeneous and anisotropic general covariances, *Mon. Weather Rev.*, 131, 1536-1548,  
1647 doi: 10.1175//2543.1, 2003b.  
1648  
1649 Saide, P. E., Carmichael, G. R., Liu, Z., Schwartz, C. S., Lin, H. C., da Silva, A. M., and  
1650 Hyer, E.: Aerosol optical depth assimilation for a size-resolved sectional model: impacts of  
1651 observationally constrained, multi-wavelength and fine mode retrievals on regional scale  
1652 analyses and forecasts, *Atmos. Chem. Phys.*, 13, 10425-10444, doi:10.5194/acp-13-10425-  
1653 2013, 2013.  
1654  
1655 Saide, P. E., Kim, J., Song, C. H., Choi, M., Cheng, Y., and Carmichael, G. R.: Assimilation  
1656 of next generation geostationary aerosol optical depth retrievals to improve air quality  
1657 simulations, *Geophys. Res. Lett.*, 41, 9188-9196, doi:10.1002/2014GL062089, 2014.  
1658  
1659 Saide, P. E., Gao, M., Lu, Z., Goldberg, D., Streets, D. G., Woo, J.-H., Beyersdorf, A., Corr,  
1660 C. A., Thornhill, K. L., Anderson, B., Hair, J. W., Nehr, A. R., Diskin, G. S., Jimenez, J. L.,  
1661 Nault, B. A., Campuzano-Jost, P., Dibb, J., Heim, E., Lamb, K. D., Schwarz, J. P., Perring,  
1662 A. E., Kim, J., Choi, M., Holben, B., Pfister, G., Hodzic, A., Carmichael, G. R., Emmons, L.,  
1663 and Crawford, J. H.: Understanding and improving model representation of aerosol optical  
1664 properties for a Chinese haze event measured during KORUS-AQ, *Atmos. Chem. Phys.*, 20,  
1665 6455-6478, doi:10.5194/acp-20-6455-2020, 2020.  
1666

1667 Schwartz, C. S., Liu, Z., Lin, H.-C., and McKeen, S. A.: Simultaneous three-dimensional  
1668 variational assimilation of surface fine particulate pattern and MODIS aerosol optical depth, *J.*  
1669 *Geophys. Res.*, 117, D13202, doi:10.1029/2011JD017383, 2012.

1670  
1671 Sič, B., Amraoui, L. E., Piacentini, A., Marécal, V., Emili, E., Cariolle, D., Prather, M., and  
1672 Attié, J.-L.: Aerosol data assimilation in the chemical transport model MOCAGE during the  
1673 TRAQA/ChArMEx campaign: aerosol optical depth, *Atmos. Chem. Phys.*, 9, 5535-5554,  
1674 doi:10.5194/amt-9-5535-2016, 2016.

1675  
1676 [Sorribas, M., Olmo, F. J., Quirantes, A., Lyamani, H., Gil-Ojeda, M., Alados-Arboledas, L.,](#)  
1677 [and Horvath, H.: Role of spheroidal particles in closure studies for aerosol microphysical-](#)  
1678 [optical properties, \*Q. J. R. Meteorol. Soc.\*, 141, 2700-2707, doi:10.1002/qj.2557, 2015.](#)

1679  
1680 Tang, Y., Pagowski, M., Chai, T., Pan, L., Lee, P., Baker, B., Kumar, R., Monache, L. D.,  
1681 Tong, D., and Kim, H.-C.: A case study of aerosol data assimilation with the Community  
1682 Multi-scale Air Quality Model over the contiguous United States using 3D-Var and optimal  
1683 interpolation methods, *Geosci. Model Dev.*, 10, 4743-4758, doi:10.5194/gmd-10-4743-2017,  
1684 2017.

1685  
1686 Tewari, M., Chen, F., Wang, W., Dudhai, J., LeMone, M. A., Mitchell, K., Ek, M., Gayno,  
1687 G., Wegiel, J., and Cuenca, R. H.: Implementation and verification of the unified NOAA land  
1688 surface model in the WRF model. 20<sup>th</sup> conference on weather analysis and forecasting/16<sup>th</sup>  
1689 conference on numerical weather prediction, pp. 11-15, 2004.

1690  
1691 [Tian, Y., Wang, Z., Pan, X., Li, J., Yang, T., Wang, D., Liu, X., Liu, H., Zhang, Y., Lei, S.,](#)  
1692 [Sun, Y., Fu, P., Uno, I., and Wang, Z.: Influence of the morphological change in natural](#)  
1693 [Asian dust during transport: A modeling study for a typical dust event over northern China,](#)  
1694 [\*Sci. Total Environ.\*, 10.1016/j.scitotenv.2020.139791, 2020.](#)

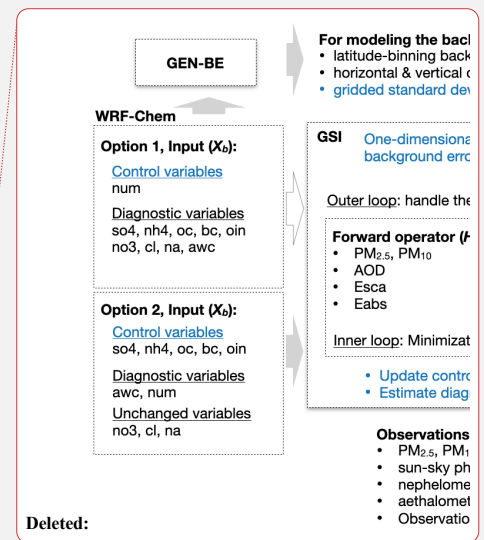
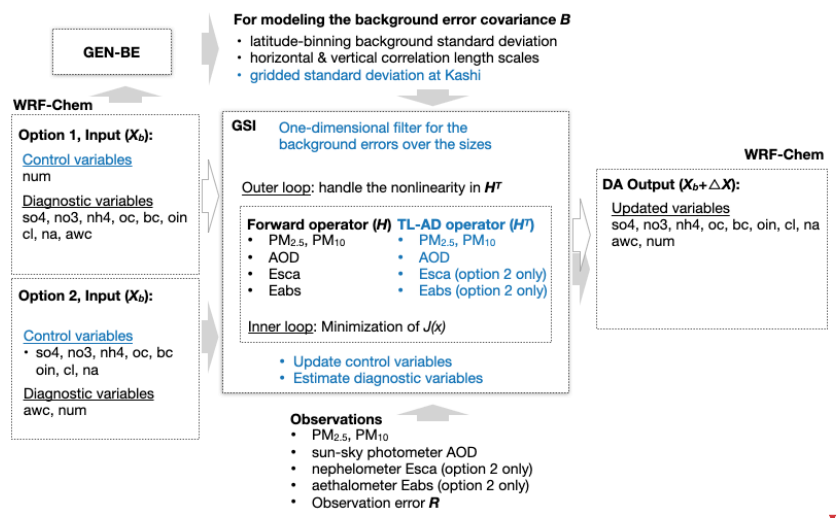
1695  
1696 [Toon, O. B., Pollack, J. B., and Khare, B. N.: The optical constants of several atmospheric](#)  
1697 [aerosol species: ammonium sulfate, aluminum oxide, and sodium chloride, \*J. Geophys. Res.\*,](#)  
1698 [81, 33, doi:10.1029/JC081i033p05733, 1976.](#)

1699  
1700 Wang, K.-Y., Lary, D. J., Shallcross D. E., Hall, S. M., and Pyle, J. A.: A review on the use of  
1701 the adjoint method in four-dimensional atmospheric-chemistry data assimilation, *Q. J. R.*  
1702 *Meteorol. Soc.*, 127, 2181-2204, doi:10.1002/qj.49712757616, 2001.

1703  
1704 [Wang, D., You, W., Zang, Z., Pan, X., He, H., and Liang, Y.: A three-dimensional variational](#)  
1705 [data assimilation system for a size-resolved aerosol model: Implementation and application](#)  
1706 [for particulate matter and gaseous pollutant forecasts across China, \*Sci. China-Earth Sci.\*, 63,](#)  
1707 [1366-1380, doi:10.1007/s11430-019-9601-4, 2020.](#)

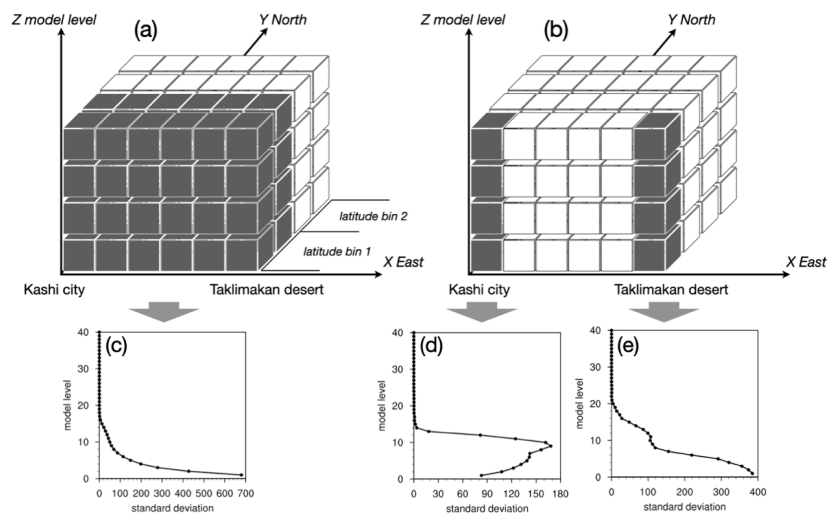
1708

1709 Wu, W.-S., Purser, r. J., and Parrish, D. F.: three-dimensional variational analysis with  
1710 spatially inhomogeneous covariances, *Mon. Weather Rev.*, 130, 12, 2905-2916,  
1711 doi: 10.1175/1520-0493(2002)130<2905:TDVAWS>2.0.CO;2, 2002.  
1712  
1713 Xia, X., Min, J., Shen, F., Wang, Y., and Yang, C.: Aerosol data assimilation using data from  
1714 Fengyun-3A and MODIS: application to a dust storm over East Asia in 2011, *Adv. Atmos.*  
1715 *Sci.*, 36, 1-14, doi:10.1007/s00376-018-8075-9, 2019a.  
1716  
1717 Xia, X., Min, J., Wang, Y., Shen, F., Yang, C., and Sun, Z.: Assimilating Himawari-8 AHI  
1718 aerosol observations with a rapid-update data assimilation system, *Atmos. Environ.*, 215,  
1719 116866, doi:10.1016/j.atmosenv.2019.116866, 2019b.  
1720  
1721 Zang, Z., Li, Z., Pan, X., Hao, Z., and You, W.: Aerosol data assimilation and forecasting  
1722 experiments using aircraft and surface observations during CalNex, *Tellus B.*, 68,1, 29812,  
1723 doi:10.3402/tellusb.v68.29812, 2016.  
1724  
1725 Zaveri, R. A., and Peters, L. K.: A new lumped structure photochemical mechanism for large-  
1726 scale applications, *J. Geophys. Res.*, 104, 30387-30415, doi:10.1029/1999JD900876, 1999.  
1727  
1728 Zaveri, R. A., Easter, R. C., Fast, J. D., Peters, L. K.: Model for simulating aerosol  
1729 interactions and chemistry (MOSAIC), *J. Geophys. Res.*, 113, D13204,  
1730 doi:10.1029/2007JD008782, 2008.  
1731  
1732 [Zhao, C., Liu, X., Leung, L. R., Johnson, B., McFarlane, S. A., Gustafson Jr., W. I., Fast, J.](#)  
1733 [D., and Easter, R.: The spatial distribution of mineral dust and its shortwave radiative forcing](#)  
1734 [over North Africa: modeling sensitivities to dust emissions and aerosol size treatments,](#)  
1735 [Atmos. Chem. Phys., 10, 8821-8838, doi:10.5194/acp-10-8821-2010, 2010.](#)  
1736  
1737 Zhao, J., Ma, X., Wu, S., and Sha, T.: Dust emission and transport in Northwest China: WRF-  
1738 Chem simulation and comparisons with multi-sensor observation, *Atmos. Res.*, 241, 104978,  
1739 doi:10.1016/j.atmosres.2020.104978, 2020.



1740  
1741  
1742  
1743  
1744  
1745  
1746  
1747  
1748  
1749  
1750

Figure 1. The workflow of aerosol DA in the revised GSI system for the sectional MOSAIC aerosols in WRF-Chem. The contents in blue are the portions we developed. The arrows in gray indicate the workflow of option 2 that we did in this study. Only option 2 can assimilate the aerosol scattering/absorption coefficients. Abbreviations: so4, sulfate; nh4, ammonium; oc, organic carbon; bc, black carbon; oin, other inorganic matter; awc, aerosol water content; num, aerosol number concentration; no3, nitrate; cl, chlorine; na, sodium; Esca, aerosol scattering coefficient; Eabs, aerosol absorption coefficient.

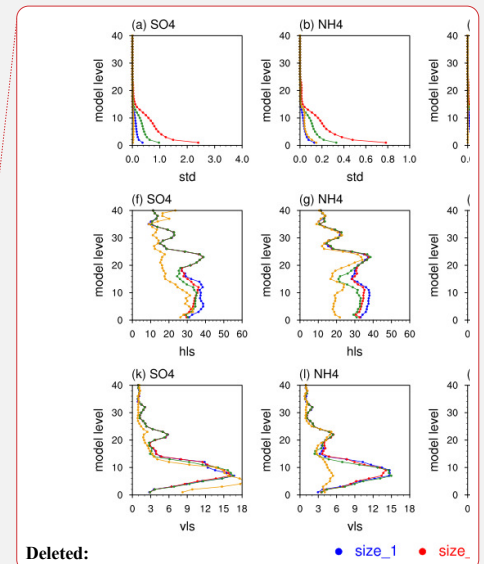
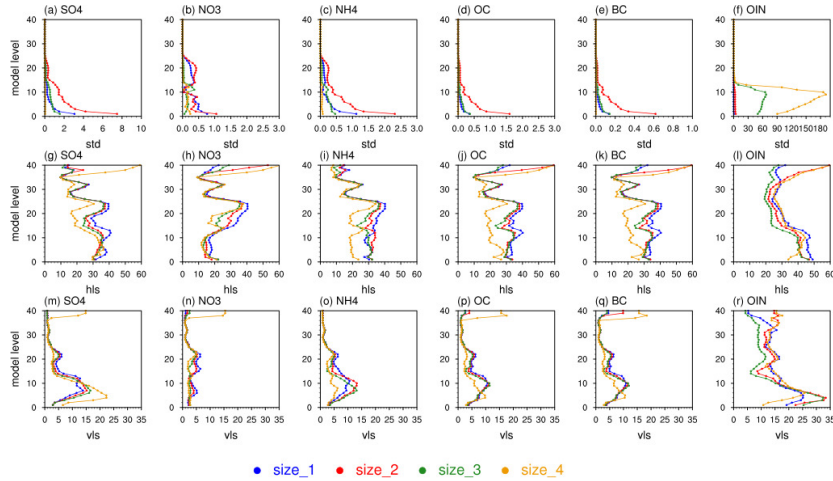


1752

1753

1754 Figure 2. Schematic diagram of the binning strategy for modeling background error  
 1755 covariance matrix on (a) the latitude binning data or (b) the gridded data; and the  
 1756 vertical profiles of standard deviations ( $\mu\text{g kg}^{-1}$ ) of the coarse OIN component  
 1757 concentration at 06:00UTC in April 2019 (c) on average over the latitude bins, (d) at  
 1758 Kashi city grid and (e) at the Taklimakan desert grid (i.e., 1.5 degrees east to the  
 1759 Kashi city).

1760



1761

1762

1763

1764

1765

1766

1767

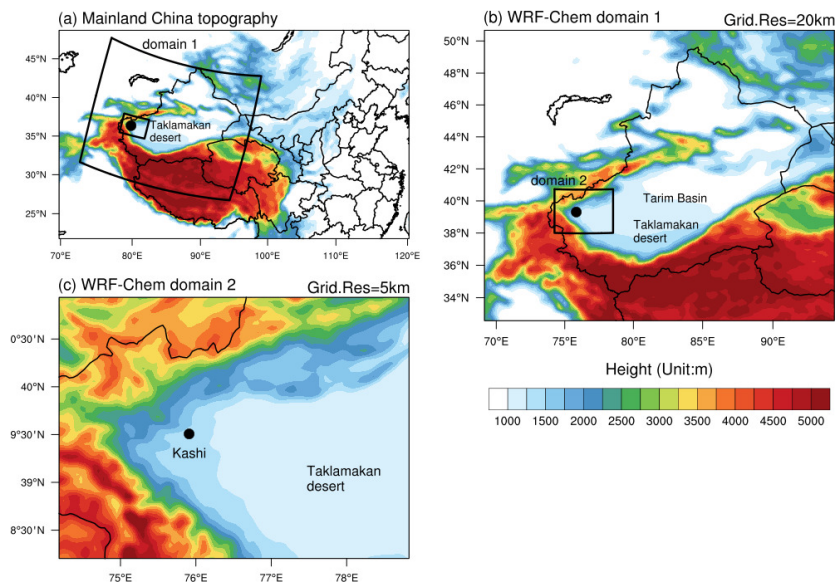
1768

1769

1770

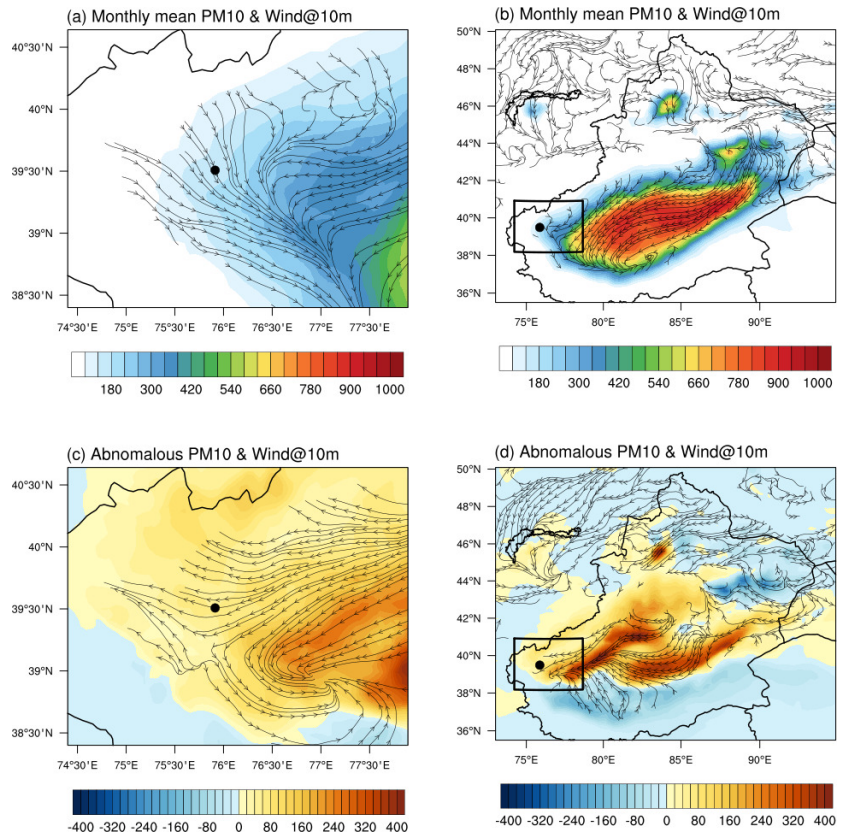
1771

Figure 3. Background error standard deviations at Kashi grid (std, a-f,  $\mu\text{g kg}^{-1}$ ), horizontal correlation length scales (hls, g-l, km), and vertical correlation length scales (vls, m-r, km) at 00:00 UTC in April 2019 for the sectional sulfate (SO4), nitrate (NO3), ammonium (NH4), organic aerosol (OC), black carbon (BC), and other inorganic aerosols (OIN, including dust) in the model domain 2. The horizontal and vertical correlation length were computed based on the latitude bins with a half degree width.



1773  
 1774  
 1775  
 1776  
 1777

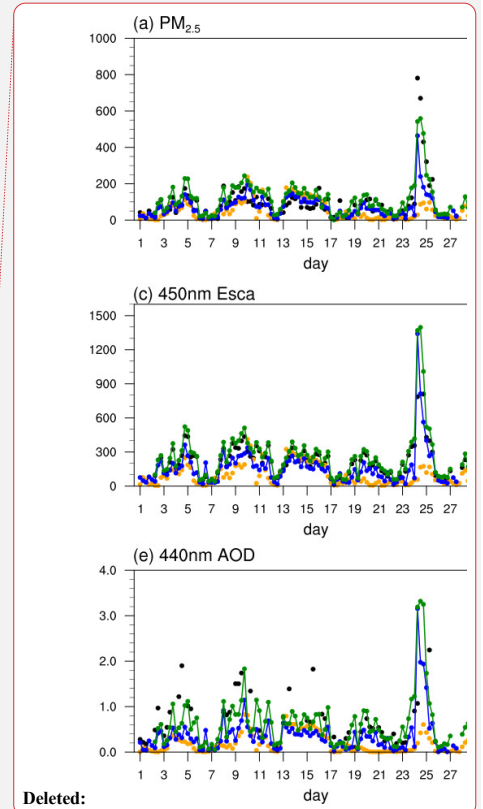
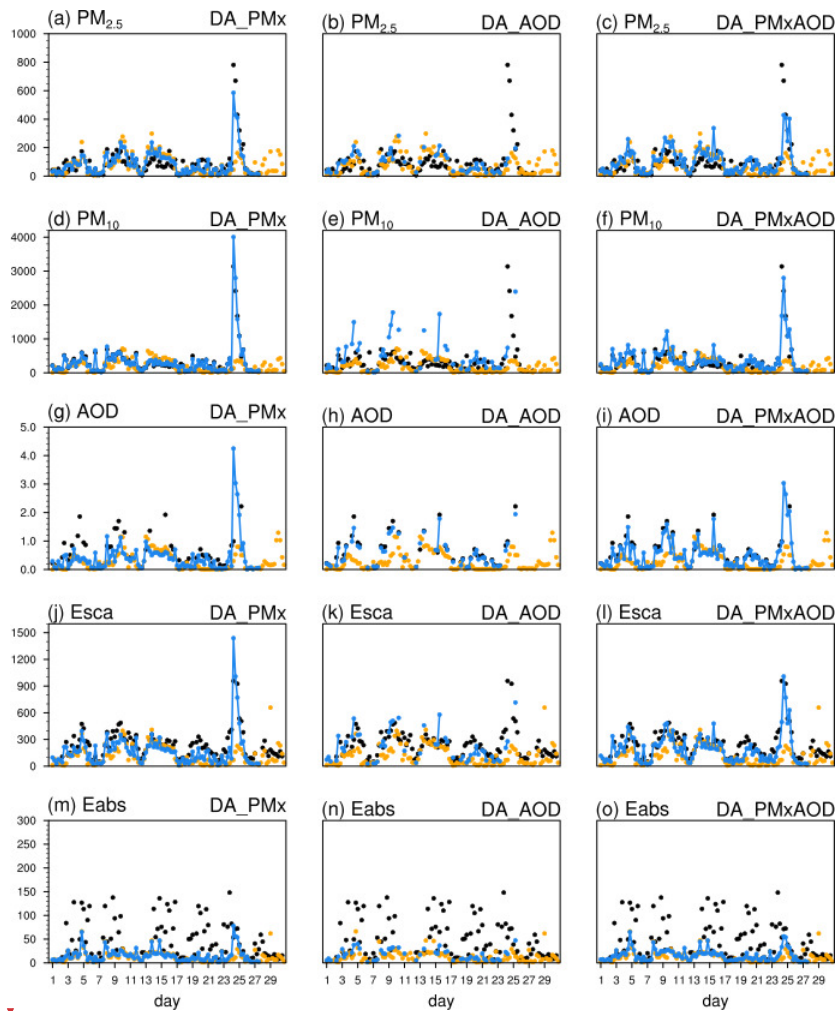
Figure 4. Topography in China (a) and the model domains with the grid resolution of 20 km (b) and 5 km (c) in WRF-Chem.



1778  
 1779  
 1780  
 1781  
 1782  
 1783  
 1784  
 1785  
 1786  
 1787  
 1788

Figure 5. Monthly mean  $PM_{10}$  concentration ( $\mu g m^{-3}$ ) and the streamlines of the 10-m wind ( $m s^{-1}$ ) in April (a, b) and their daily mean anomalies (c, d) during a dust storm on 24 April to the monthly mean values. Only the streamlines at the topographical height lower than 2500 meters are shown for clarity. The rectangles in figures (b) and (d) denote the fine model domain 2, which was the geographical range in the figures (a) and (c). The black points indicate the Kashi city.

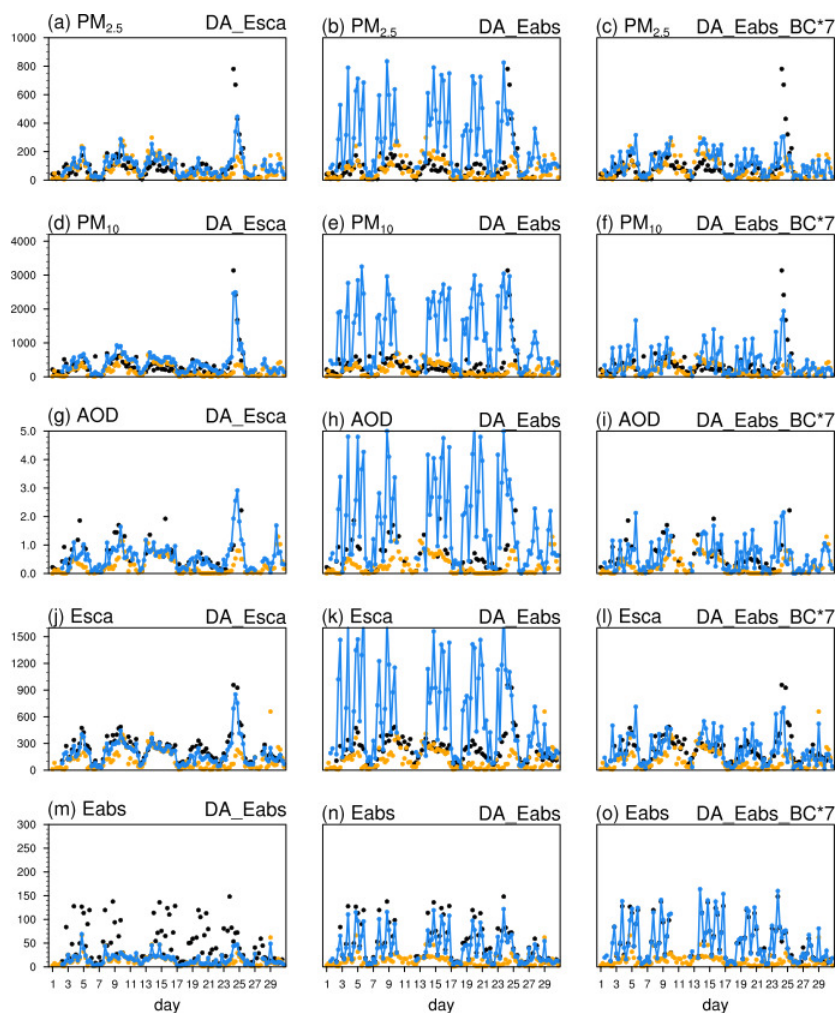
Deleted: (a)  
 Deleted: (b)



Deleted:

1791  
1792  
1793  
1794  
1795  
1796  
1797  
1798  
1799

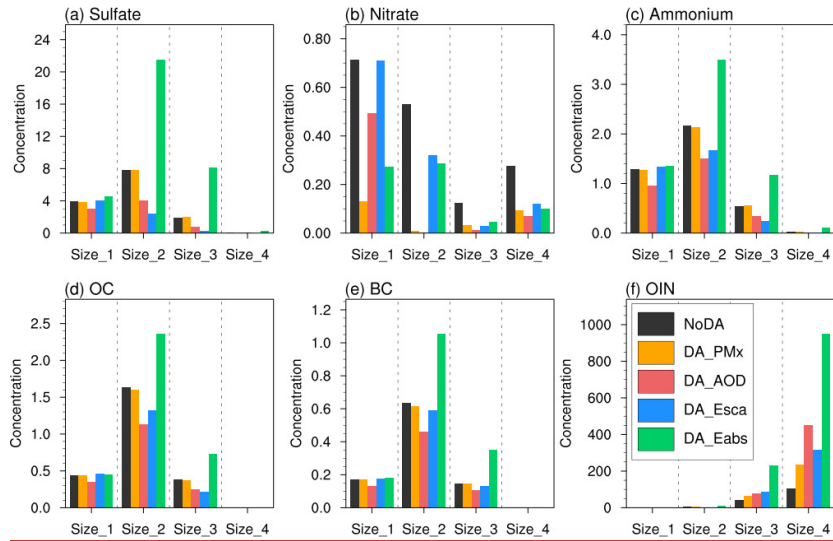
Figure 6. Comparison of PM<sub>2.5</sub> ( $\mu\text{g m}^{-3}$ ; a-c), PM<sub>10</sub> ( $\mu\text{g m}^{-3}$ ; d-f), 870 nm AOD (g-i), 635 nm aerosol scattering coefficient (Esca,  $\text{Mm}^{-1}$ ; j-l), and 660 nm aerosol absorption coefficient (Eabs,  $\text{Mm}^{-1}$ ; m-o) in the observation (black solid point), the background simulation (orange solid point), and the DA analyses (blue line) when assimilating the observed PM<sub>2.5</sub> and PM<sub>10</sub> (DA\_PMx), AOD (DA\_AOD), and simultaneously assimilating PMx and AOD (DA\_PMxAOD) at Kashi in April 2019.



1801  
 1802  
 1803  
 1804  
 1805  
 1806  
 1807  
 1808  
 1809  
 1810

Figure 7. Comparison of  $PM_{2.5}$  ( $\mu g m^{-3}$ ; a-c),  $PM_{10}$  ( $\mu g m^{-3}$ ; d-f), 870 nm AOD (g-i), 635 nm aerosol scattering coefficient (Esca,  $Mm^{-1}$ ; j-l), and 660 nm aerosol absorption coefficient (Eabs,  $Mm^{-1}$ ; m-o) in the observation (black solid point), the background simulation (orange solid point), and the DA analyses (blue line) when assimilating the aerosol scattering coefficient (DA\_Esca), aerosol absorption coefficient (DA\_Eabs), and absorption coefficient with the background error of BC enlarged by a factor of 7 (DA\_Eabs\_BC\*7) at Kashi in April 2019.

1811



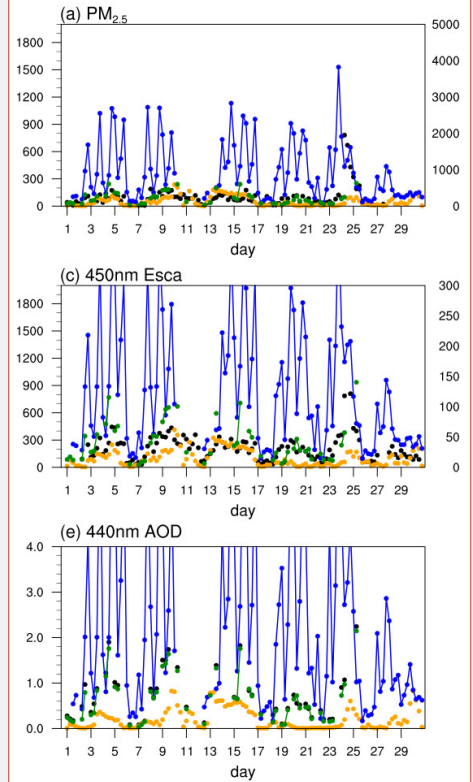
1812

1813

1814 Figure 8. Monthly mean aerosol concentrations ( $\mu\text{g m}^{-3}$ ) per size bin in the  
1815 background (NoDA) and the DA analyses when assimilating each individual  
1816 observation at Kashi in April 2019.

1817

Deleted: ¶

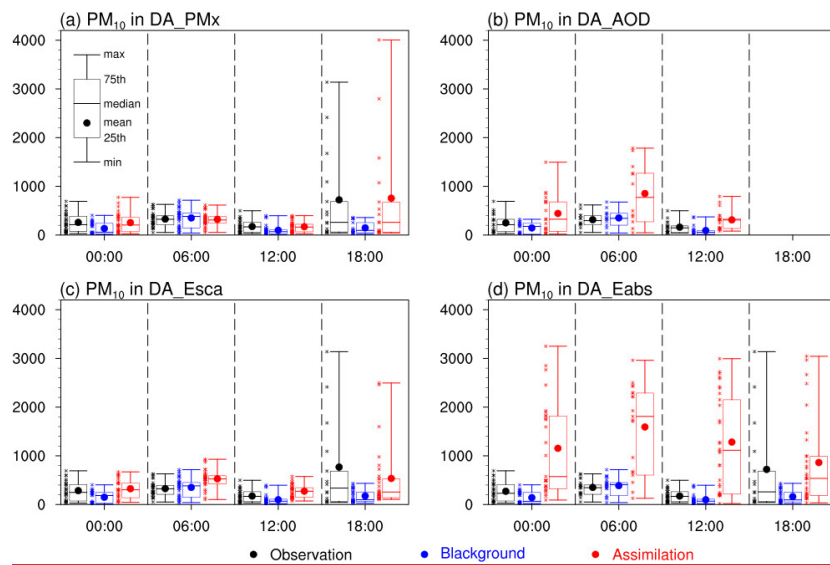


¶  
Figure 7. Comparison of (a)  $\text{PM}_{2.5}$  ( $\mu\text{g m}^{-3}$ ), (b)  $\text{PM}_{10}$  ( $\mu\text{g m}^{-3}$ ), (c) aerosol scattering coefficient (Esca,  $\text{Mm}^{-1}$ ), (d) aerosol absorption coefficient (Eabs,  $\text{Mm}^{-1}$ ) and (e) AOD in the observation (OBS), the background simulation (NoDA), and the DA analyses when assimilating the observed aerosol absorbing coefficients (DA\_Eabs) and AOD (DA\_AOD) at Kashi in April 2019. ¶

¶

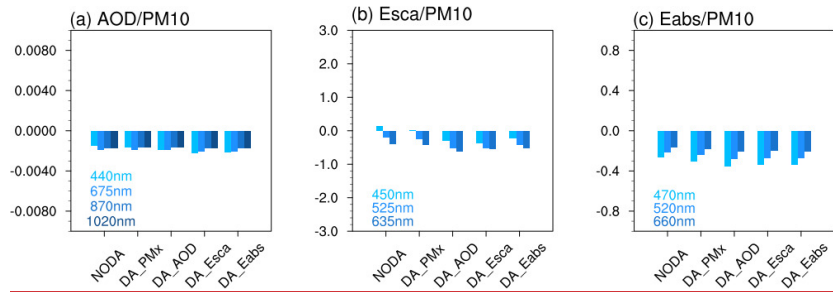
¶

Page Break



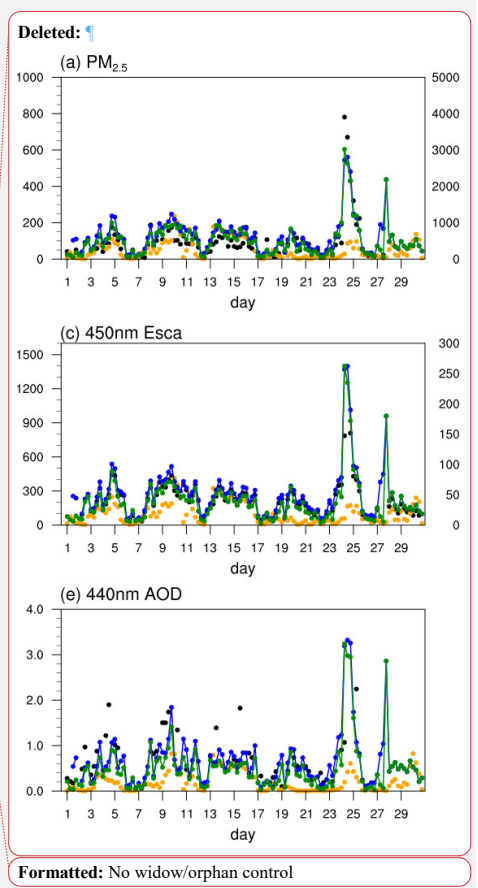
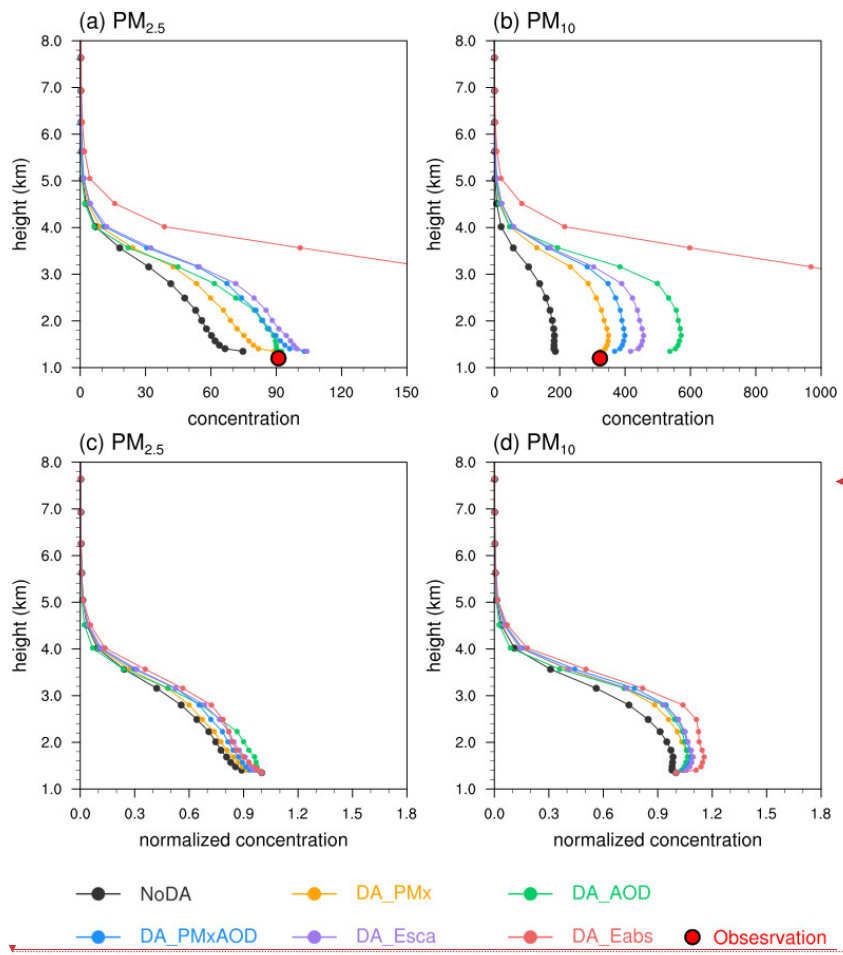
1831  
 1832  
 1833  
 1834  
 1835  
 1836  
 1837  
 1838  
 1839

Figure 9. Surface  $PM_{10}$  concentrations ( $\mu\text{g m}^{-3}$ ) in the observation (black), background simulation (blue) and the DA analyses (red) at 00:00, 06:00, 12:00, 18:00 UTC in April when assimilating the observations of (a)  $PM_x$ , (b) AOD, (c) aerosol scattering coefficients (Esca), and (d) aerosol absorption coefficient (Eabs) respectively. The DA\_AOD had no analysis at 18:00 UTC that was local midnight. Kashi is 6 hours ahead of UTC (UTC+6).



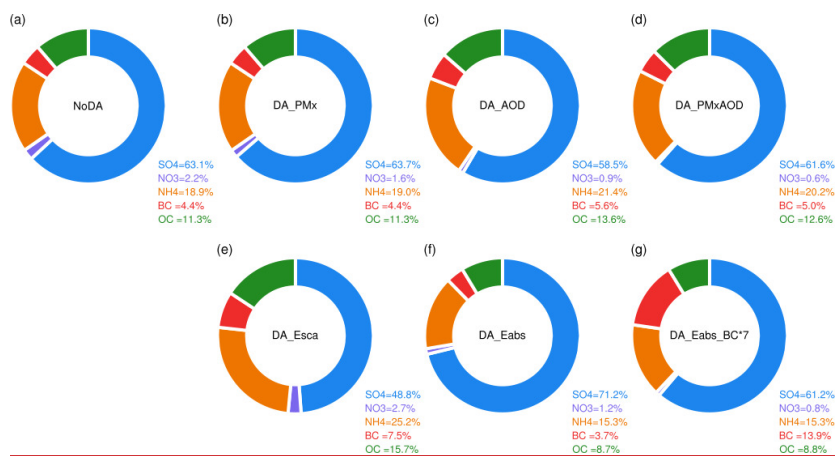
1840  
1841  
1842  
1843  
1844  
1845

Figure 10. Monthly mean biases in the ratios of AOD to PM<sub>10</sub>, aerosol scattering coefficient (Esca, Mm<sup>-1</sup>), and aerosol absorbing coefficient (Eabs, Mm<sup>-1</sup>) at Kashi in April 2019.



1846  
 1847  
 1848  
 1849  
 1850  
 1851  
 1852

Figure 11. Monthly mean vertical concentration profiles of (a)  $PM_{2.5}$  ( $\mu g m^{-3}$ ), (b)  $PM_{10}$  ( $\mu g m^{-3}$ ) and their normalized concentration respect to the surface concentration (c, d) at Kashi in April 2019.



1855

1856

1857

1858 Figure 12. Monthly mean chemical composition in percent (%) in the simulated PM<sub>10</sub>,

1859 excluding the OIN component at Kashi in April 2019.

1860

1861

1862 Table 1. The observed surface particle concentration, aerosol scattering coefficient  
 1863 (Esca), aerosol absorption coefficient (Eabs), and AOD used for the DA analysis and  
 1864 their observational errors.  
 1865

	Data time range	Wavelength (nm)	Observation error ( $e$ )
PM <sub>2.5</sub> & PM <sub>10</sub> ( $\mu\text{g m}^{-3}$ )	Apr 1 – Apr 30		$e = \sqrt{e_1^2 + e_2^2}$ $e_1 = 1.5 + 0.0075 \cdot PM_x$ $e_2 = 0.5 \cdot e_1 \cdot \sqrt{\frac{d}{3000}}$ <p><math>d</math>: grid spacing in meter</p>
AOD	Mar 29 – Apr 25	440, 675, 870, 1020	$e = 0.01/\text{height} \times 10^8$
Esca (Mm <sup>-1</sup> )	Apr 2 – Apr 30	450, 525, 635	$e = 10$
Eabs (Mm <sup>-1</sup> )	Apr 2 – Apr 30	470, 520, 660	$e = 10$

1866  
 1867

1868 Table 2. The monthly mean values of the PM<sub>2.5</sub> and PM<sub>10</sub> concentrations ( $\mu\text{g m}^{-3}$ ),  
 1869 635 nm aerosol scattering coefficient (Esca,  $\text{Mm}^{-1}$ ), 660 nm aerosol absorption  
 1870 coefficient (Eabs,  $\text{Mm}^{-1}$ ) and 870 nm AOD in the background and analysis data and  
 1871 their correlation values (in brackets) with the observations at 00:00, 06:00, 12:00,  
 1872 18:00 UTC at Kashi in April 2019. The underlined number in bold denotes the  
 1873 monthly mean value that is not significantly different from the observation, and the  
 1874 dashed line denotes an insignificant correlation. Both the statistical tests of the mean  
 1875 difference and correlation are conducted at the significance level of 0.05.

DA experiment	PM <sub>2.5</sub> ( $\mu\text{g m}^{-3}$ )	PM <sub>10</sub> ( $\mu\text{g m}^{-3}$ )	<u>870 nm</u> AOD	<u>635nm</u> Esca ( $\text{Mm}^{-1}$ )	<u>660nm</u> Eabs ( $\text{Mm}^{-1}$ )
Observation	91.0	323.2	<u>0.66</u>	<u>231.5</u>	<u>47.4</u>
Background	<u>75.3</u> (0.28)	<u>190.7</u> (0.24)	<u>0.24</u> (0.60)	<u>123.3</u> (0.36)	<u>12.9</u> (0.34)
DA_PMx	<u>89.3</u> (0.89)	<u>329.3</u> (0.99)	<u>0.38</u> (0.35)	<u>170.4</u> (0.89)	<u>15.8</u> (0.42)
DA_AOD	<u>92.6</u> (0.35)	<u>541.7</u> (0.31)	<u>0.59</u> (0.98)	<u>222.6</u> (0.61)	<u>17.0</u> (0.26)
<u>DA_PMx_AOD</u>	<u>103.6</u> (0.61)	<u>372.7</u> (0.86)	<u>0.59</u> (0.98)	<u>192.2</u> (0.86)	<u>16.7</u> (0.45)
<u>DA_Esca</u>	<u>103.6</u> (0.67)	<u>442.1</u> (0.93)	<u>0.53</u> (0.62)	<u>192.1</u> (0.97)	<u>16.5</u> (0.47)
DA_Eabs	<u>298.8</u> (0.36)	<u>1281.2</u> (0.34)	<u>1.73</u> (----)	<u>612.2</u> (0.54)	<u>40.0</u> (0.98)
<u>DA_Eabs BC*7</u>	<u>106.7</u> (0.48)	<u>463.7</u> (0.45)	<u>0.75</u> (0.50)	<u>226.2</u> (0.52)	<u>51.9</u> (0.90)

1877  
1878

1879 Table 3. The Ångström exponent based on the AOD at 440 nm and 1020 nm and the  
 1880 surface single scattering albedo (SSAsrf=Esca525/(Esca525+Eabs520)) at Kashi in  
 1881 April 2019

	<u>440-1020 nm Ångström</u> <u>exponent</u>	<u>SSAsrf</u>
<u>Observation</u>	<u>0.18</u>	<u>0.78</u>
<u>Background</u>	<u>0.54</u>	<u>0.86</u>
<u>DA_PMx</u>	<u>0.30</u>	<u>0.88</u>
<u>DA_AOD</u>	<u>-0.01</u>	<u>0.88</u>
<u>DA_PMx_AOD</u>	<u>0.17</u>	<u>0.89</u>
<u>DA_Esca</u>	<u>-0.15</u>	<u>0.88</u>
<u>DA_Eabs</u>	<u>-0.01</u>	<u>0.90</u>
<u>DA_Eabs_BC*7</u>	<u>0.33</u>	<u>0.82</u>

1883  
 1884

1885 Table 4. The ratios of AOD, aerosol scattering/absorption coefficient to PM<sub>10</sub>  
 1886 concentration (mean ± standard deviation) in the observations, the model background  
 1887 data, and the DA [analyses](#).  
 1888

	Ratios of <u>870 nm</u> AOD to PM <sub>10</sub> ( $\mu\text{g}^{-1} \text{m}^3$ )	Ratios of <u>635 nm</u> aerosol scattering coefficient ( <u>E<sub>sca</sub></u> ) to PM <sub>10</sub> ( $\text{Mm}^{-1} \mu\text{g}^{-1}$ $\text{m}^3$ )	Ratios of <u>660 nm</u> aerosol absorption coefficient ( <u>E<sub>abs</sub></u> ) to PM <sub>10</sub> ( $\text{Mm}^{-1} \mu\text{g}^{-1}$ $\text{m}^3$ )
Observation	<u>0.0030±0.0020</u>	<u>1.05±0.57</u>	<u>0.25±0.22</u>
Background	<u>0.0013±0.0009</u>	<u>0.65±0.18</u>	<u>0.09±0.05</u>
DA_PMx	<u>0.0013±0.0008</u>	<u>0.61±0.22</u>	<u>0.07±0.05</u>
<u>DA_AOD</u>	<u>0.0013±0.0011</u>	<u>0.51±0.24</u>	<u>0.05±0.04</u>
<u>DA_PMx_AOD</u>	<u>0.0015±0.0010</u>	<u>0.61±0.24</u>	<u>0.06±0.05</u>
<u>DA_Esca</u>	<u>0.0015±0.0010</u>	<u>0.52±0.21</u>	<u>0.05±0.05</u>
<u>DA_Eabs</u>	<u>0.0015±0.0010</u>	<u>0.58±0.37</u>	<u>0.05±0.06</u>
<u>DA_Eabs_BC*7</u>	<u>0.0023±0.0085</u>	<u>0.74±0.51</u>	<u>0.30±0.48</u>

1889  
 1890

1891 Table 5. The mean instantaneous clear-sky shortwave (SW), longwave (LW) and the  
 1892 net (SW+LW) direct radiative forcing ( $\text{Wm}^{-2}$ ) at the top of atmosphere (TOA), in the  
 1893 atmosphere (ATM) and at the surface (SRF) in the background and the simulations  
 1894 restarted from the analyses of DA\_PMx and DA\_PMx\_AOD at one hour after the  
 1895 analysis times of AOD DA at Kashi in April 2019.  
 1896

	SW ( $\text{Wm}^{-2}$ )			LW ( $\text{Wm}^{-2}$ )			SW+LW ( $\text{Wm}^{-2}$ )		
	TOA	ATM	SRF	TOA	ATM	SRF	TOA	ATM	SRF
Background	<u>-7.0</u>	<u>+17.0</u>	<u>-24.0</u>	<u>+0.3</u>	<u>-2.9</u>	<u>+3.2</u>	<u>-6.7</u>	<u>+14.1</u>	<u>-20.8</u>
DA_PMx	<u>-8.5</u>	<u>+22.7</u>	<u>-31.2</u>	<u>+0.6</u>	<u>-6.3</u>	<u>+6.9</u>	<u>-7.9</u>	<u>+16.4</u>	<u>-24.3</u>
DA_PMx_A OD	<u>-11.4</u>	<u>+28.6</u>	<u>-40.0</u>	<u>+1.0</u>	<u>-7.8</u>	<u>+8.8</u>	<u>-10.4</u>	<u>+20.8</u>	<u>-31.2</u>

1897  
 1898